Electronic Supplementary Material (ESI) for Organic Chemistry Frontiers.

Supporting Information

NBN/BNB-Doped phenalenyl homo- and heterodyads: structural uniformity but optoelectronic diversity

Alexander S. Scholz,[a] Thomas Froitzheim,[b]* Michael Bolte,[a] Hans-Wolfram Lerner,[a] Jan-M. Mewes,[b] Matthias Wagner[a]*

[a]*Institut für Anorganische und Analytische Chemie*
Goethe-Universität Frankfurt am Main
Max-von-Laue-Straße 7, 60438 Frankfurt (Main), Germany.
E-mail: matthias.wagner@chemie.uni-frankfurt.de

[b]*Mulliken Center for Theoretical Chemistry, Institut für Physikalische und Theoretische Chemie*
Rheinische Friedrich Wilhelms-Universität Bonn
Beringstr. 4, 53115 Bonn, Germany.
E-mail: th.froitzheim@thch.uni-bonn.de

Table of contents

1. General experimental procedures

If not stated otherwise, all reactions and manipulations were carried out under an atmosphere of dry nitrogen using Schlenk techniques or in an inert-atmosphere glovebox. *n*-Hexane and *n*-pentane were distilled from Na metal. C_6H_6, toluene, Et_2O, and THF were distilled from Na/benzophenone. CH_2Cl_2 and $CHCl_3$ were distilled from CaH_2. $CDCl_3$ and 1,4-dioxane were stored over 3 Å molecular sieves.

The starting materials 1,8-naphthalenediyl-bridged diborane(6) **C**,[S1] compound **E**,[S2] mesitylmagnesium bromide (MesMgBr; Mes = mesityl),[S3] 2,6-Me_2-4-$(Me_3Si)_2N$-C_6H_2-Br,[S4] 4-$(Me_3Si)_2N$-C_6H_4-Br,[S4] and *N*,*N*'-dimethylnaphthalene-1,8-diamine **A**[S5] were prepared according to literature procedures. The following chemicals were purchased from commercial suppliers and used as received: 3 Å molecular sieves (*Roth*), *p*-phenylenediamine **D** (*Fluorochem*), 4-bromoaniline (*Abcr*), *N*,*N*-di-*iso*-propylethylamine (*i*-Pr_2NEt; *Abcr*), *p*-phenylenediboronic acid (*Sigma-Aldrich*), boron trichloride in CH_2Cl_2 (1 M, *Sigma-Aldrich*), and methylmagnesium bromide in Et_2O (3 M, *Sigma-Aldrich*).

NMR spectra were recorded at 298 K using a *Bruker* Avance-500 spectrometer. Chemical shift values are referenced to (residual) solvent signals ($^1H/^{13}C\{^1H\}$; $CDCl_3$: δ = 7.26/77.16) or external $BF_3{\cdot}Et_2O$ (^{11}B; δ = 0.00).[S6] Abbreviations: s = singlet, d = doublet, dd = doublet of doublets, vt = virtual triplet, br. = broad, n.o. = not observed. Resonances of carbon atoms attached to boron atoms were typically broadened and sometimes not observed due to the quadrupolar relaxation of boron. Resonance assignments were aided by ^{H,H}COSY, ^{H,C}HSQC, and ^{H,C}HMBC spectra.

UV/vis absorption spectra were recorded at room temperature using a *Varian* Cary 60 Scan UV/vis spectrophotometer. Photoluminescence (PL) spectra were recorded at room temperature using a *Jasco* FP-8300 spectrofluorometer equipped with a calibrated *Jasco* ILF-835 100 mm diameter integrating sphere and analyzed using the *Jasco* FWQE-880 software. For PL quantum yield (Φ_{PL}) measurements, each sample was carefully degassed with argon using an injection needle and a septum-capped cuvette. Under these conditions, the Φ_{PL} of the fluorescence standard 9,10-diphenylanthracene was determined as 97% (lit.: 97%).[S7,S8] For all Φ_{PL} measurements, at least three samples of different concentrations were used (range between 10^{-5} and 10^{-7} mol L^{-1}). Due to self-absorption, slightly lower Φ_{PL} values were observed at higher concentrations. Aggregation-induced emission (enhancement) measurements were performed in THF with water fractions between 0% and 99% H_2O at a concentration of 1.5×10^{-4} mol L^{-1}. The samples were homogenized in an ultrasonic bath for two minutes and used without further dilution. Solid-state fluorescence was measured in quartz-glass tubes in a similar manner as the measurements in solution.

Cyclic voltammetry (CV) measurements were performed in an inert-atmosphere glovebox at room temperature in a one-chamber, three-electrode cell using an *EG&G* Princeton Applied Research 263A potentiostat. A platinum-disk electrode (2.00 mm diameter) was used as the working electrode with a platinum wire counter electrode and a silver wire reference electrode, which was coated with AgCl by immersion into HCl/HNO_3 (3:1). Prior to measurements, THF was dried over Na and degassed by three freeze-pump-thaw cycles. [*n*-Bu_4N][PF_6] (*Sigma-Aldrich*; used as received) was employed as the supporting electrolyte (0.1 M). All potential values were referenced against the FcH/FcH^+ redox couple (FcH = ferrocene; $E_{1/2}$ = 0 V). Measurements employing the FcH^*/FcH^{*+} redox couple were referenced against the FcH/FcH^+ redox couple with a conversion factor of 0.446 V (FcH* = decamethylferrocene).[S9] Scan rates were varied between 100 and 400 mV s^{-1}.

High-resolution mass spectra were measured in positive mode using a *Thermo Fisher Scientific* MALDI LTQ Orbitrap XL spectrometer and α-cyano-4-hydroxycinnamic acid as the matrix.

2. Syntheses, purification methods, and analytical data

2.1. Synthesis of compound B

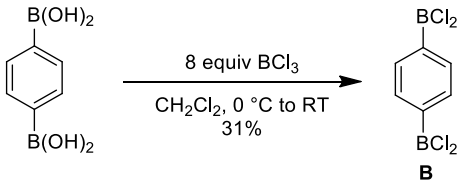

B

This compound is known, albeit with a different synthesis.[S10] BCl_3 (1 M in CH_2Cl_2, 39 mL, 39 mmol, 8 equiv) was added dropwise with stirring to solid *p*-phenylenediboronic acid (810 mg, 4.89 mmol, 1 equiv) at 0 °C within 20 min. The yellow reaction mixture was slowly warmed to room temperature over the course of 12 h. All volatiles were removed under reduced pressure to yield an off-white solid, which was sublimed (80 °C, ca. 10^{-3} Torr) to give colorless crystals of **B** suitable for X-ray analysis. Yield: 360 mg (1.50 mmol, 31%).

^{1}H NMR ($CDCl_3$, 500.2 MHz): δ = 8.22 (s, C_6H_4)

^{13}C{^{1}H} NMR ($CDCl_3$, 125.8 MHz): δ = 139.5* (br., B*C*), 136.0 (C_6H_4). *) This signal was further confirmed through a ^{H,C}HMBC NMR experiment.

^{11}B NMR ($CDCl_3$, 160.5 MHz): δ = 56.0 (s).

2.2. Synthesis of compound 1^{Me}

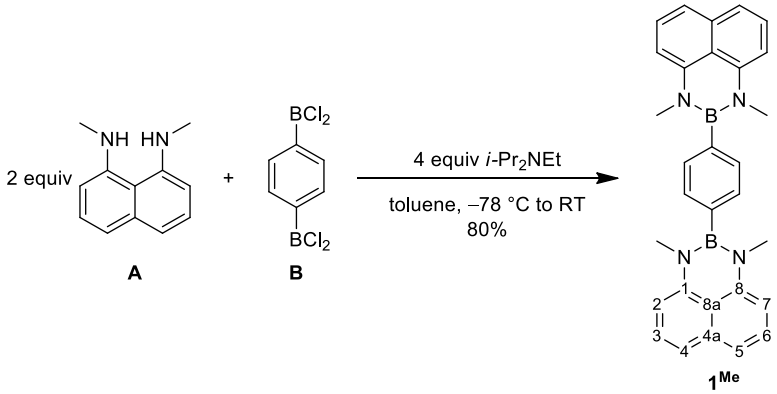

N,*N*'-dimethylnaphthalene-1,8-diamine **A** (155 mg, 0.832 mmol, 2 equiv) and *i*-Pr_2NEt (0.30 mL, 1.7 mmol, 4 equiv) were dissolved in toluene (6 mL); the mixture was cooled to –78 °C. Compound **B** (100 mg, 0.417 mmol, 1 equiv) in toluene (3 mL) was added dropwise with stirring at –78 °C. The dropping funnel was rinsed with toluene (2 × 1 mL) after the complete addition. The cooling bath was removed after 30 min at –78 °C and stirring was continued for another 12 h at room temperature. H_2O (10 mL) and CH_2Cl_2 (20 mL) were added to the brown solution. The phases were separated and the aqueous phase was extracted with CH_2Cl_2 (6 × 10 mL). The combined organic phases were dried over $MgSO_4$ and filtered through a plug of neutral Al_2O_3. The plug was flushed with CH_2Cl_2 (2 × 10 mL) and the filtrate was evaporated to dryness under reduced pressure to yield $\mathbf{1^{Me}}$ as a colorless solid. Yield: 155 mg (0.332 mmol, 80%). Single crystals of $\mathbf{1^{Me}}\cdot CH_2Cl_2$ suitable for X-ray analysis were obtained by recrystallization from CH_2Cl_2.

^{1}H NMR ($CDCl_3$, 500.2 MHz): δ = 7.53 (s, 4H; C_6H_4), 7.34 (vt, 4H; H3,6), 7.23 (dd, ^3J(H,H) = 8.3 Hz, ^4J(H,H) = 0.9 Hz, 4H; H4,5), 6.56 (d, ^3J(H,H) = 7.8 Hz, 4H; H2,7), 2.97 (s, 12H; Me).

^{13}C{^{1}H} NMR ($CDCl_3$, 125.8 MHz): δ = 143.2 (C1,8), 138.0* (B*C*), 136.0 (C4a), 131.7 (C_6H_4), 127.4 (C3,6), 120.7 (C8a), 118.4 (C4,5), 103.8 (C2,7), 35.9 (Me). *) This signal was detected through a ^{H,C}HMBC NMR experiment.

^{11}B NMR ($CDCl_3$, 160.5 MHz): δ = 32.7 (s).

HRMS: Calculated *m/z* for $[C_{30}H_{28}B_2N_4]^{\bullet+}$: 466.24946, found: 466.24915.

2.3. Synthesis of compound 2^H

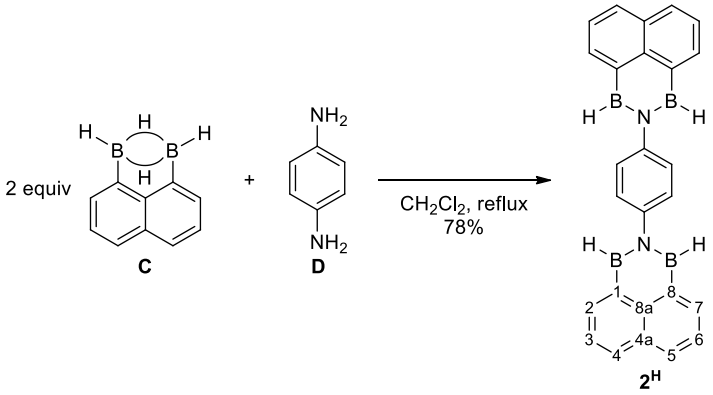

Borane **C** (256 mg, 1.69 mmol, 2 equiv) and *p*-phenylenediamine **D** (91 mg, 0.84 mmol, 1 equiv) were suspended in CH_2Cl_2 (2.6 mL) and heated under reflux with stirring for 4 h. After cooling to room temperature, C_6H_6 (1.3 mL) was added to the colorless suspension. The solid was then collected on a Schlenk frit. The filter cake was washed with C_6H_6 (3 × 1 mL) and afterwards dried under reduced pressure to furnish $\mathbf{2^H}$ as a colorless solid. Yield: 265.5 mg (0.657 mmol, 78%). Single crystals of $\mathbf{2^H}$ suitable for X-ray analysis were obtained by recrystallization of the product from THF.

^{1}H NMR ($CDCl_3$, 500.2 MHz): δ = 8.40 (dd, ^3J(H,H) = 6.7 Hz, ^4J(H,H) = 1.3 Hz, 4H; H2,7), 8.21 (dd, ^3J(H,H) = 8.2 Hz, ^4J(H,H) = 1.3 Hz, 4H; H4,5), 7.76 (dd, ^3J(H,H) = 8.2 Hz, ^3J(H,H) = 6.7 Hz, 4H; H3,6), 7.48 (s, 4H; C_6H_4), 6.08 (br., 4H; BH).

^{13}C{^{1}H} NMR ($CDCl_3$, 125.8 MHz): δ = 148.4 (NC), 142.9 (C2,7), 136.5 (C8a), 135.3 (br., C1,8), 134.1 (C4,5), 131.0 (C4a), 126.4 (C3,6), 125.1 (C_6H_4).

^{11}B NMR ($CDCl_3$, 160.5 MHz): δ = 48.4 (br.).

HRMS: Calculated *m/z* for $[C_{26}H_{20}B_4N_2]^{\bullet+}$: 404.19932, found: 404.19934.

2.4. Synthesis of compound 2^{Me}

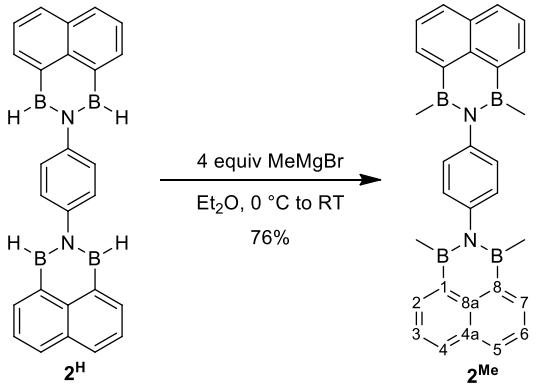

$\mathbf{2^H}$ (150.1 mg, 0.371 mmol, 1 equiv) was suspended in Et_2O (3 mL). MeMgBr (3.16 M in Et_2O, 0.48 mL, 1.5 mmol, 4 equiv) was added dropwise with stirring at 0 °C. After 1 h, the cooling bath was removed and stirring continued for 12 h at room temperature. C_6H_6 (3 mL) was added and the suspension placed in an ultrasonic bath until the solid was homogeneously suspended and no solid remained stuck to the flask. The solid was then collected on a Schlenk frit and washed with Et_2O (5 × 2 mL). The solid was first dried under reduced pressure at room temperature and then at 60 °C for 2 h to furnish the product as a colorless powder. Yield: 129.9 mg (0.282 mmol, 76%). Single crystals of $\mathbf{2^{Me}}\cdot CH_2Cl_2$ were grown by gas-phase diffusion of *n*-hexane into a CH_2Cl_2 solution of $\mathbf{2^{Me}}$.

^{1}H NMR ($CDCl_3$, 500.2 MHz): δ = 8.43 (dd, ^3J(H,H) = 6.9 Hz, ^4J(H,H) = 1.3 Hz, 4H; H2,7), 8.12 (dd, ^3J(H,H) = 8.1 Hz, ^4J(H,H) = 1.3 Hz, 4H; H4,5), 7.68 (dd, ^3J(H,H) = 8.1 Hz, ^3J(H,H) = 6.9 Hz, 4H; H3,6), 7.08 (s, 4H; C_6H_4), 0.88 (s, 12H; Me).

^{13}C{^{1}H} NMR ($CDCl_3$, 125.8 MHz): δ = 146.3 (NC), 138.2 (C2,7), 136.9 (C8a), 134.5 (br., C1,8), 133.0 (C4,5), 131.6 (C4a), 127.8 (C_6H_4), 125.9 (C3,6), 3.3 (Me).

^{11}B NMR ($CDCl_3$, 160.5 MHz): δ = 51.2 (s).

HRMS: Calculated *m/z* for $[C_{30}H_{28}B_4N_2]^{\bullet+}$: 460.26192, found: 460.26109.

2.5. Synthesis of compound 2^{Mes}

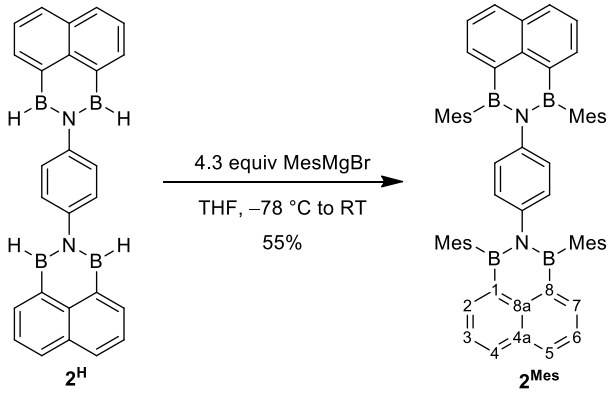

$\mathbf{2^H}$ (205.4 mg, 0.508 mmol, 1 equiv) was suspended in THF (5 mL). MesMgBr (1.49 M in THF, 1.5 mL, 2.2 mmol, 4.3 equiv) was added dropwise with stirring at −78 °C. After 1 h, the cooling bath was removed and stirring continued for 12 h at room temperature. All volatiles were removed under reduced pressure and the resulting orange solid was purified by column chromatography (SiO_2, 20:1 C_6H_{12}:ethyl acetate + 1% triethylamine). After removal of all volatiles from the eluate under reduced pressure, a colorless solid was obtained. Yield: 247 mg (0.282 mmol, 55%). Single crystals of $\mathbf{2^{Mes}}\cdot C_6H_{12}$ were obtained by slow evaporation of a solution of $\mathbf{2^{Mes}}$ in *c*-hexane.

^{1}H NMR ($CDCl_3$, 500.2 MHz): δ = 8.10 (dd, ^3J(H,H) = 8.2 Hz, ^4J(H,H) = 1.3 Hz, 4H; H4,5), 7.78 (dd, ^3J(H,H) = 6.9 Hz, ^4J(H,H) = 1.3 Hz, 4H; H2,7), 7.53 (dd, ^3J(H,H) = 8.2 Hz, ^3J(H,H) = 6.9 Hz, 4H; H3,6), 6.72 (s, 8H; MesCH), 6.35 (s, 4H; C_6H_4), 2.37 (s, 12H; $MesCH_3$-*p*), 1.84 (s, 24H; $MesCH_3$-*o*).

^{13}C{^{1}H} NMR ($CDCl_3$, 125.8 MHz): δ = 144.0 (NC), 141.0 (C2,7), 138.5 (MesC-*o*), 138.2 (br., MesC-*i*), 137.0 (C8a), 136.2 (MesC-*p*), 134.2 (br., C1,8), 133.3 (C4,5), 131.4 (C4a), 126.9 (MesCH), 126.2 (C3,6), 125.0 (C_6H_4), 22.8 ($MesCH_3$-*o*), 21.5 ($MesCH_3$-*p*).

^{11}B NMR ($CDCl_3$, 160.5 MHz): δ = n.o.

HRMS: Calculated *m/z* for $[C_{30}H_{28}B_4N_2]^{\bullet+}$: 876.51232, found: 876.51256.

2.6. Synthesis of compound 5

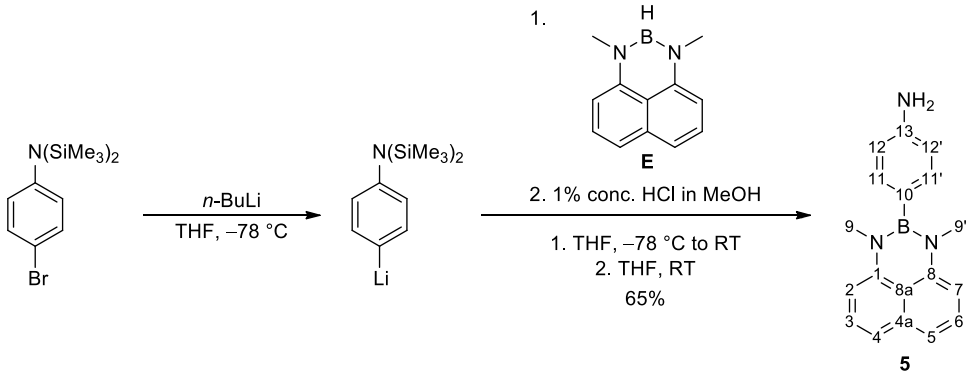

n-BuLi (2.42 M in *n*-hexane, 2.3 mL, 5.6 mmol, 1 equiv) was added dropwise with stirring at −78 °C to a solution of 4-$(Me_3Si)_2N$-C_6H_4-Br (1.790 g, 5.658 mmol, 1 equiv) in THF (8 mL).[S4] After rinsing the dropping funnel with *n*-hexane (2 mL), a suspension of **E** (1.110 g, 5.662 mmol, 1 equiv) in THF (10 mL) was added dropwise at −78 °C. The solid remaining in the dropping funnel was rinsed into the reaction mixture with THF (2 × 5 mL). The reaction mixture was slowly warmed to room temperature over the course of 12 h, which led to a color change from brown to beige. A solution of HCl in MeOH (5 mL, 1 vol% conc. HCl) was added to the reaction mixture at room temperature, whereupon the color changed from beige to green. After 15 min of stirring at room temperature, all volatiles were removed under reduced pressure. The green solid was dissolved in Et_2O (40 mL) and a saturated aqueous solution of $NaHCO_3$ (40 mL) was added. The phases were separated and the aqueous phase was extracted with Et_2O (4 × 40 mL). The combined organic phases were dried over $MgSO_4$ and filtered. All volatiles were removed from the filtrate under reduced pressure. The crude product was dissolved in ethyl acetate (20 mL) and filtered through a plug of neutral Al_2O_3. All volatiles were removed from the yellow filtrate to yield an orange solid, which was recrystallized from *n*-hexane:ethyl acetate (20:1, ca. 165 mL). After cooling to room temperature, the flask was placed in a freezer (−30 °C). Brownish single crystals suitable for X-ray analysis grew overnight. The mother liquor was separated from the crystals, which were then washed with *n*-hexane:ethyl acetate (20:1, 3 × 5 mL) and dried under reduced pressure to yield 962 mg of **5**. All volatiles were removed from the mother liquor and the recrystallization was repeated to yield another 100 mg of product. Combined yield: 1062 mg (3.698 mmol, 65%).

^{1}H NMR ($CDCl_3$, 500.2 MHz): δ = 7.35 (vt, 2H; H3,6), 7.27 (d, ^3J(H,H) = 7.9 Hz, 2H; H11,11'), 7.24 (d, ^3J(H,H) = 8.2 Hz, 2H; H4,5), 6.82 (d, ^3J(H,H) = 7.9 Hz, 2H; H12,12'), 6.55 (d, ^3J(H,H) = 7.7 Hz, 2H; H2,7), 3.76 (br., 2H; NH_2), 2.98 (s, 6H; H9,9').

^{13}C{^{1}H} NMR ($CDCl_3$, 125.8 MHz): δ = 146.4 (C13), 143.4 (C1,8), 136.0 (C4a), 133.3 (C11,11'), 127.4 (C3,6), 127.0* (C10), 120.6 (C8a), 118.0 (C4,5), 115.0 (C12,12'), 103.6 (C2,7), 35.8 (C9,9'). *) This signal was detected through a ^{H,C}HMBC NMR experiment.

^{11}B NMR ($CDCl_3$, 160.5 MHz): δ = 32.0 (s).

HRMS: Calculated *m/z* for $[C_{18}H_{18}BN_3]^{\bullet+}$: 287.15883, found: 287.15964.

2.7. Synthesis of compound $3^{Me,Me}$

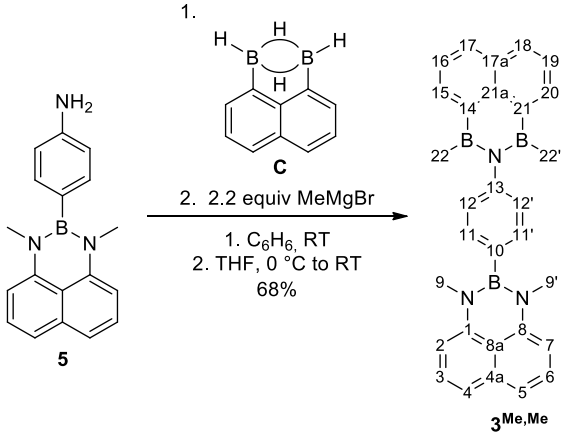

5 (51.0 mg, 0.178 mmol, 1 equiv) and the 1,8-naphthalenediyl-bridged diborane(6) **C** (27.0 mg, 0.178 mmol, 1 equiv) were suspended in C_6H_6 (2 mL) and stirred for 30 min at room temperature to afford a yellow suspension. All volatiles were removed from the reaction mixture under reduced pressure. The resulting yellow solid was suspended in THF (4 mL). MeMgBr (3.34 M in Et_2O, 0.12 mL, 0.40 mmol, 2.2 equiv) was added dropwise with stirring at 0 °C. The cooling bath was removed after 30 min and stirring continued for 2 h to yield a clear yellow solution. 1,4-Dioxane (0.5 mL) was added at room temperature, which resulted in a colorless precipitate after 1.5 h of stirring. The precipitate was filtered off and the filter cake washed with THF (2 × 0.5 mL). All volatiles were removed from the clear filtrate under reduced pressure, and C_6H_6 (4 mL) was added to give a yellow suspension. The flask was placed in an ultrasonic bath until the solid was homogeneously suspended and no solid remained stuck to the flask. The precipitate was collected on a frit and washed with C_6H_6 (2 mL) and Et_2O (3 × 4 mL) to afford product $\mathbf{3^{Me,Me}}$ as a yellow solid after drying in vacuo. Yield: 56.2 mg (0.121 mmol, 68%). Single crystals of $\mathbf{3^{Me,Me}}$·THF were obtained by gas-phase diffusion of *n*-hexane into a THF solution of $\mathbf{3^{Me,Me}}$.

^{1}H NMR ($CDCl_3$, 500.2 MHz): δ = 8.42 (dd, ^3J(H,H) = 6.8 Hz, ^4J(H,H) = 1.2 Hz, 2H; H15,20), 8.12 (dd, ^3J(H,H) = 8.2 Hz, ^4J(H,H) = 1.2 Hz, 2H; H17,18), 7.68 (dd, ^3J(H,H) = 6.8 Hz, ^3J(H,H) = 8.2 Hz, 2H; H16,19), 7.49 (d, ^3J(H,H) = 8.1 Hz, 2H; H11,11'), 7.34 (vt, 2H; H3,6), 7.23 (dd, ^3J(H,H) = 8.2 Hz, ^4J(H,H) = 0.8 Hz, 2H; H4,5), 7.14 (d, ^3J(H,H) = 8.1 Hz, 2H; H12,12'), 6.57 (d, ^3J(H,H) = 7.6 Hz, 2H; H2,7), 2.99 (s, 6H; H9,9'), 0.83 (s, 6H; H22,22').

^{13}C{^{1}H} NMR ($CDCl_3$, 125.8 MHz): δ = 149.1 (C13), 143.3 (C1,8), 138.3 (C15,20), 136.9 (C21a), 136.1 (C4a), 134.5* (C10 and C14,21), 133.0 (C17,18), 132.7 (C11,11'), 131.6 (C17a), 127.5 (C3,6), 127.5 (C12,12'), 125.9 (C16,19), 120.8 (C8a), 118.3 (C4,5), 103.8 (C2,7), 35.9 (C9,9'), 3.3* (C22,22'). *) This signal was detected through a ^{H,C}HSQC NMR experiment.

^{11}B NMR ($CDCl_3$, 160.5 MHz): δ = 49.5 (br.), 32.5 (br.).

HRMS: Calculated *m/z* for $[C_{30}H_{28}B_3N_3]^{\bullet+}$: 463.25569, found: 463.25663.

2.8. Synthesis of compound $3^{Me,Mes}$

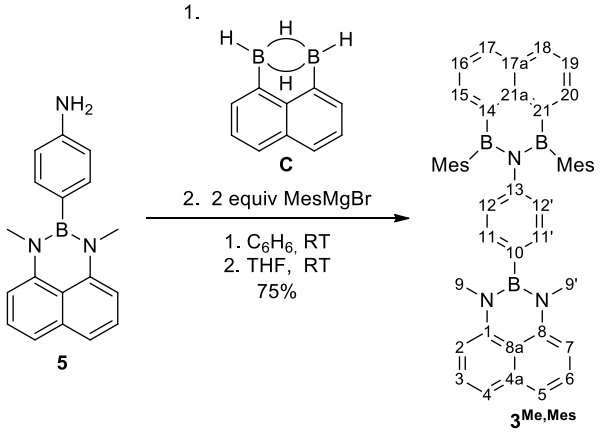

5 (200 mg, 0.696 mmol, 1 equiv) and the 1,8-naphthalenediyl-bridged diborane(6) **C** (106 mg, 0.696 mmol, 1 equiv) were suspended in C_6H_6 (4 mL) and stirred for 30 min at room temperature to afford a yellow suspension. All volatiles were removed from the reaction mixture. The resulting yellow solid was suspended in THF (4 mL). MesMgBr (1.56 M in THF, 0.92 mL, 1.4 mmol, 2 equiv) was added dropwise with stirring at room temperature to give a clear yellow solution. After 30 min, all volatiles were removed under reduced pressure to obtain a red foam, which was dissolved in C_6H_6 (5 mL) and filtered through a plug of neutral Al_2O_3. The plug was rinsed with C_6H_6 (4 × 20 mL). All volatiles were removed from the yellow filtrate under reduced pressure to yield a yellow oil, which solidified after 4 h at 60 °C under a dynamic vacuum. Yield: 352 mg (0.524 mmol, 75%). Yellow single crystals of $\mathbf{3^{Me,Mes}}\cdot C_6H_{14}$ were obtained by recrystallization of $\mathbf{3^{Me,Mes}}$ from *n*-hexane.

^{1}H NMR ($CDCl_3$, 500.2 MHz): δ = 8.17 (dd, ^3J(H,H) = 8.2 Hz, ^4J(H,H) = 1.0 Hz, 2H; H17,18), 7.94 (d, ^3J(H,H) = 6.9 Hz, 2H; H15,20), 7.61 (vt, 2H; H16,19), 7.28 (vt, 2H; H3,6), 7.17 (d, ^3J(H,H) = 8.1 Hz, 2H; H4,5), 7.02 (d, ^3J(H,H) = 8.2 Hz, 2H; H12,12'), 6.93 (d, ^3J(H,H) = 8.2 Hz, 2H; H11,11'), 6.70 (s, 4H; MesCH), 6.44 (d, ^3J(H,H) = 7.7 Hz, 2H; H2,7), 2.59 (s, 6H; H9,9'), 2.23 (s, 6H; $MesCH_3$-*p*), 2.19 (s, 12H; $MesCH_3$-*o*).

^{13}C{^{1}H} NMR ($CDCl_3$, 125.8 MHz): δ = 148.0 (C13), 143.3 (C1,8), 141.2 (C15,20), 138.5 (MesC-*o*), 138.3 (MesC-*i*), 137.2 (C21a), 136.7 (MesC-*p*), 136.0 (C4a), 134.1 (C10 and C14,21), 133.6 (C17,18), 131.6 (C17a), 130.7 (C11,11'), 127.4 (C3,6), 126.7 (MesCH), 126.3 (C16,19), 125.7 (C12,12'), 120.6 (C8a), 118.1 (C4,5), 103.5 (C2,7), 35.2 (C9,9'), 23.3 ($MesCH_3$-*o*), 21.3 ($MesCH_3$-*p*).

^{11}B NMR ($CDCl_3$, 160.5 MHz): δ = 53.0 (br.), 32.8 (br.).

HRMS: Calculated *m/z* for $[C_{46}H_{44}B_3N_3]^{\bullet+}$: 671.38089, found: 671.38387.

2.9. Synthesis of compound 6

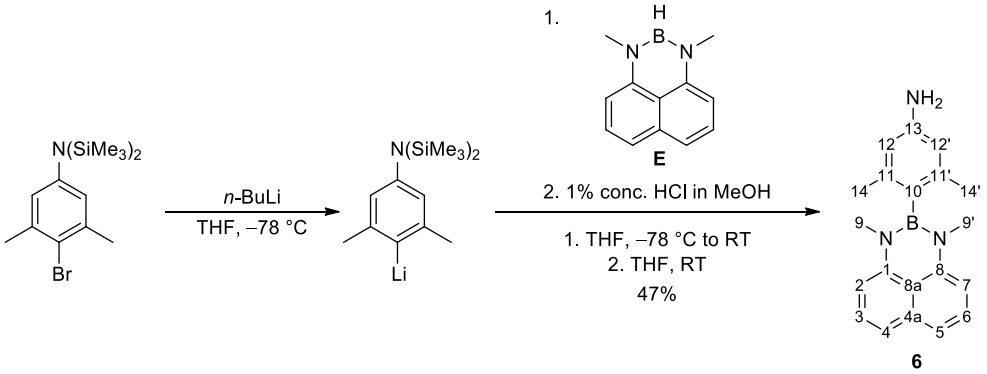

n-BuLi (2.37 M in *n*-hexane, 0.60 mL, 1.4 mmol, 1 equiv) was added dropwise with stirring at −78 °C to a solution of 2,6-Me_2-4-$(Me_3Si)_2N$-C_6H_2-Br (485 mg, 1.41 mmol, 1 equiv) in THF (3 mL).[S4] After rinsing the dropping funnel with *n*-hexane (1 mL), a suspension of **E** (276 mg, 1.41 mmol, 1 equiv) in THF (5 mL) was added dropwise at −78 °C. The remaining solid in the dropping funnel was rinsed into the reaction mixture with THF (2 × 2.5 mL). The reaction mixture was slowly warmed to room temperature in the course of 12 h, whereupon its color changed from brown to beige. A solution of HCl in MeOH (3 mL, 1 vol% conc. HCl) was added to the reaction mixture at room temperature, resulting in a color change from beige to green. All volatiles were removed under reduced pressure after 30 min of stirring at room temperature. The green solid was dissolved in Et_2O (10 mL) and a saturated aqueous solution of $NaHCO_3$ (10 mL) was added. The phases were separated and the aqueous phase was extracted with Et_2O (4 × 10 mL). The combined organic phases were dried over $MgSO_4$ and then filtered through a plug of neutral Al_2O_3. The plug was flushed with Et_2O (2 × 100 mL). All volatiles were removed from the filtrate to yield an orange oil, from which a colorless oily impurity was distilled off (120 °C, ca. 10^{-3} Torr) to afford product **6** as an off-white solid. Yield: 208 mg (0.660 mmol, 47%). Single crystals were obtained by recrystallization from *n*-hexane.

^{1}H NMR ($CDCl_3$, 500.2 MHz): δ = 7.32 (vt, 2H; H3,6), 7.21 (dd, ^3J(H,H) = 8.3 Hz, ^4J(H,H) = 0.8 Hz, 2H; H4,5), 6.52 (d, ^3J(H,H) = 7.6 Hz, 2H; H2,7), 6.45 (s, 2H; H12,12'), 3.61 (br., 2H; NH_2), 2.89 (s, 6H; H9,9'), 2.14 (s, 6H; H14,14').

^{13}C{^{1}H} NMR ($CDCl_3$, 125.8 MHz): δ = 146.5 (C13), 143.3 (C1,8), 140.9 (C11,11'), 136.0 (C4a), 128.1* (C10), 127.4 (C3,6), 120.6 (C8a), 118.0 (C4,5), 113.6 (C12,12'), 103.5 (C2,7), 34.5 (C9,9'), 22.0 (C14,14').
*) This signal was detected through a ^{H,C}HSQC NMR experiment.

^{11}B NMR ($CDCl_3$, 160.5 MHz): δ = 32.8 (s).

HRMS: Calculated *m/z* for $[C_{20}H_{22}BN_3]^{\bullet+}$: 315.19013, found: 315.19125.

2.10. Synthesis of compound $4^{Me,Mes}$

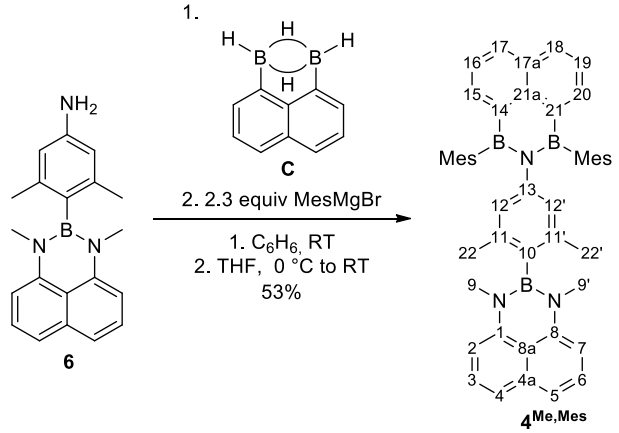

6 (149.0 mg, 0.473 mmol, 1 equiv) and the 1,8-naphthalenediyl-bridged diborane(6) **C** (71.8 mg, 0.473 mmol, 1 equiv) were suspended in C_6H_6 (4 mL) at room temperature and stirred for 30 min to afford a yellow solution. All volatiles were removed from the reaction mixture. The resulting yellow solid was dissolved in THF (4 mL). MesMgBr (1.55 M in THF, 0.73 mL, 1.1 mmol, 2.3 equiv) was added dropwise with stirring at 0 °C. The cooling bath was removed after 15 min and stirring continued at room temperature. After 3.5 h, all volatiles were removed under reduced pressure. The resulting red foam was dissolved in C_6H_6 (5 mL) and the solution filtered through a plug of neutral Al_2O_3. The plug was flushed with C_6H_6 (3 × 20 mL). All volatiles were removed under reduced pressure to give a yellow resin. Recrystallization of the resin from acetonitrile (31 mL) yielded $\mathbf{4^{Me,Mes}}$ as brown single crystals suitable for X-ray analysis. Yield: 174 mg (0.249 mmol, 53%).

^{1}H NMR ($CDCl_3$, 500.2 MHz): δ = 8.16 (dd, ^3J(H,H) = 8.1 Hz, ^4J(H,H) = 1.1 Hz, 2H; H17,18), 7.93 (d, ^3J(H,H) = 6.9 Hz, 2H; H15,20), 7.60 (dd, ^3J(H,H) = 8.1 Hz, ^3J(H,H) = 6.9 Hz, 2H; H16,19), 7.30 (vt, 2H; H3,6), 7.19 (d, ^3J(H,H) = 8.1 Hz, 2H; H4,5), 6.69 (s, 4H; MesCH), 6.64 (s, 2H; H12,12'), 6.46 (d, ^3J(H,H) = 7.6 Hz, 2H; H2,7), 2.54 (s, 6H; H9,9'), 2.24 (s, 6H; $MesCH_3$-*p*), 2.19 (s, 12H; $MesCH_3$-*o*), 1.91 (s, 6H; H22,22').

^{13}C{^{1}H} NMR ($CDCl_3$, 125.8 MHz): δ = 148.1 (C13), 143.2 (C1,8), 141.1 (C15,20), 138.5 (MesC-*o*), 138.2 (C11,11'), 137.2 (C21a), 136.5 (MesC-*p*), 136.0 (C4a), 134.2 (br., C10 and C14,21), 133.4 (C17,18), 131.6 (C17a), 127.4 (C3,6), 126.5 (MesCH), 126.3 (C16,19), 124.0 (C12,12'), 120.6 (C8a), 118.0 (C4,5), 103.4 (C2,7), 33.9 (C9,9'), 23.3 ($MesCH_3$-*o*), 21.4 (C22,22'), 21.3 ($MesCH_3$-*p*); n.o. (MesC-*i*).

^{11}B NMR ($CDCl_3$, 160.5 MHz): δ = 52.1 (br.), 33.1 (br.).

HRMS: Calculated *m/z* for $[C_{48}H_{48}B_3N_3]^{\bullet+}$: 699.41219, found: 699.41479.

3. Plots of ^{1}H, $^{13}C\{^{1}H\}$, and ^{11}B NMR Spectra

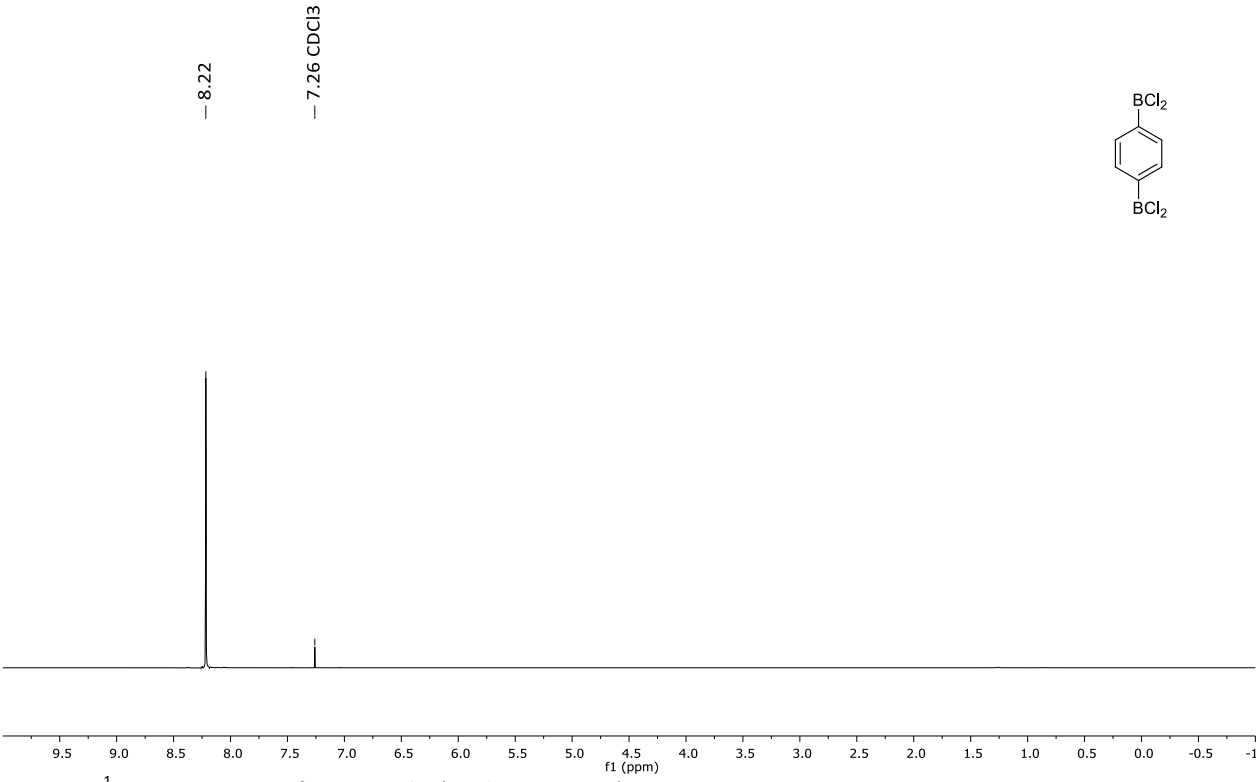

Figure S1: ^{1}H NMR spectrum of compound **B** ($CDCl_3$, 500.2 MHz).

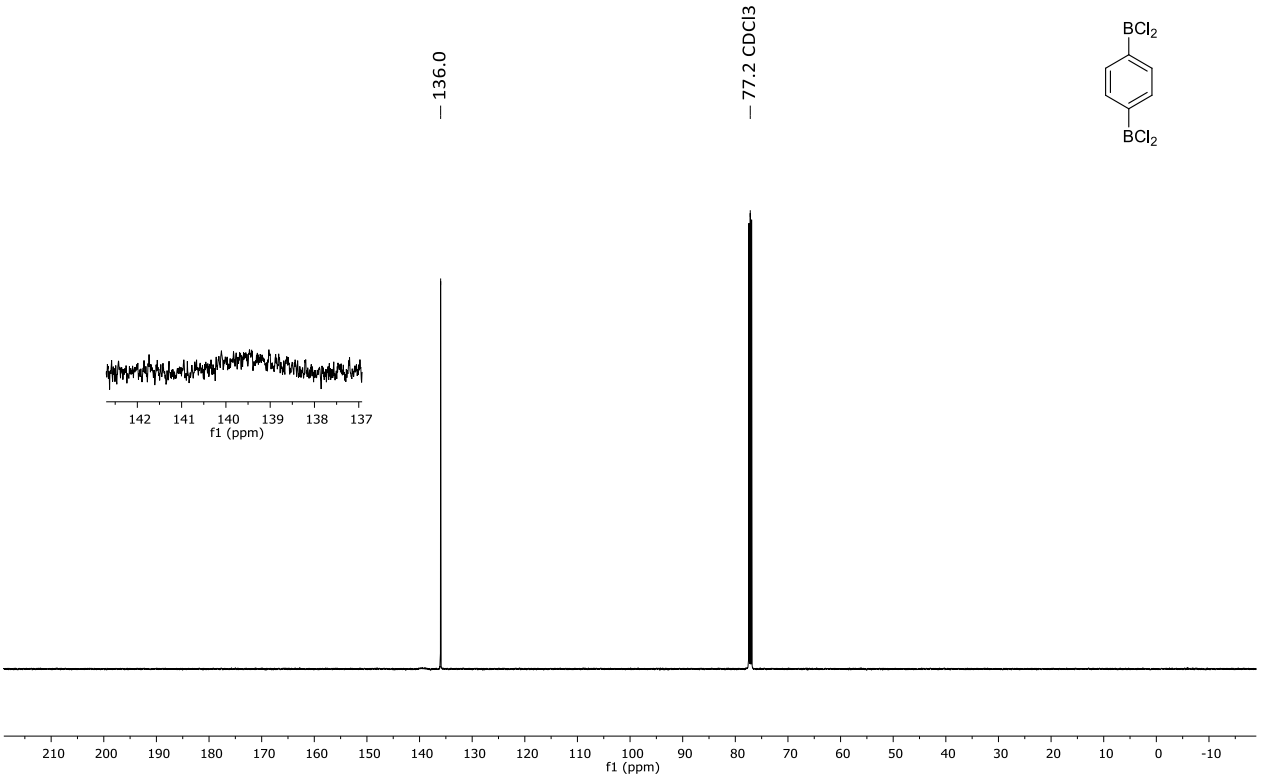

Figure S2: $^{13}C\{^{1}H\}$ NMR spectrum of compound **B** ($CDCl_3$, 125.8 MHz).

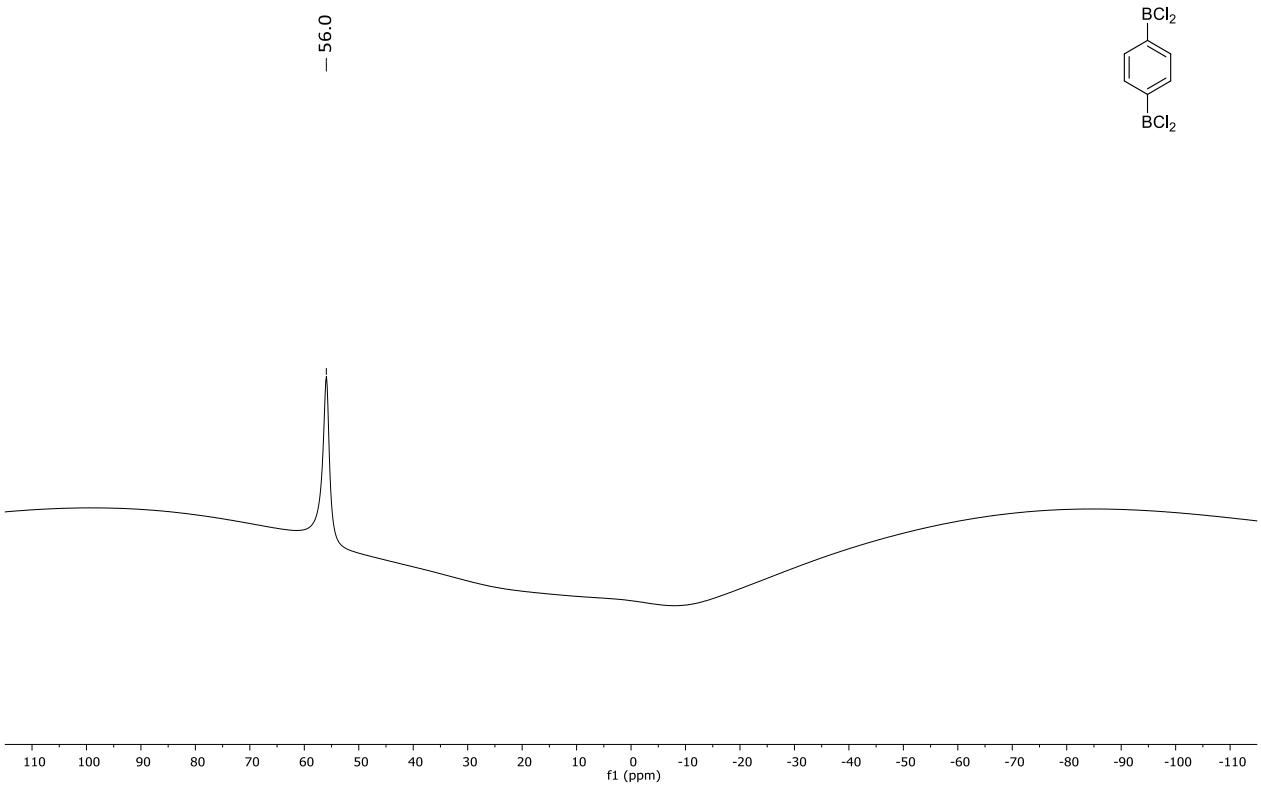

Figure S3: ^{11}B NMR spectrum of compound **B** ($CDCl_3$, 160.5 MHz).

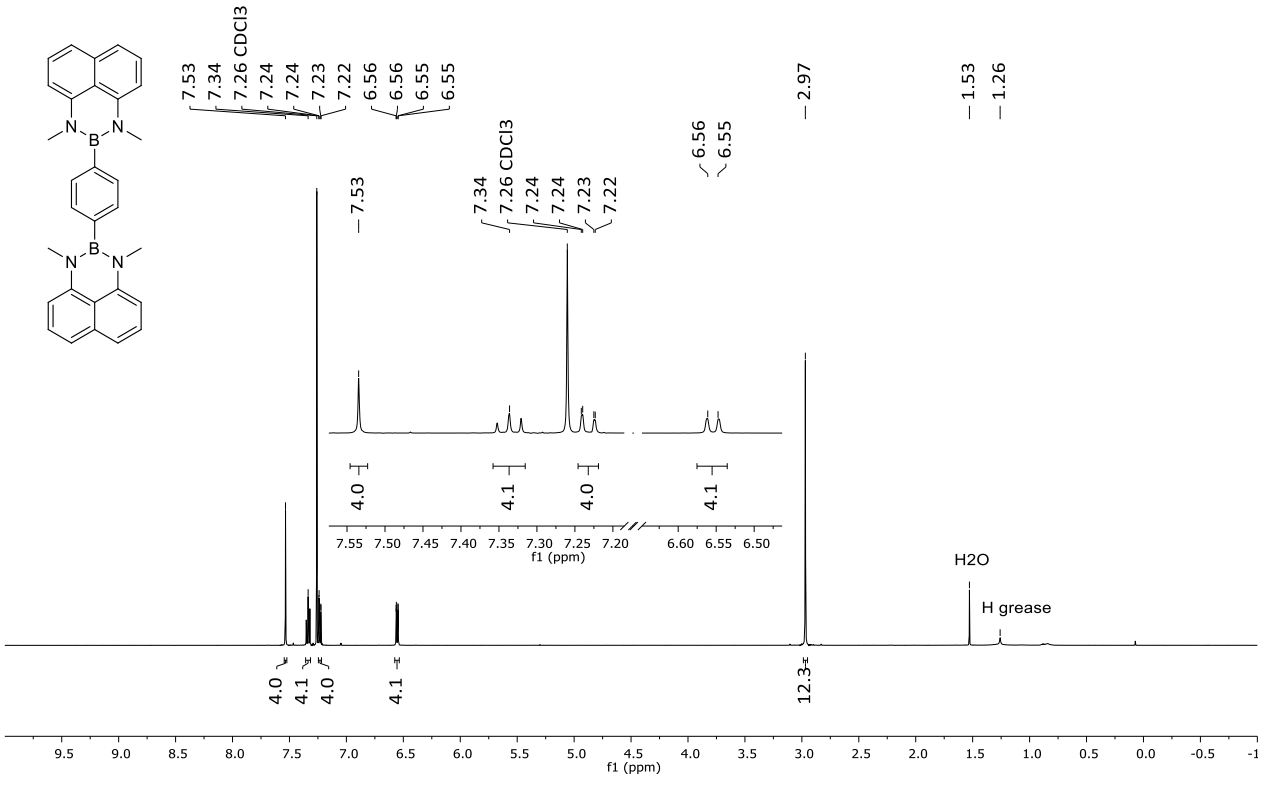

Figure S4: ^{1}H NMR spectrum of compound **1^{Me}** ($CDCl_3$, 500.2 MHz).

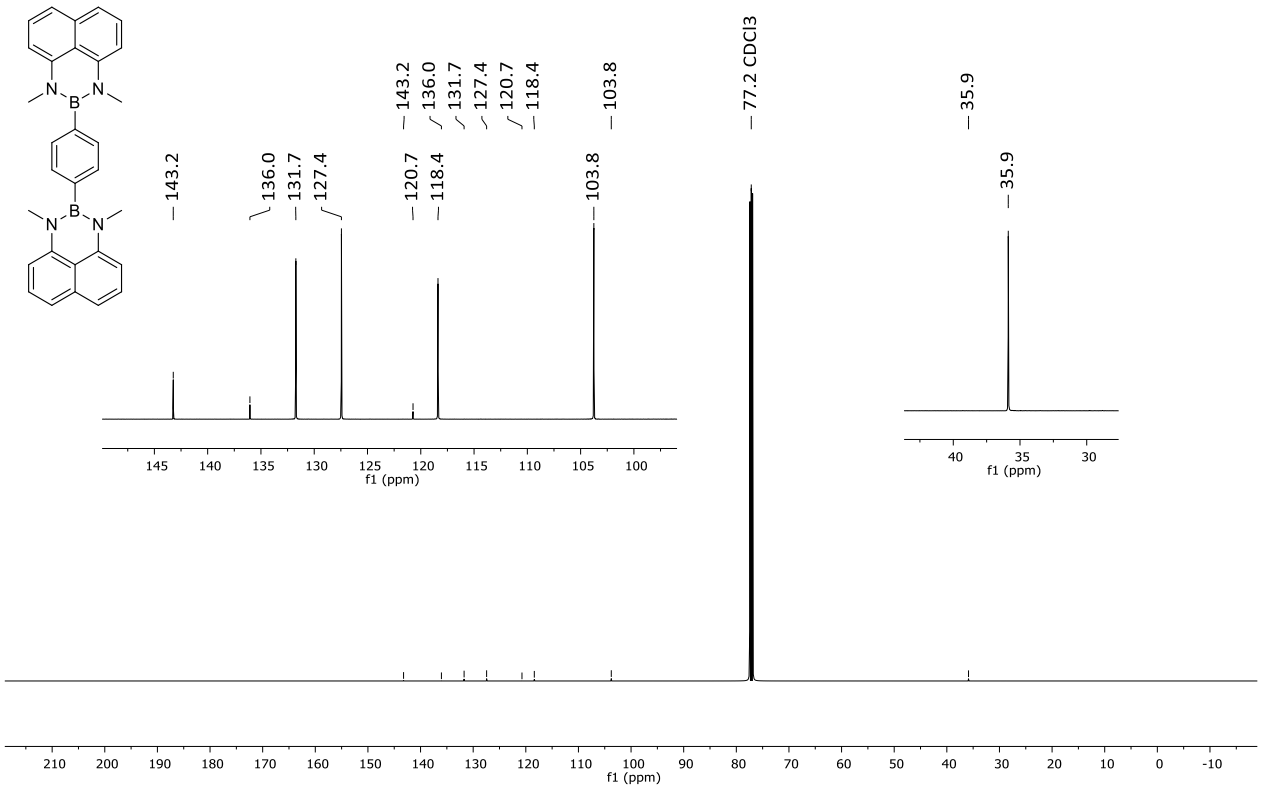

Figure S5: $^{13}C\{^{1}H\}$ NMR spectrum of compound **1**^{Me} ($CDCl_3$, 125.8 MHz).

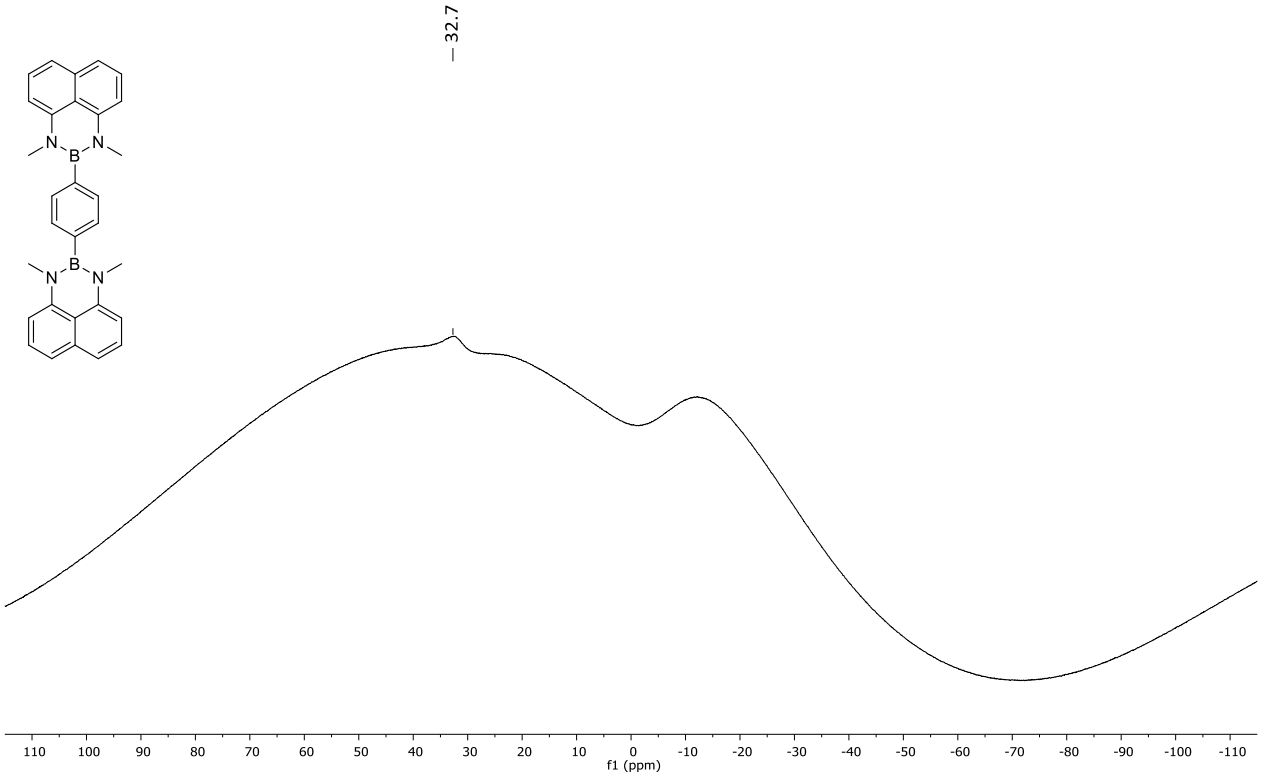

Figure S6: ^{11}B NMR spectrum of compound **1**^{Me} ($CDCl_3$, 160.5 MHz).

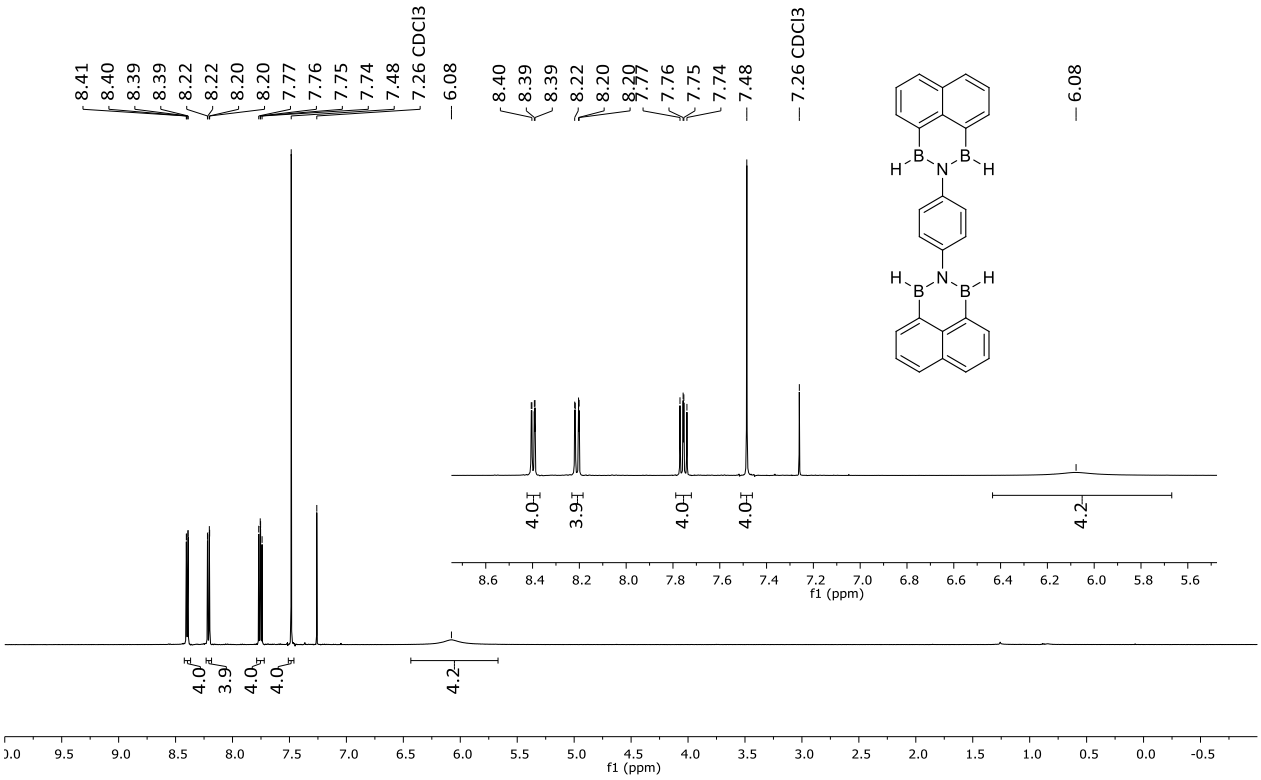

Figure S7: ^{1}H NMR spectrum of compound **2^{H}** ($CDCl_3$, 500.2 MHz).

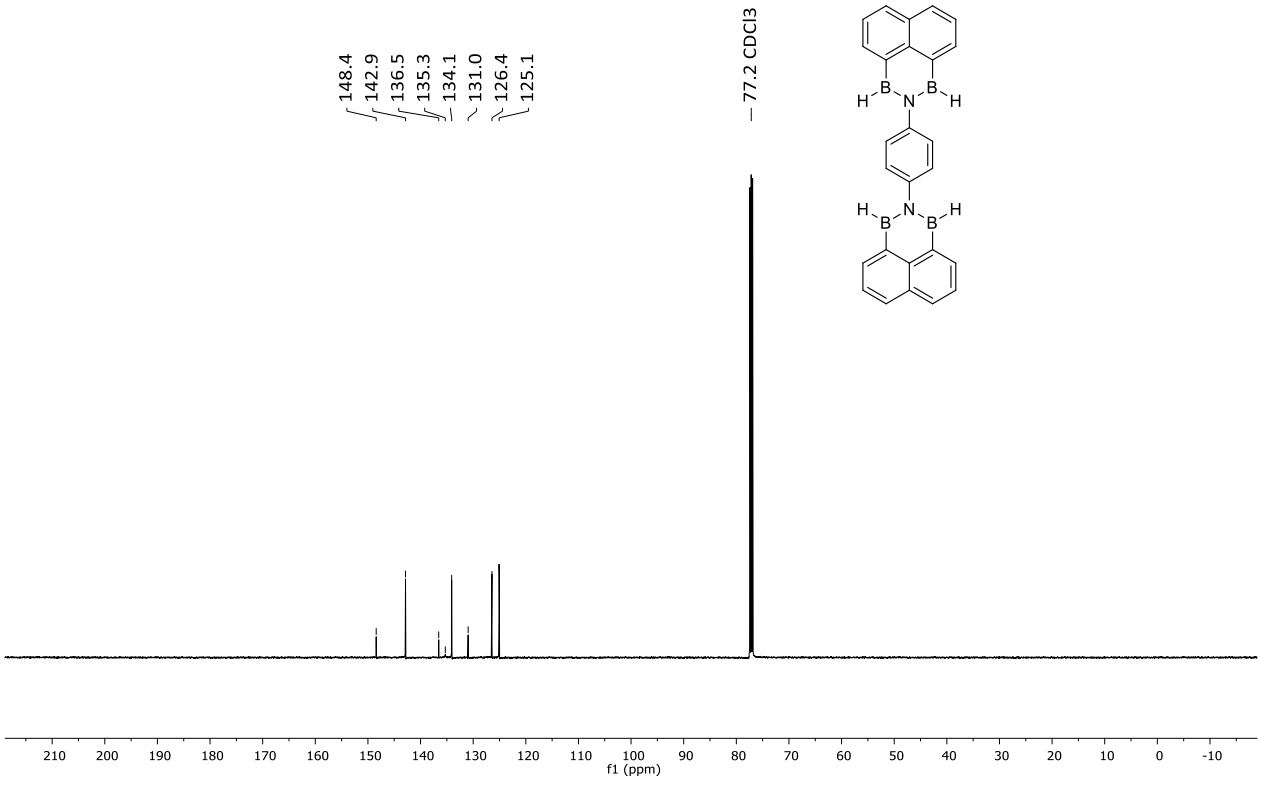

Figure S8: $^{13}C\{^{1}H\}$ NMR spectrum of compound **2^{H}** ($CDCl_3$, 125.8 MHz).

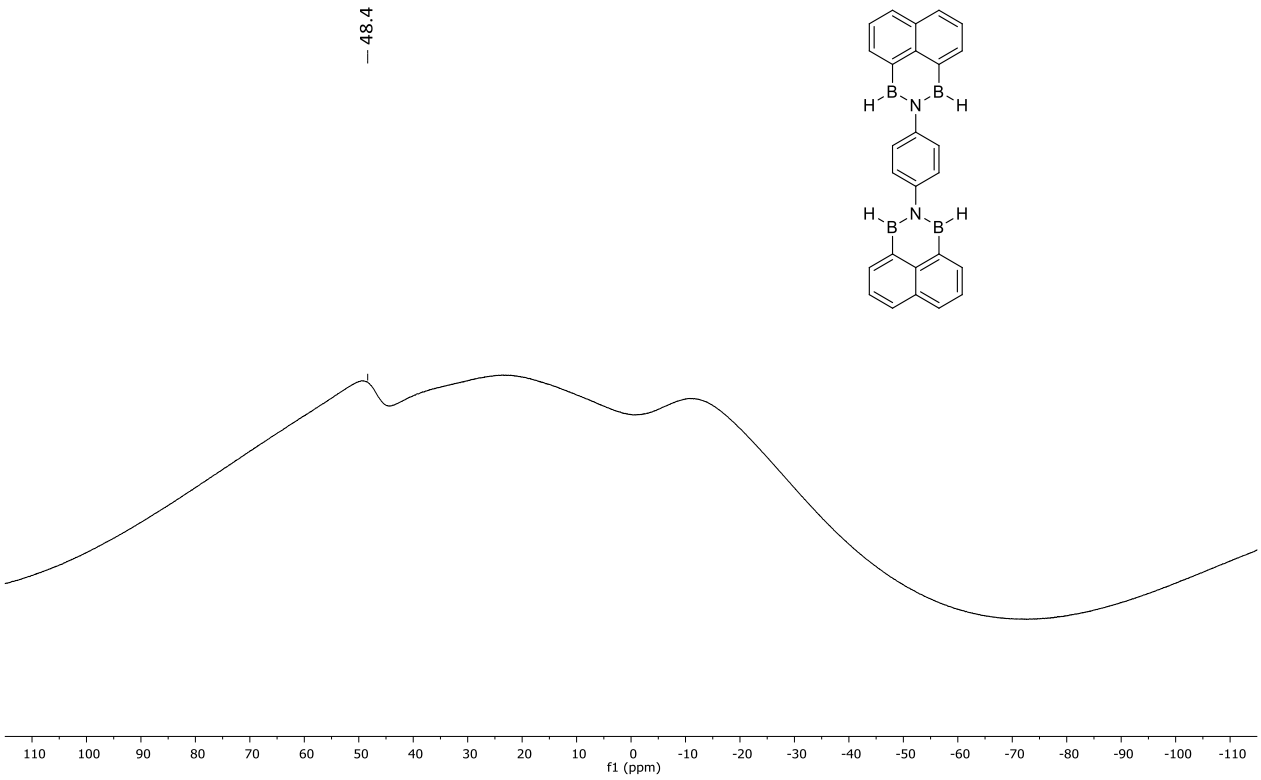

Figure S9: ^{11}B NMR spectrum of compound **2^{H}** ($CDCl_3$, 160.5 MHz).

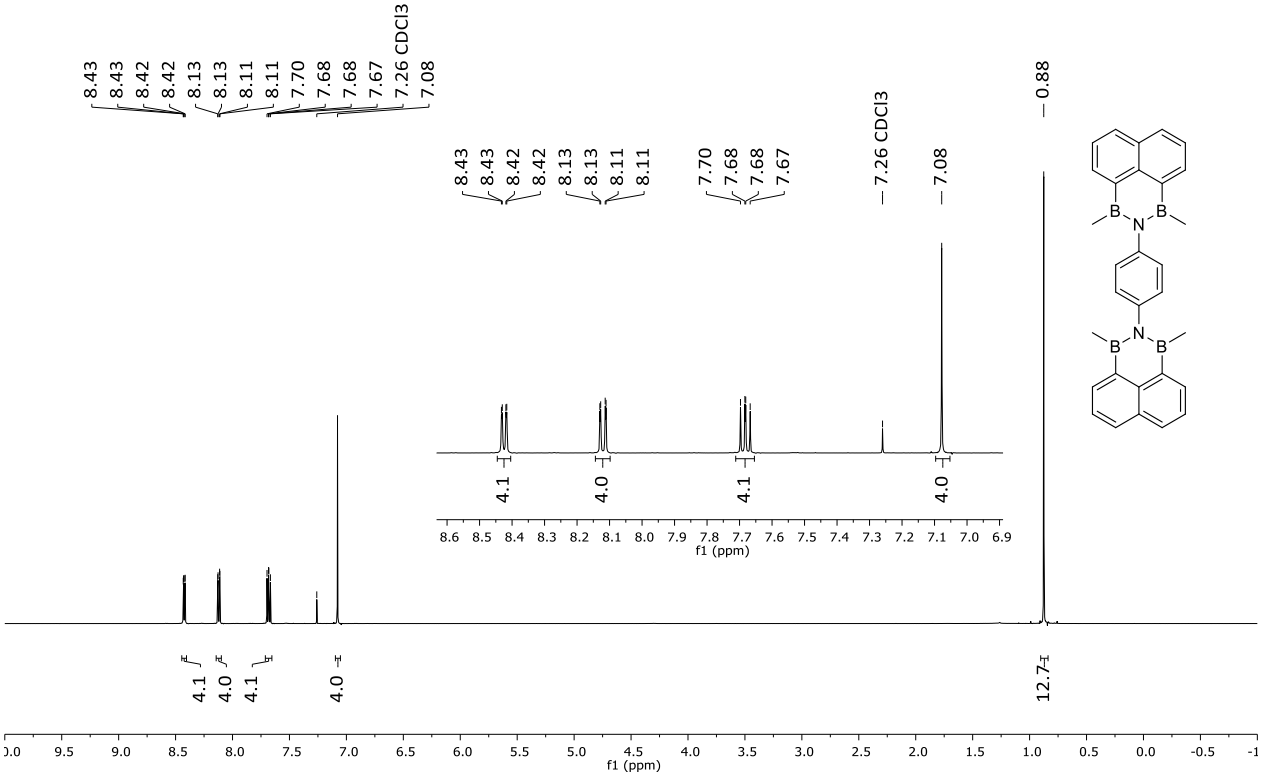

Figure S10: ^{1}H NMR spectrum of compound **2^{Me}** ($CDCl_3$, 500.2 MHz).

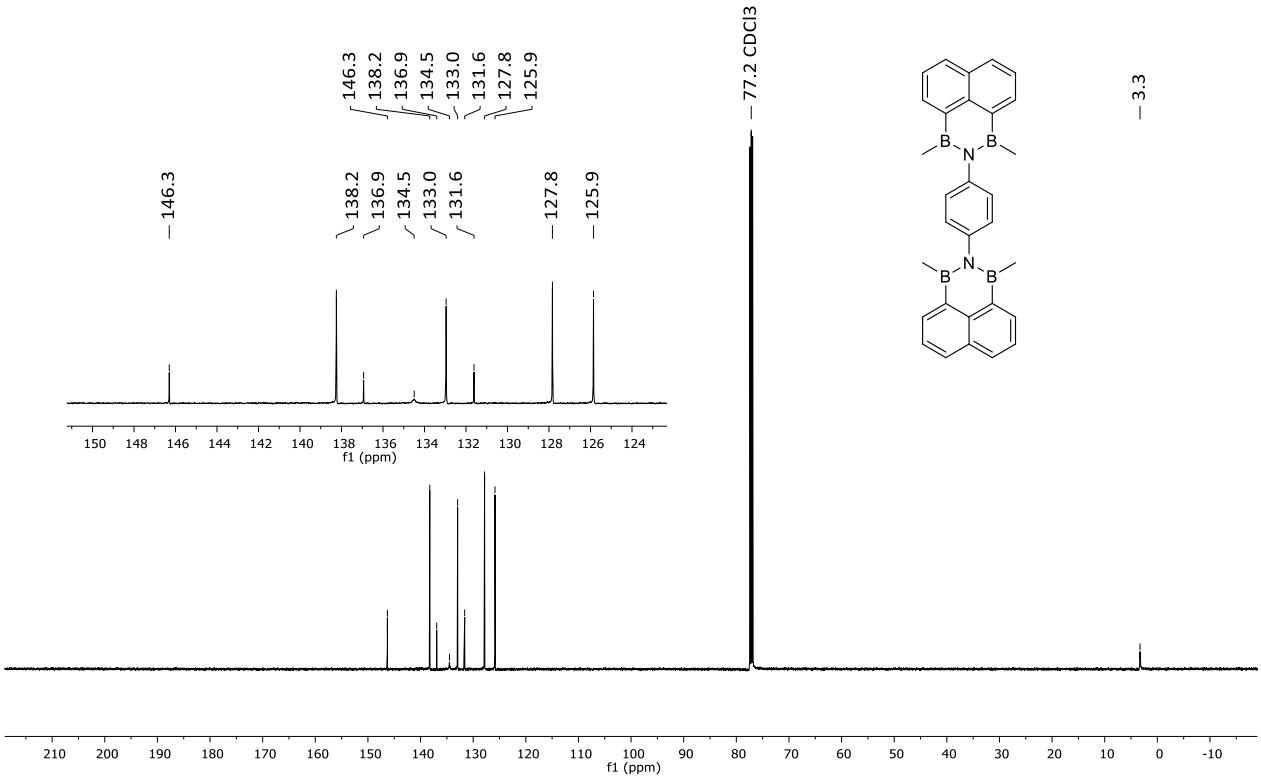

Figure S11: $^{13}C\{^{1}H\}$ NMR spectrum of compound **2^{Me}** ($CDCl_3$, 125.8 MHz).

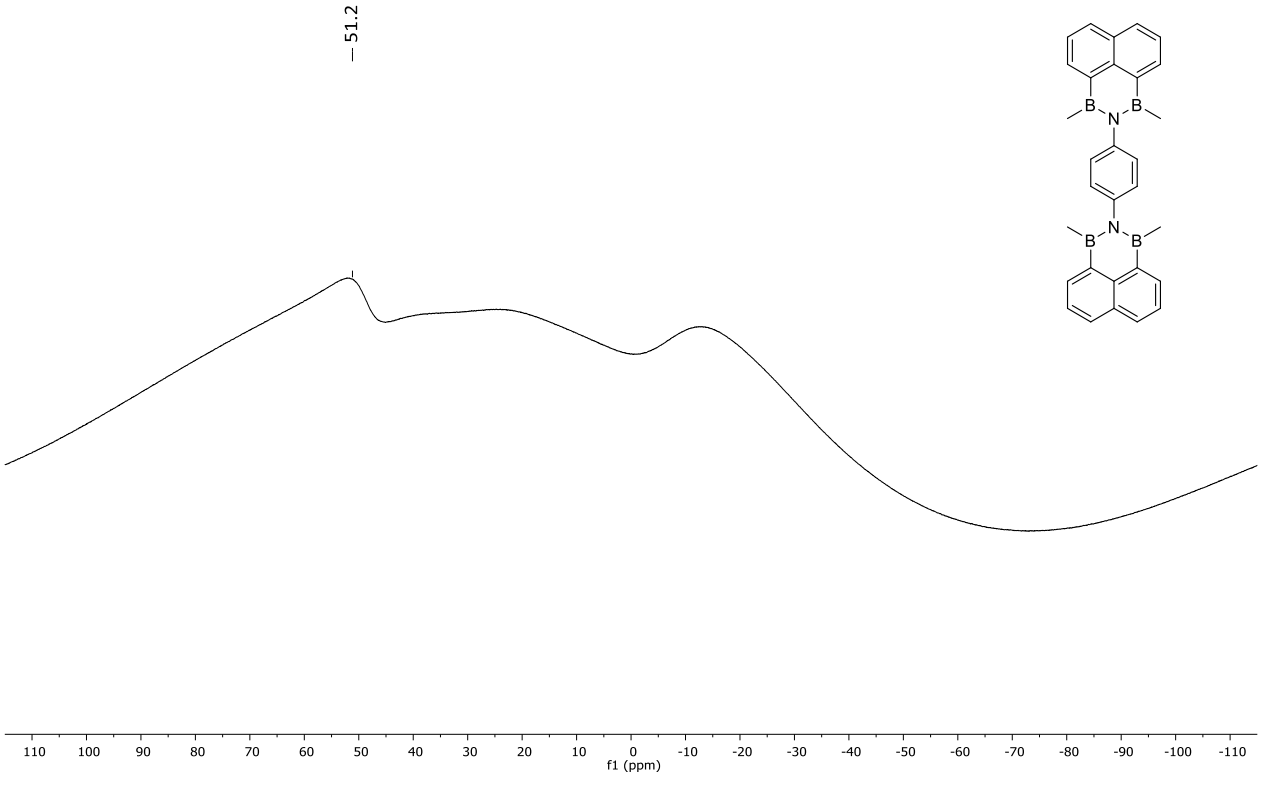

Figure S12: ^{11}B NMR spectrum of compound **2^{Me}** ($CDCl_3$, 160.5 MHz).

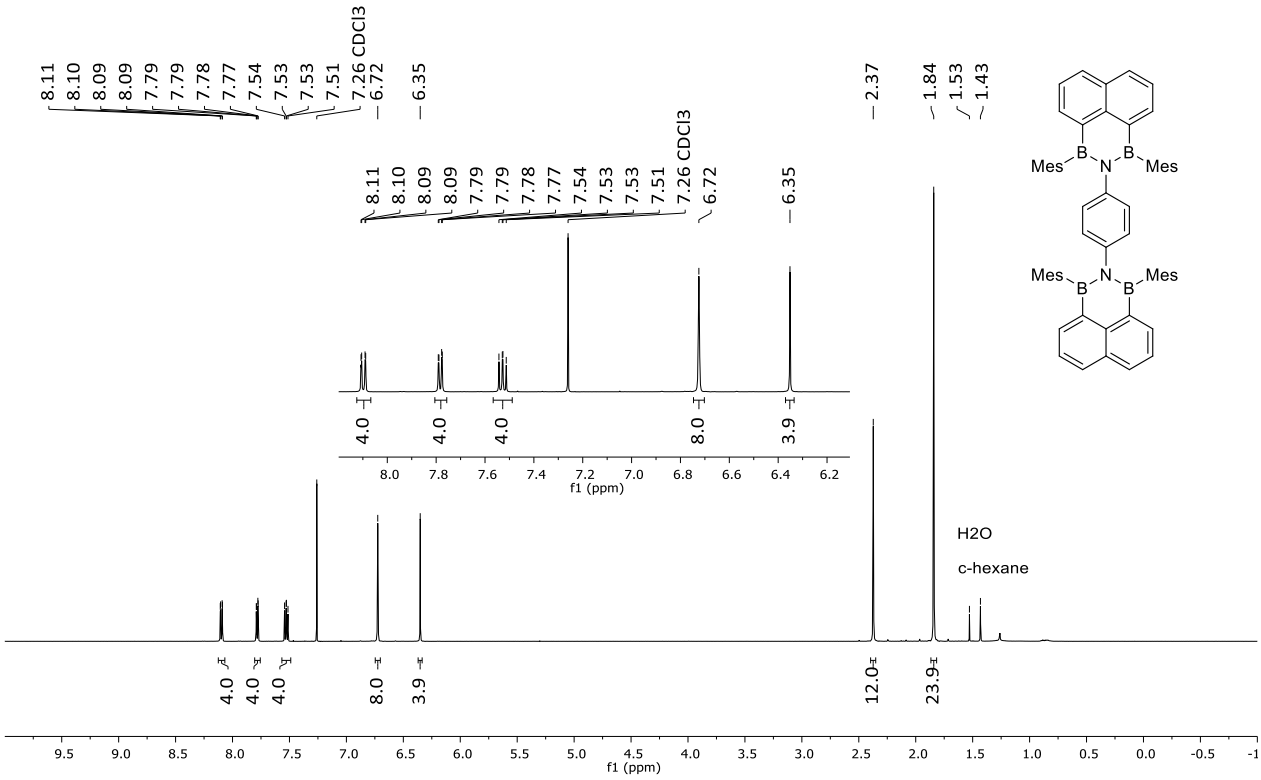

Figure S13: ^{1}H NMR spectrum of compound **2**$^{\mathbf{Mes}}$ ($CDCl_3$, 500.2 MHz).

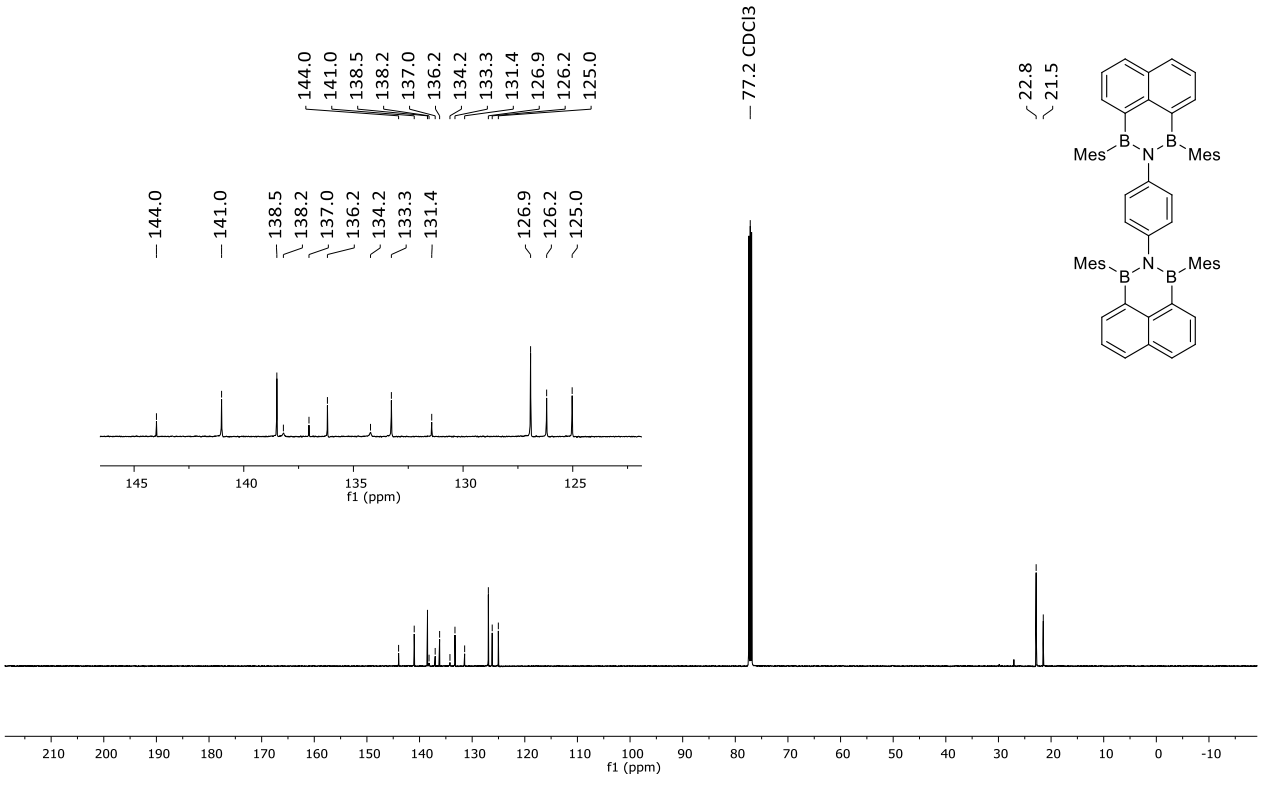

Figure S14: $^{13}C\{^{1}H\}$ NMR spectrum of compound **2**$^{\mathbf{Mes}}$ ($CDCl_3$, 125.8 MHz).

Figure 15: ^{11}B NMR spectrum of compound **2**$^{\mathbf{Mes}}$ ($CDCl_3$, 160.5 MHz).

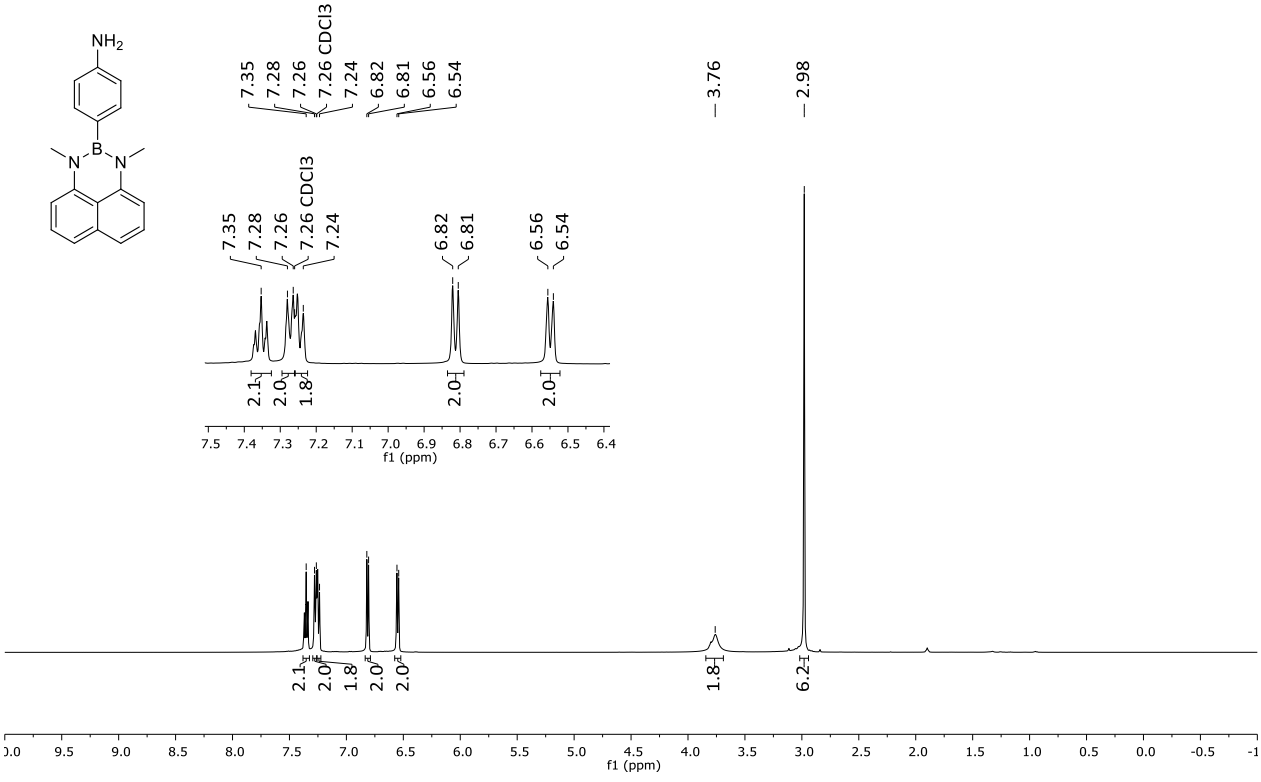

Figure S16: ^{1}H NMR spectrum of compound **5** ($CDCl_3$, 500.2 MHz).

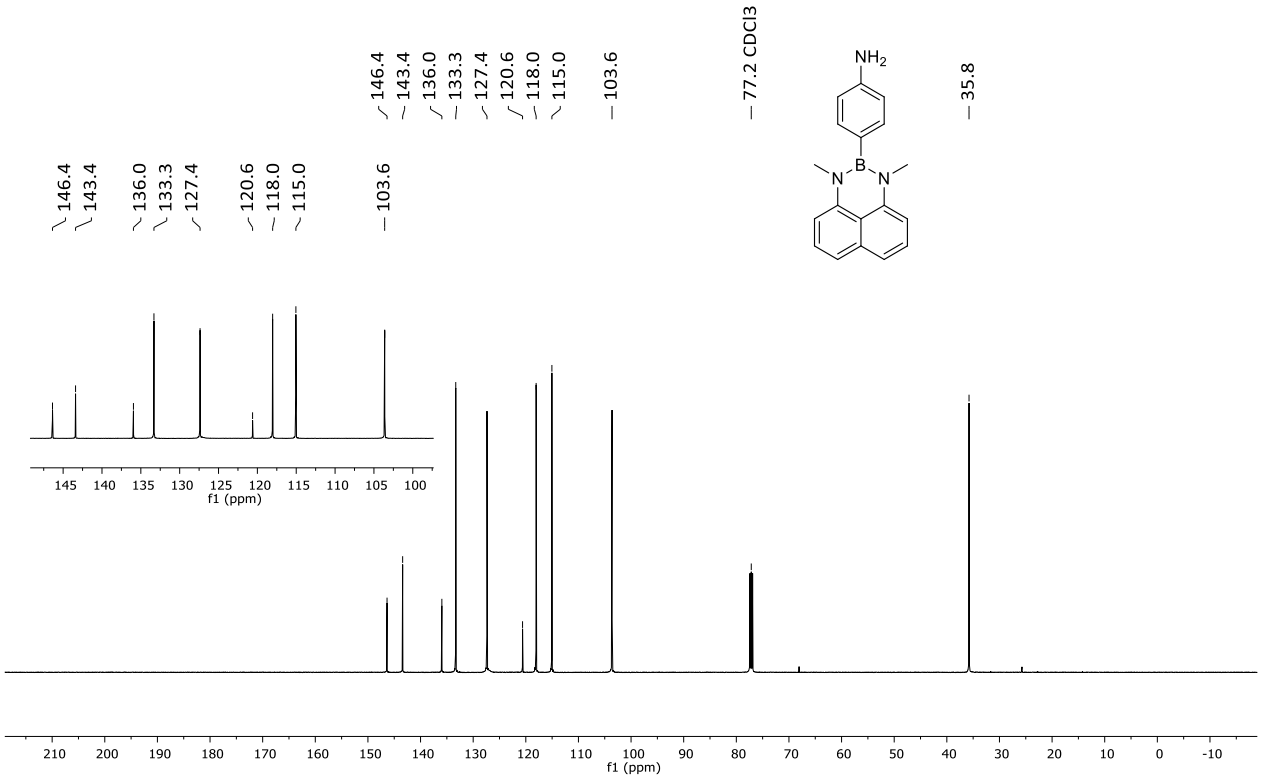

Figure S17: $^{13}C\{^{1}H\}$ NMR spectrum of compound **5** ($CDCl_3$, 125.8 MHz).

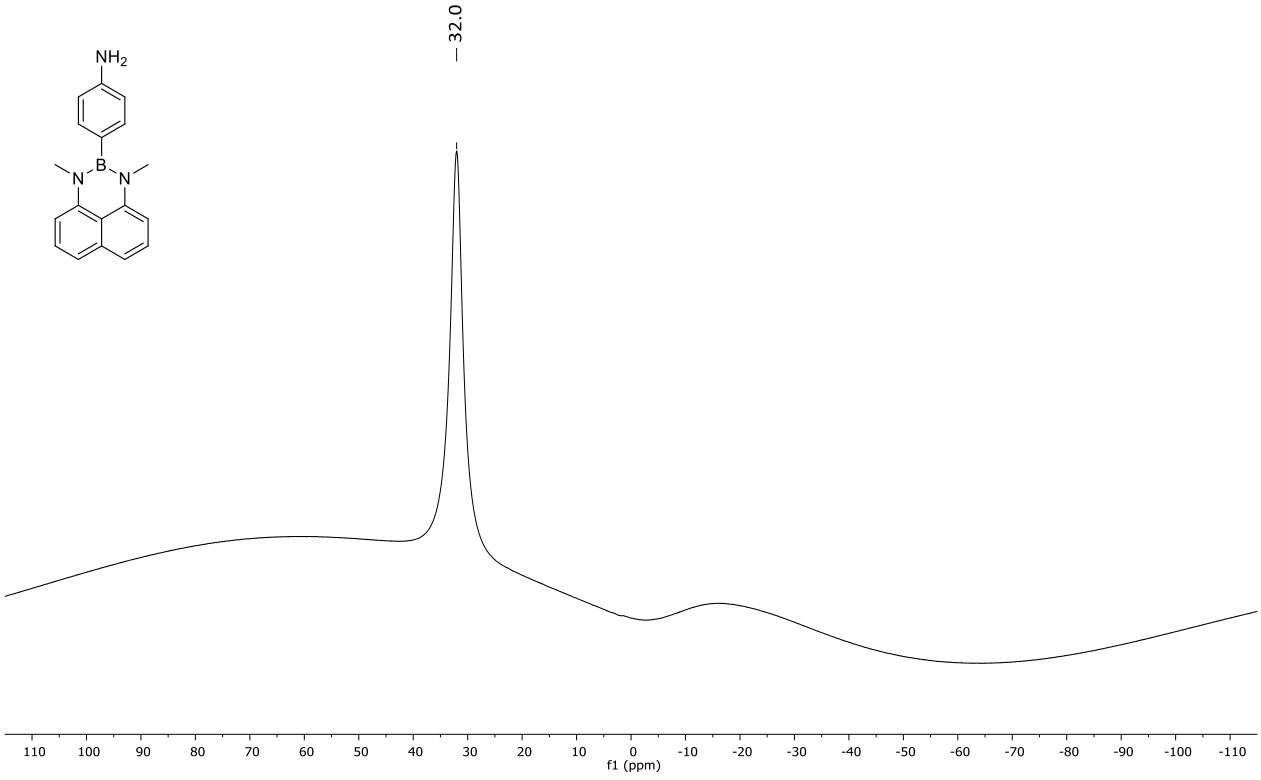

Figure S18: ^{11}B NMR spectrum of compound **5** ($CDCl_3$, 160.5 MHz).

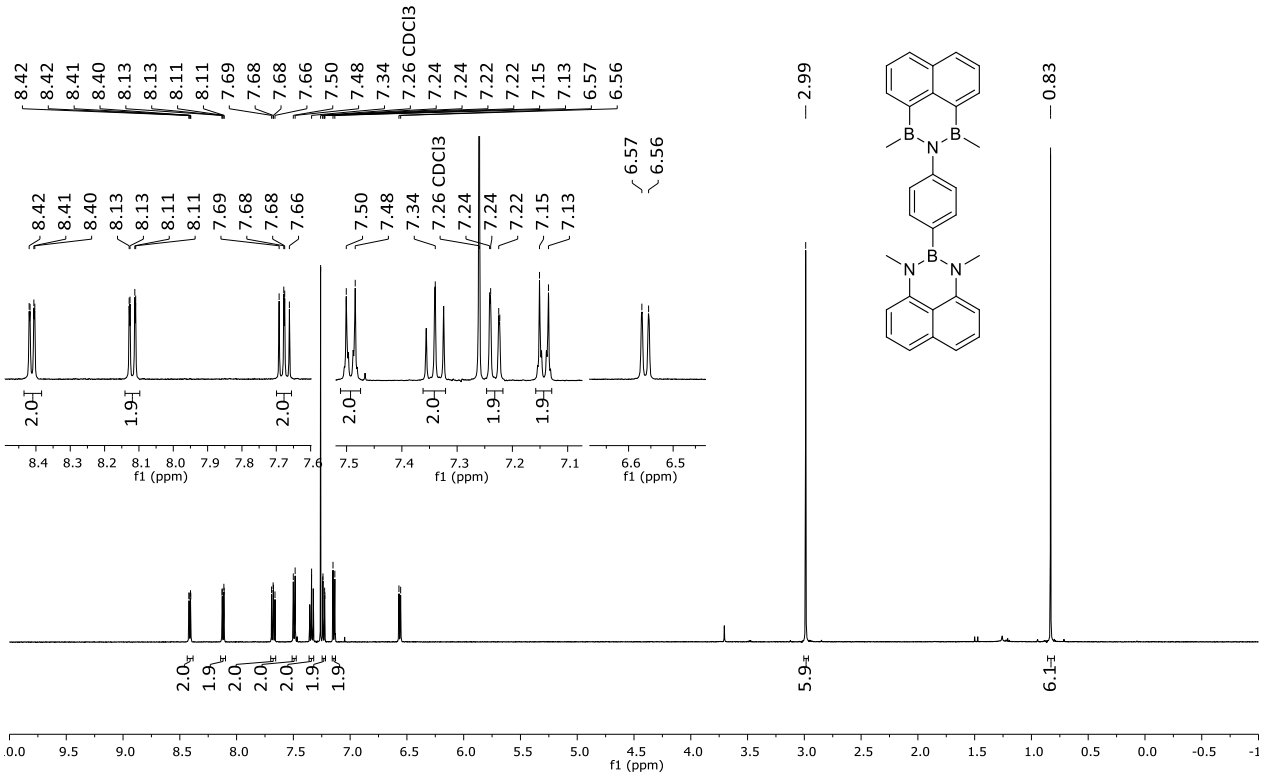

Figure S19: ^{1}H NMR spectrum of compound **3**$^{\mathbf{Me,Me}}$ ($CDCl_3$, 500.2 MHz).

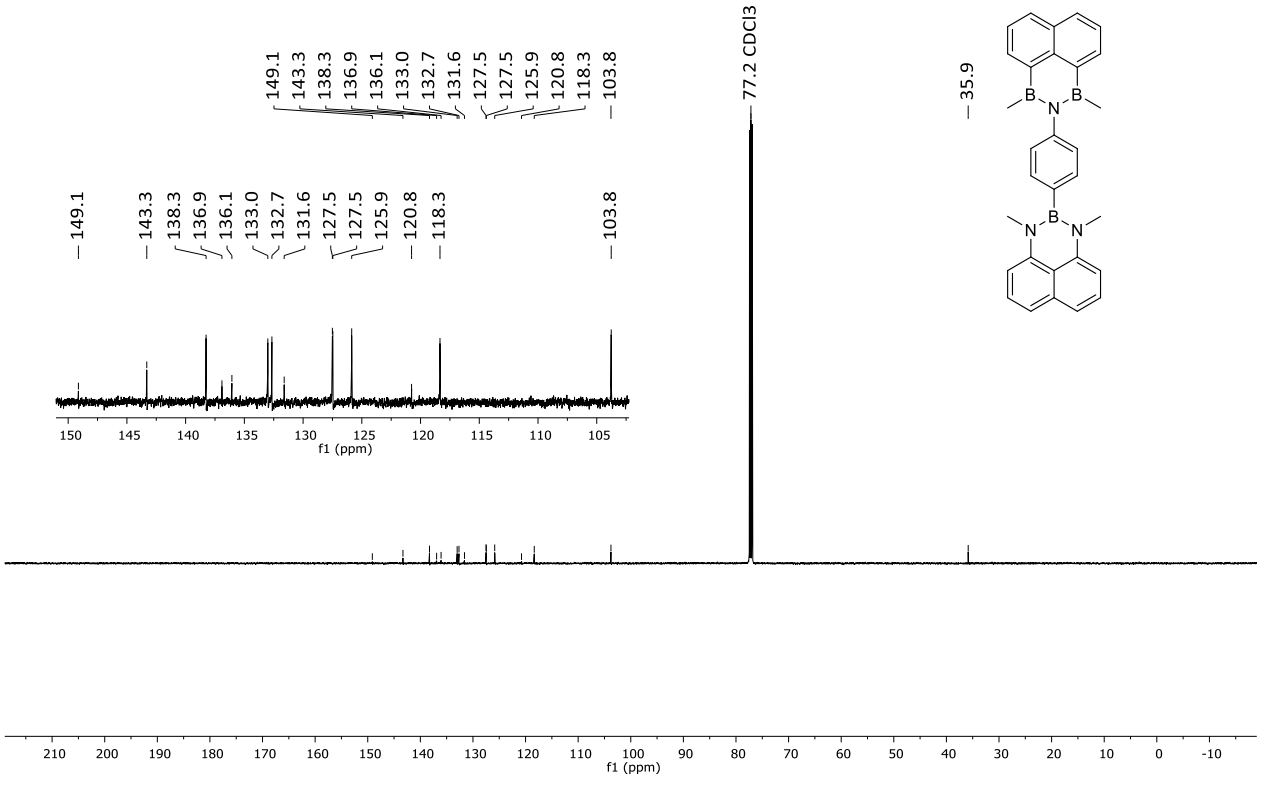

Figure S20: ^{13}C{^{1}H} NMR spectrum of compound **3**$^{\mathbf{Me,Me}}$ ($CDCl_3$, 125.8 MHz).

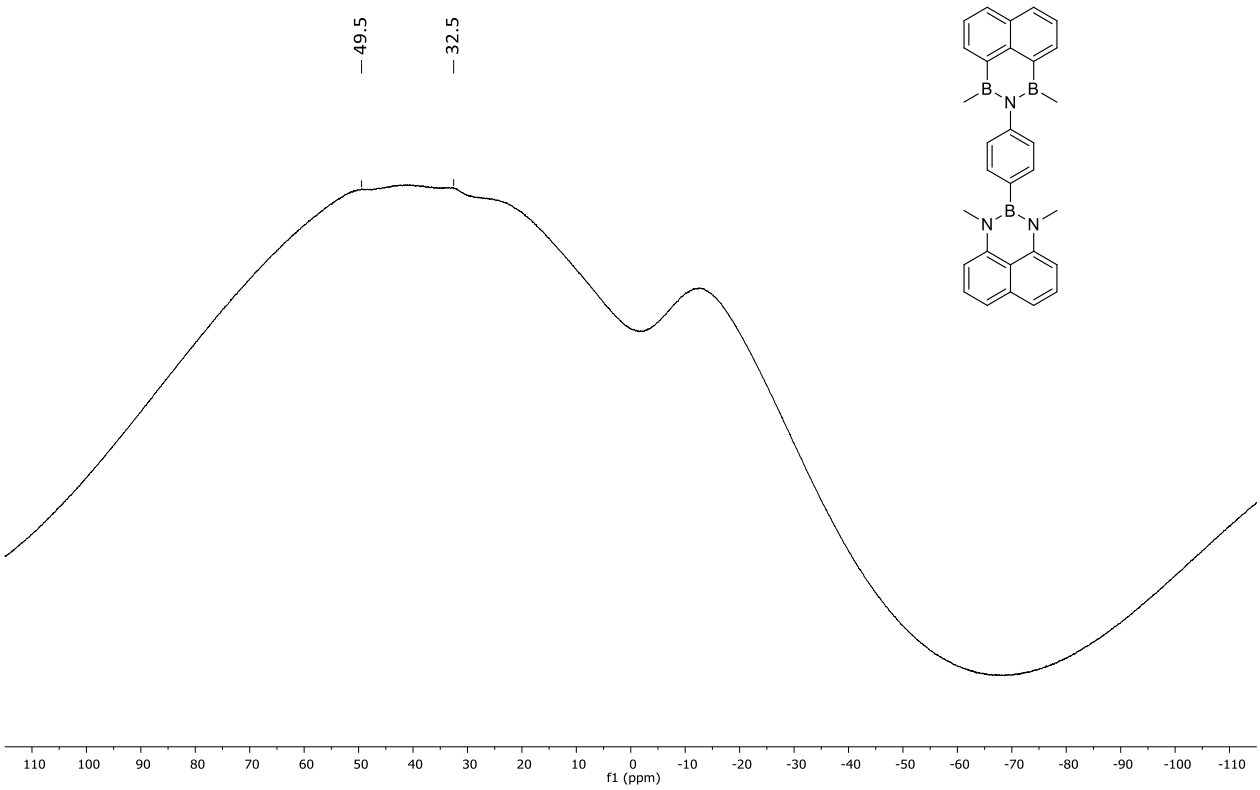

Figure 21: ^{11}B NMR spectrum of compound **3**^{Me,Me} ($CDCl_3$, 160.5 MHz).

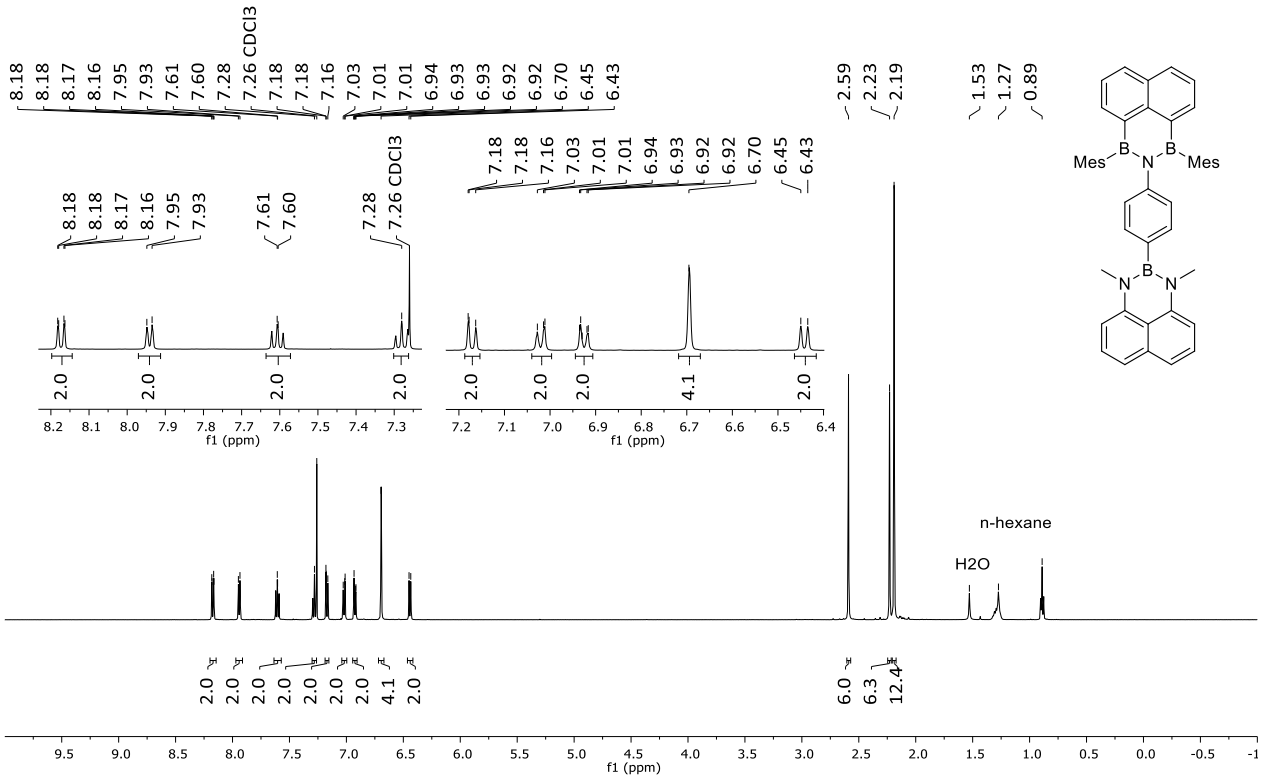

Figure S22: ^{1}H NMR spectrum of compound **3**^{Me,Mes} ($CDCl_3$, 500.2 MHz).

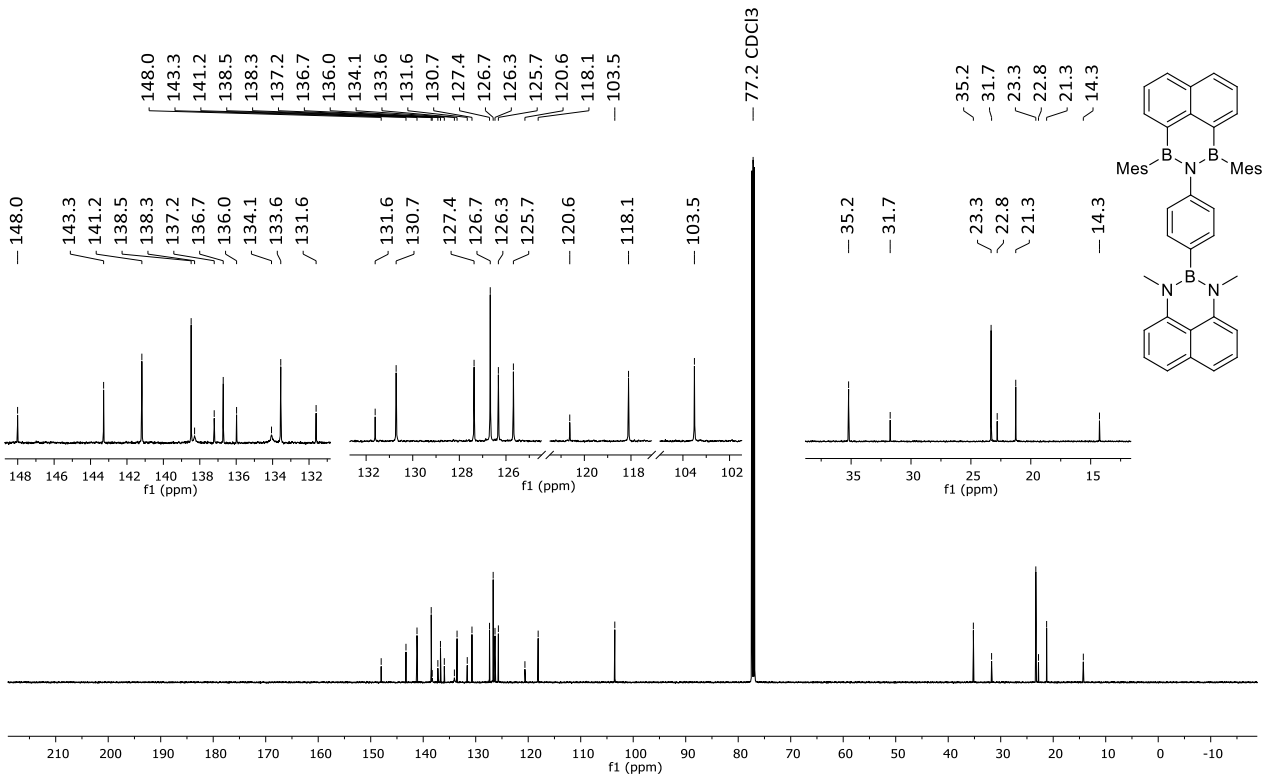

Figure S23: $^{13}C\{^{1}H\}$ NMR spectrum of compound $\mathbf{3}^{\mathbf{Me,Mes}}$ ($CDCl_3$, 125.8 MHz). As in the ^{1}H NMR spectrum (Figure S22), there is still *n*-hexane present in the sample (δ = 31.7, 22.8, and 14.3), which cannot be removed from the crystals.

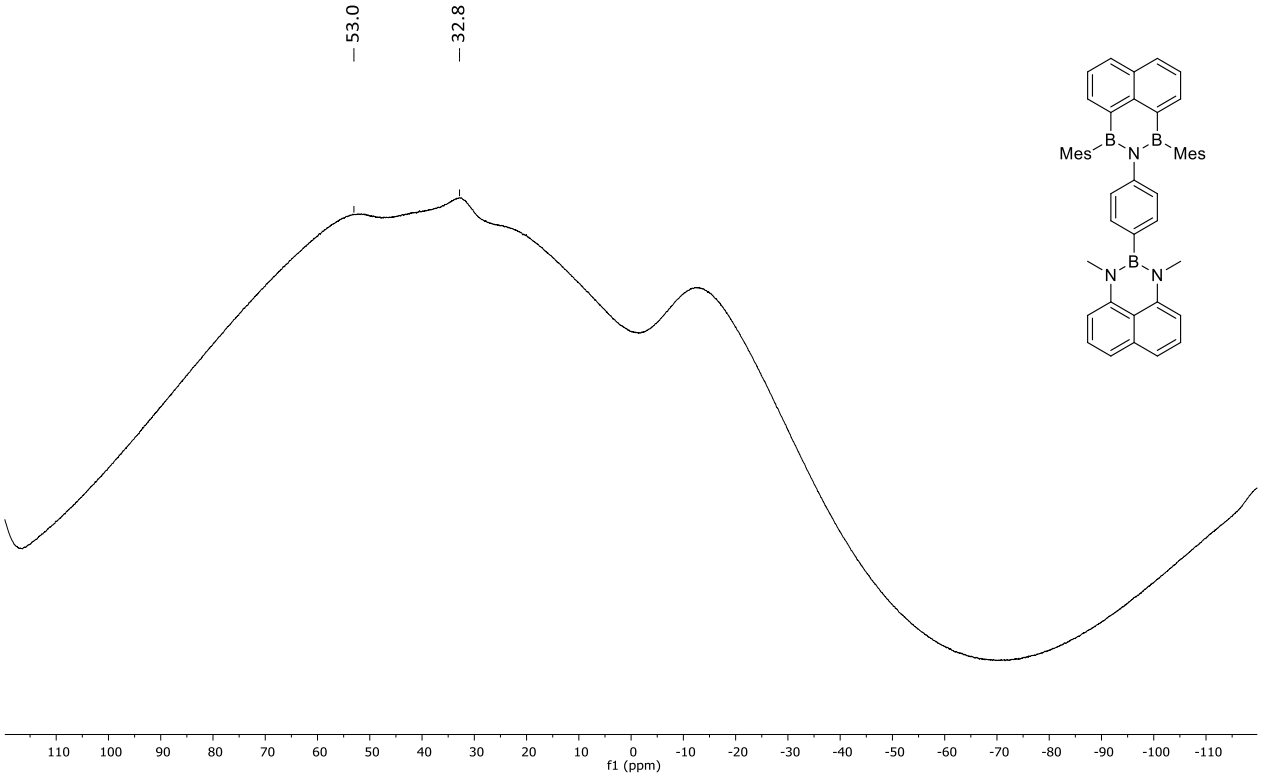

Figure S24: ^{11}B NMR spectrum of compound $\mathbf{3}^{\mathbf{Me,Mes}}$ ($CDCl_3$, 160.5 MHz).

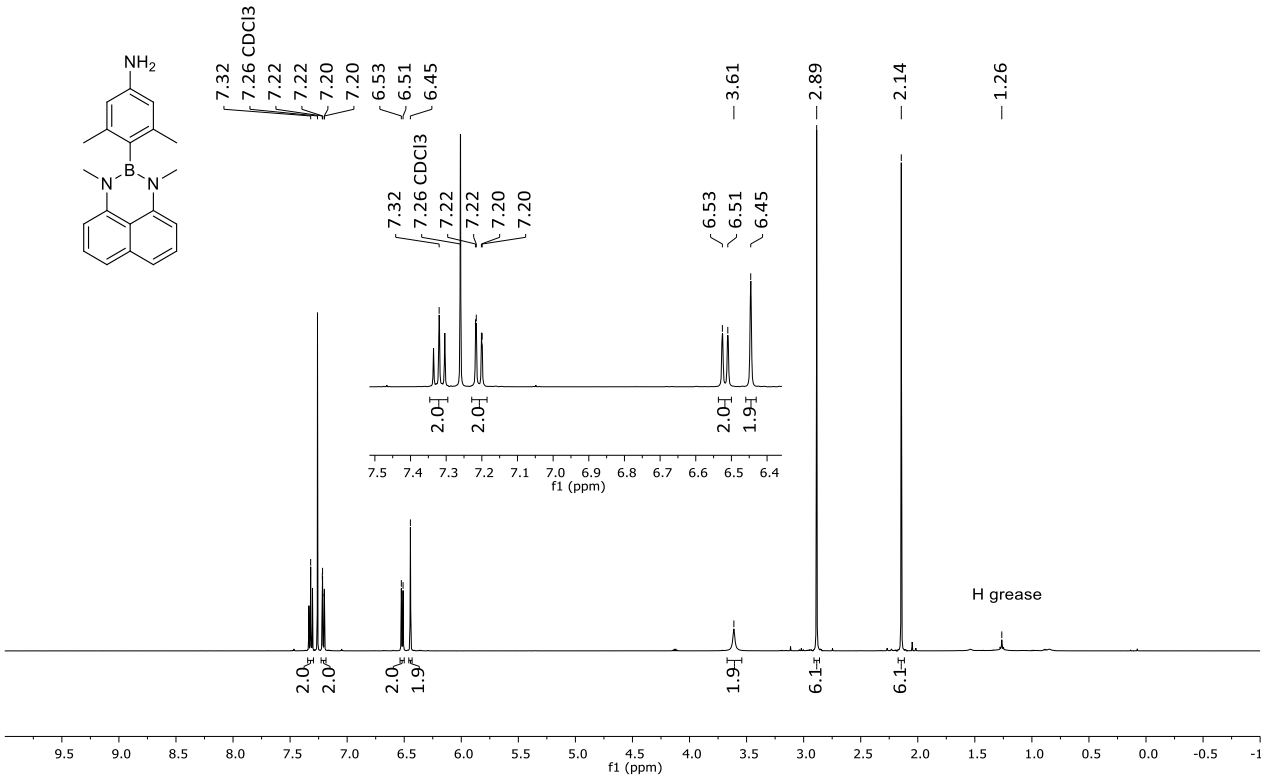

Figure S25: ^{1}H NMR spectrum of compound **6** ($CDCl_3$, 500.2 MHz).

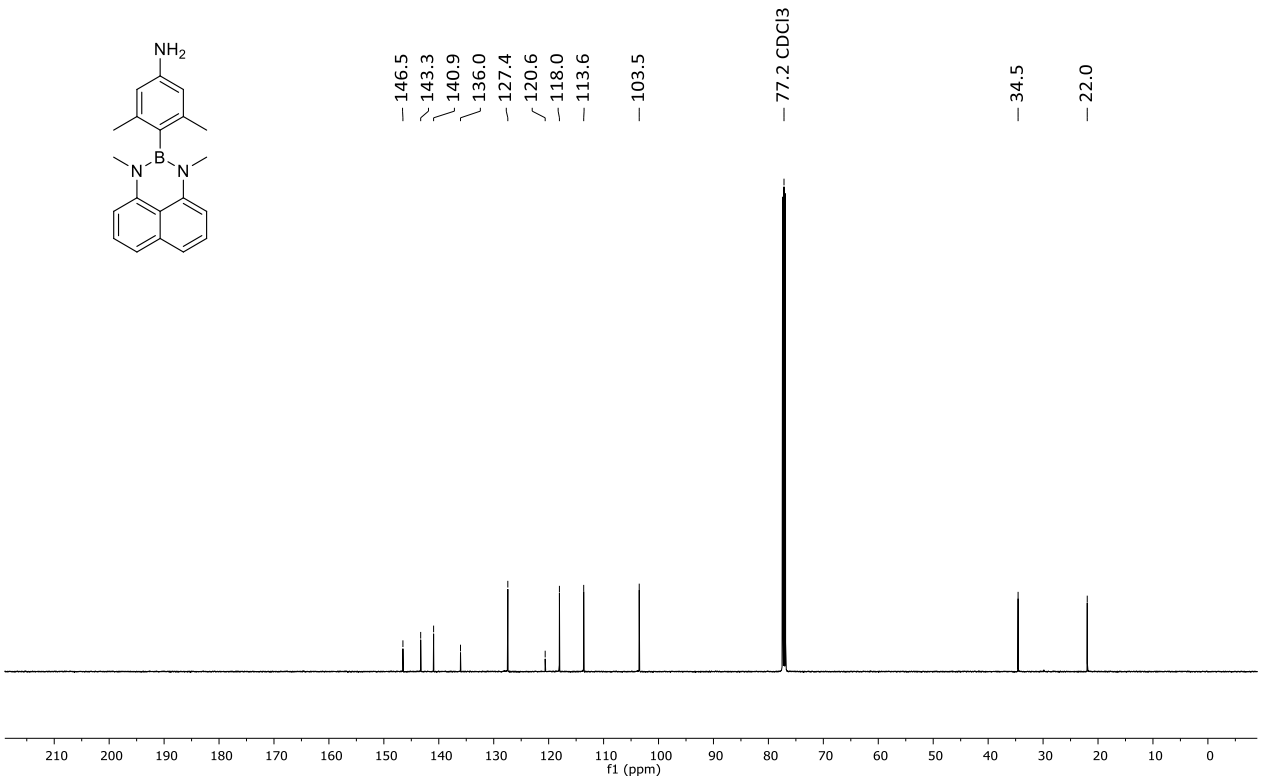

Figure S26: $^{13}C\{^{1}H\}$ NMR spectrum of compound **6** ($CDCl_3$, 125.8 MHz).

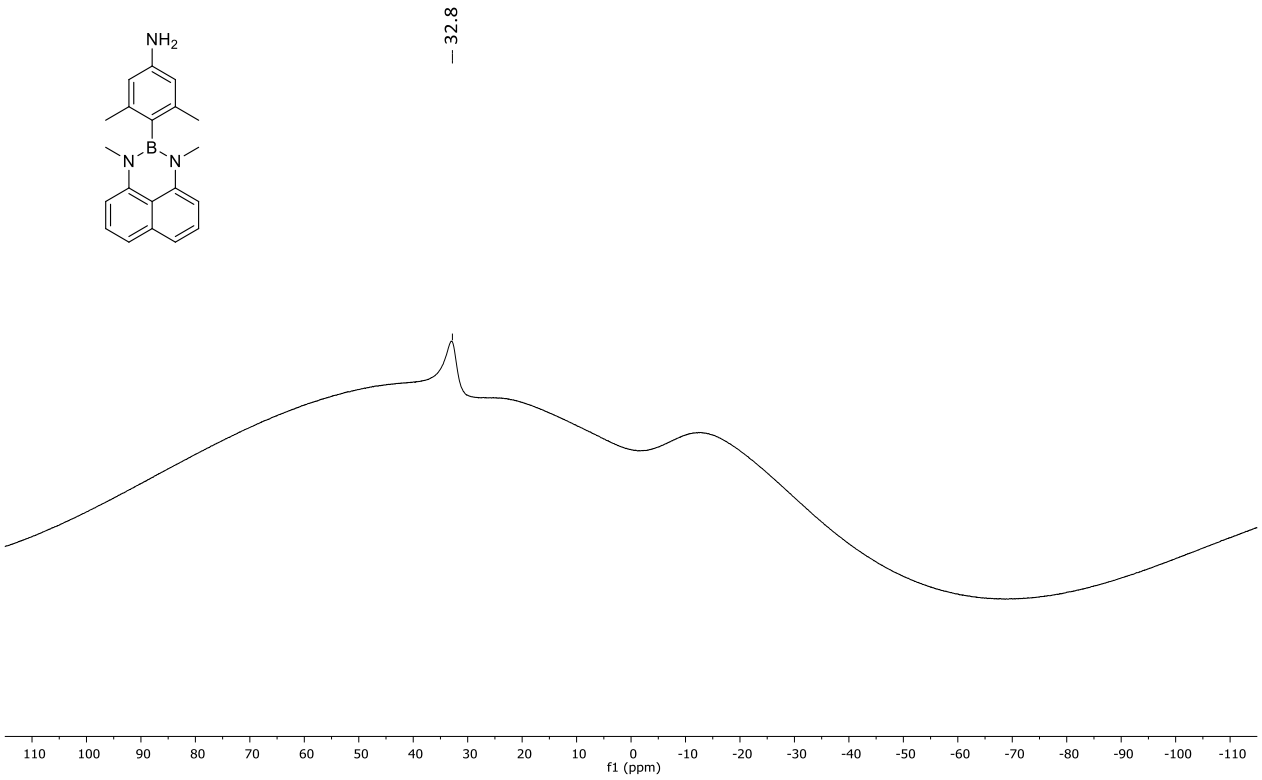

Figure S27: ^{11}B NMR spectrum of compound **6** ($CDCl_3$, 160.5 MHz).

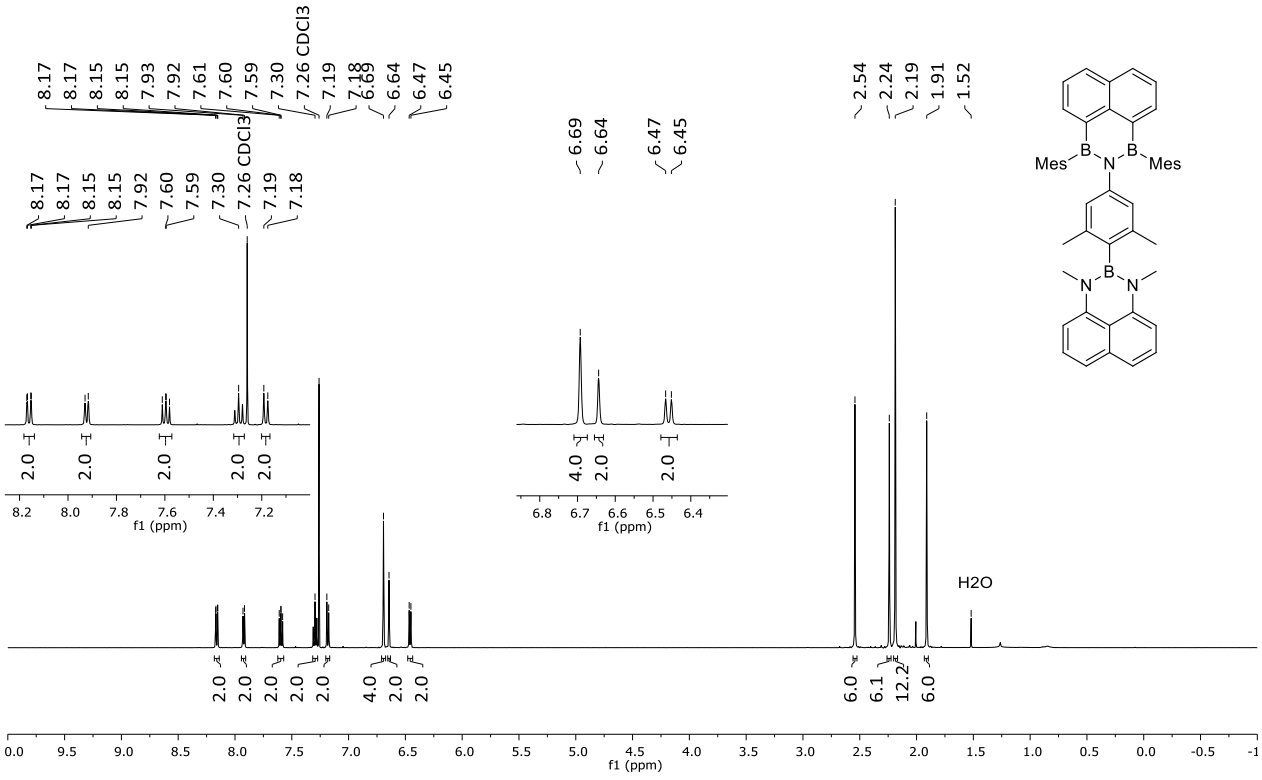

Figure S28: ^{1}H NMR spectrum of compound **4**$^{\mathbf{Me,Mes}}$ ($CDCl_3$, 500.2 MHz).

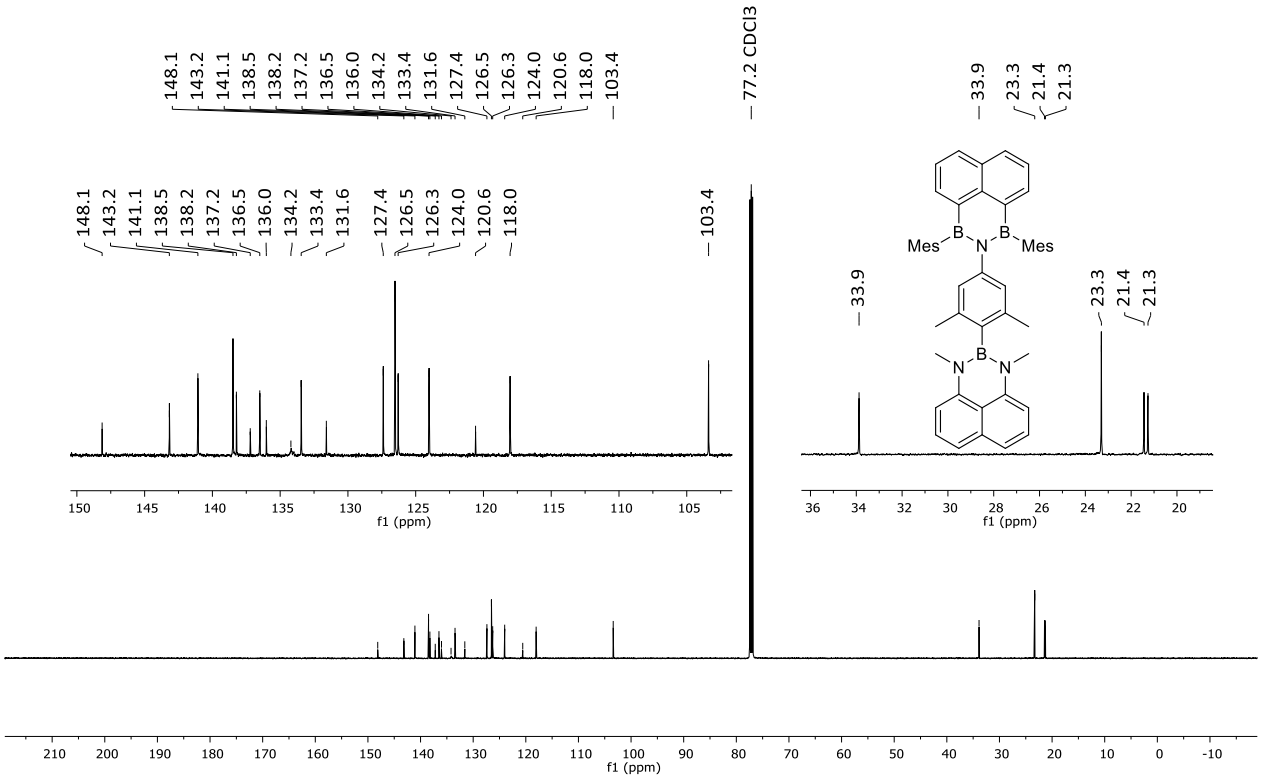

Figure S29: $^{13}C\{^{1}H\}$ NMR spectrum of compound **4**^{Me,Mes} ($CDCl_3$, 125.8 MHz).

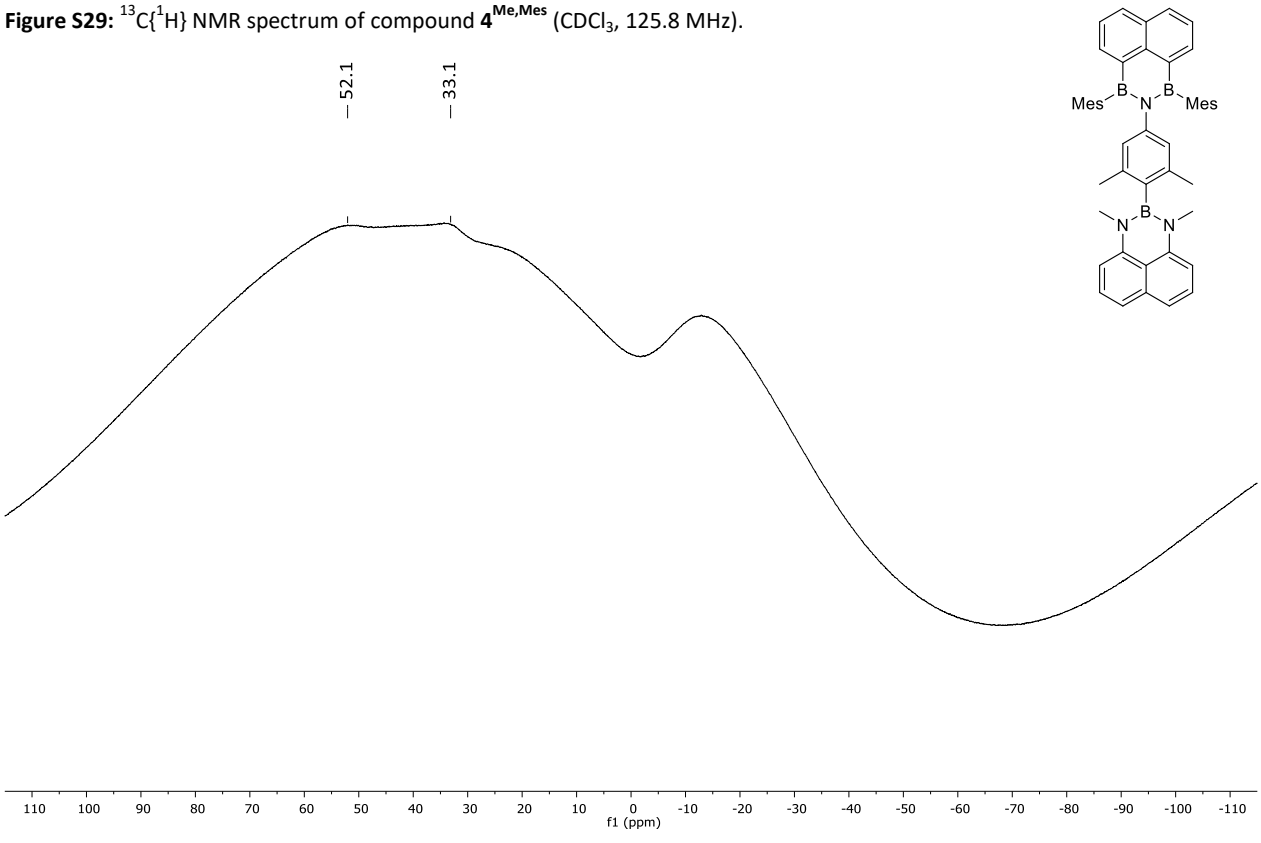

Figure S30: ^{11}B NMR spectrum of compound **4**^{Me,Mes} ($CDCl_3$, 160.5 MHz).

4. Photophysical and electrochemical data

Table S1: Photophysical and electrochemical data of compounds $\mathbf{1}^{Me}$, $\mathbf{2}^{Me}$, $\mathbf{2}^{Mes}$, $\mathbf{3}^{Me,Me}$, $\mathbf{3}^{Me,Mes}$, and $\mathbf{4}^{Me,Mes}$. Optical measurements were performed in the specified solvents. All electrochemical measurements were performed in THF.

	λ_{abs} [a] in C_6H_{12} [nm] ([eV]) {ε [M^{-1} cm^{-1}]}	λ_{onset} [b] [nm]	λ_{ex} [nm]	λ_{em} [a] [nm] ([eV])	Φ_{PL} [c] [%]	FWHM [d] [nm] ([eV])	$E_{1/2}$ [V]	E_{pa} [V]	E_{pc} [V]
$\mathbf{1}^{Me}$	333‡ (3.72) {28144} 350*‡ (3.54) 356‡ (3.48) {22145} 365*‡ (3.40)	373	333	n.o. in solution **Solid:** 471 (2.63)	**Solid:** 1	**Solid:** 114 (0.60)	––	0.08	––
$\mathbf{2}^{Me}$	304‡* (4.08) 316‡ (3.92) {12680} 330‡ (3.76) {11690} 335‡* (3.70)	346	330	**THF:** 361* (3.43) 371 (3.34) **CH_2Cl_2:** 361* (3.43) 371 (3.34)	**THF:** 7 **CH_2Cl_2:** 2	**THF:** 33 (0.30) **CH_2Cl_2:** 33 (0.30)	−2.43	––	−2.52
$\mathbf{2}^{Mes}$	323 (3.84) {57303} 335 (3.70) {51036} 342 (3.63) {58952}	351	335	**C_6H_{12}:** 399 (3.11) **C_6H_6:** 408 (3.04) **THF:** 421 (2.94) **CH_2Cl_2:** 434 (2.86) **Solid:** 404 (3.07)	**C_6H_{12}:** 28 **C_6H_6:** 34 **THF:** 28 **CH_2Cl_2:** 22 **Solid:** 15	**C_6H_{12}:** 70 (0.54) **C_6H_6:** 72 (0.52) **THF:** 79 (0.53) **CH_2Cl_2:** 83 (0.53) **Solid:** 68 (0.50)	−2.33[e]	––	−2.43
$\mathbf{3}^{Me,Me}$	318 (3.90) {13658} 332 (3.73) {14499} 357 (3.47) {5996} 365* (3.40) 477 (2.60) {139}	566	332	n.o.	--	--	−2.43	0.39	−2.55
$\mathbf{3}^{Me,Mes}$	327 (3.79) {31434} 335* (3.70) 342 (3.63) {29741} 352 (3.52) {6597} 361 (3.43) {7402}	368	327	**C_6H_{12}:** 367 (3.38) 395 (3.14) 411 (3.02) **THF:** 370 (3.35) 389 (3.19) 411 (3.02) **CH_2Cl_2:** n.o. **Solid:** 479 (2.59) 501 (2.47)	**C_6H_{12}:** 6 **THF:** 1 **Solid:** 2	**C_6H_{12}:** 64 (0.47) **THF:** 114 (0.81) **Solid:** 88 (0.42)	−2.35	0.33	−2.47
$\mathbf{4}^{Me,Mes}$	328 (3.78) {25470} 335 (3.70) {22936} 342 (3.63) {24118} 352 (3.52) {11549} 360 (3.44) {7594}	366	328	**C_6H_{12}:** 365 (3.40) 392 (3.16) **THF:** n. o. **CH_2Cl_2:** n.o. **Solid:** 471 (2.63)	**C_6H_{12}:** 3 **Solid:** 1	**C_6H_{12}:** 61 (0.46) **Solid:** 94 (0.51)	0.22, −2.35	0.32	−2.40

[a] Resolved vibrational fine structure in C_6H_{12}. *) shoulder. ‡) This measurement was performed in CH_2Cl_2, due to the poor solubility of the compound in C_6H_{12}. [b] Each onset wavelength (λ_{onset}) was determined by constructing a tangent on the point of inflection of the bathochromic slope of the most red-shifted absorption maximum. [c] Quantum yields were determined by using a calibrated integrating sphere. [d] Full-width at half-maximum. [e] The cyclic voltammogram of $\mathbf{2}^{Mes}$ shows two partly resolved reduction waves with very similar $E_{1/2}$ values.

4.1. Aggregation-induced emission (enhancement)

Table S2: Photophysical data obtained in aggregation-induced emission (enhancement) measurements in H_2O / THF mixtures.

Relative fraction H_2O / THF	**3**^{Me,Mes} Φ_{PL} [a] [%] $\lambda_{em,max}$ [b] ([nm]) {[eV]}	**4**^{Me,Mes} Φ_{PL} [a] [%] $\lambda_{em,max}$ [b] ([nm]) {[eV]}
0 / 100	1 (370) {3.35}	0
20 / 80	<1 (387) {3.20}	-
40 / 60	<1 (386) {3.21}	-
50 / 50	-	0
60 / 40	<1 (384) {3.23}	-
70 / 30	<1 (415) {2.99}	<1 (581) {2.13}
80 / 20	<1 (417) {2.97}	7 (543) {2.28}
90 / 10	2 (535) {2.32}	10 (521) {2.38}
93 / 7	5 (532) {2.33}	11 (513) {2.42}
95 / 5	6 (531) {2.33}	12 (509) {2.44}
97 / 3	5 (527) {2.35}	12 (513) {2.42}
99 / 1	4 (525) {2.36}	10 (512) {2.42}

[a] Quantum yields were determined by using a calibrated integrating sphere. [b] λ_{ex} = 327 nm.

4.2. UV/vis absorption and emission spectra

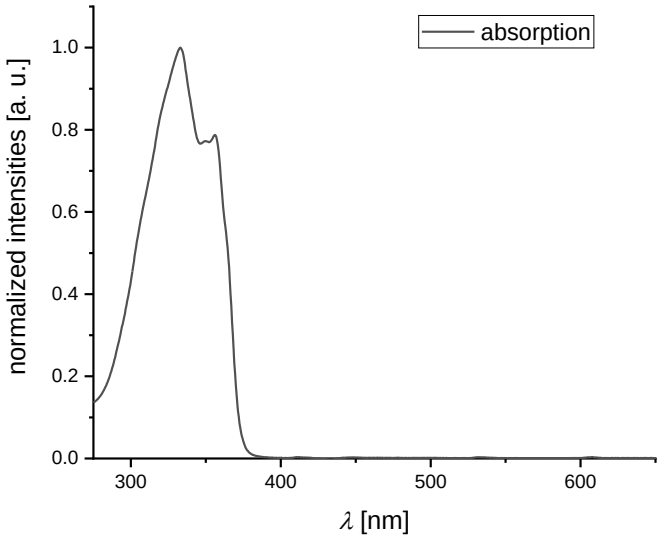

Figure S31: Normalized UV/vis absorption (CH_2Cl_2) spectrum of $\mathbf{1}^{\mathbf{Me}}$.

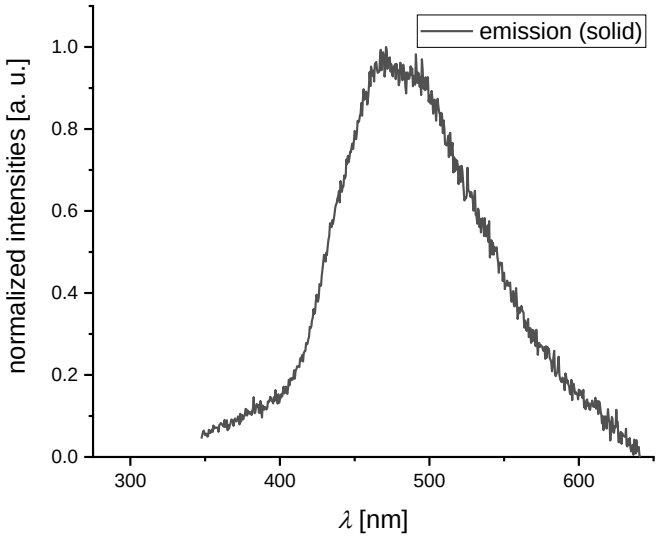

Figure S32: Solid-state emission spectrum of $\mathbf{1}^{\mathbf{Me}}$ (λ_{ex} = 333 nm).

Figure S33: Photo of a solid sample of $\mathbf{1}^{\mathbf{Me}}$ under UV irradiation (365 nm).

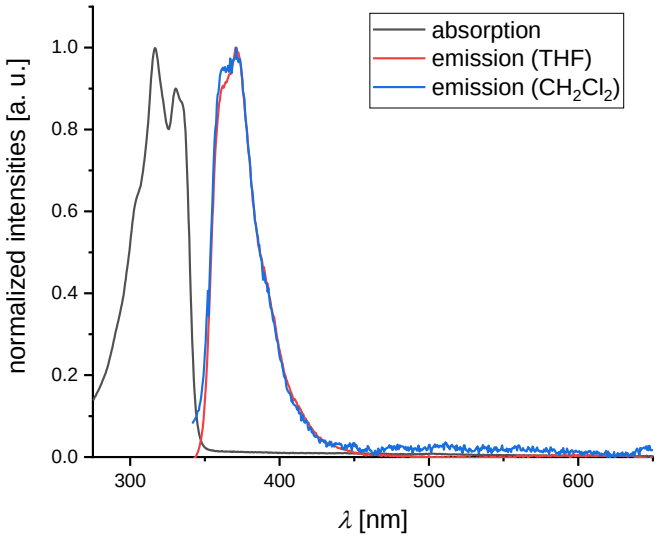

Figure S34: Normalized UV/vis absorption (CH_2Cl_2) and emission spectra of **2**^{Me} (λ_{ex} = 330 nm) in THF and CH_2Cl_2.

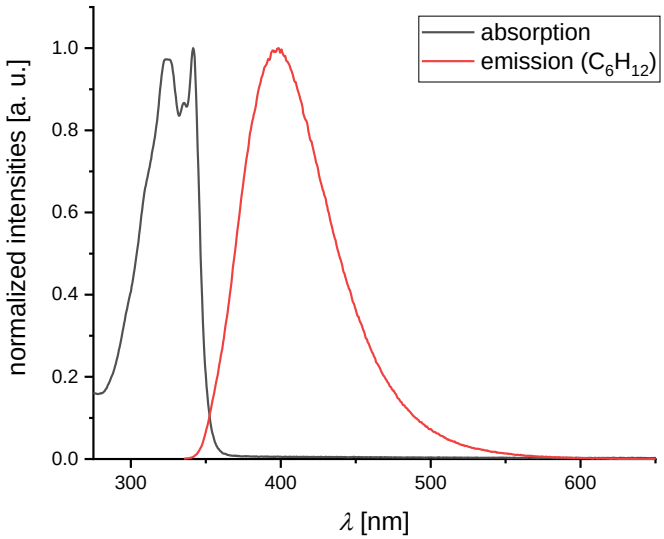

Figure S35: Normalized UV/vis absorption and emission spectra of **2**^{Mes} (C_6H_{12}, λ_{ex} = 335 nm).

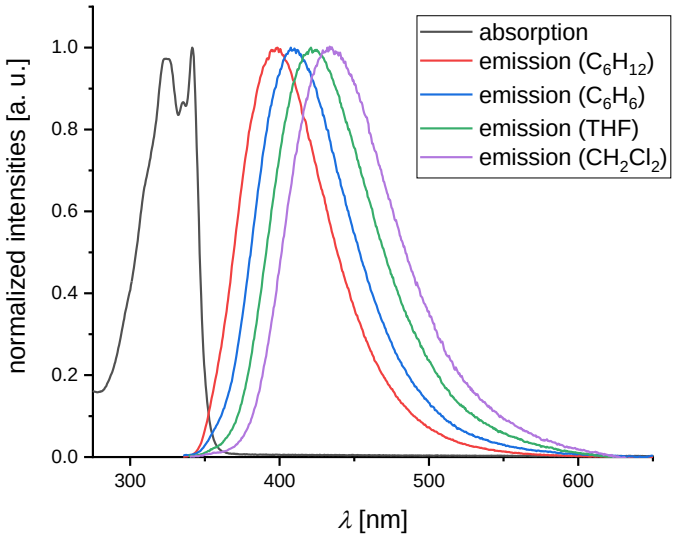

Figure S36: Normalized UV/vis absorption (C_6H_{12}) and emission spectra of **2**^{Mes} (λ_{ex} = 335 nm) in C_6H_{12}, C_6H_6, THF, and CH_2Cl_2.

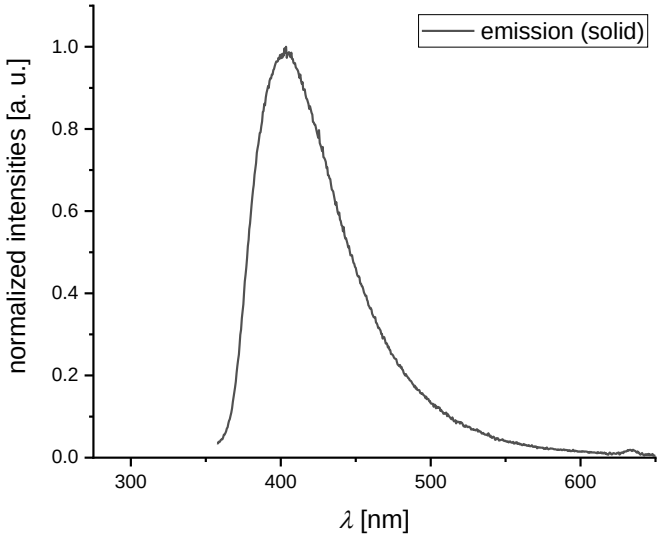

Figure S37: Solid-state emission spectrum of **2**^{Mes} (λ_{ex} = 335 nm).

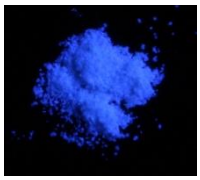

Figure S38: Photo of a solid sample of **2**^{Mes} under UV irradiation (365 nm).

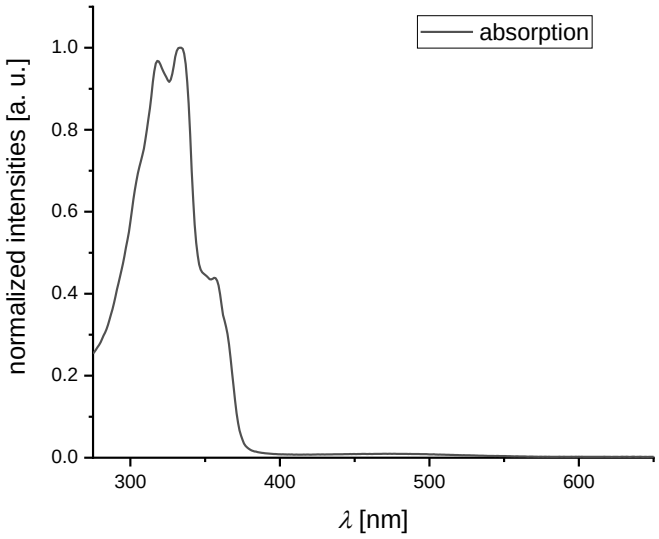

Figure S39: Normalized UV/vis absorption spectrum of $\mathbf{3}^{\mathbf{Me,Me}}$ (CH_2Cl_2).

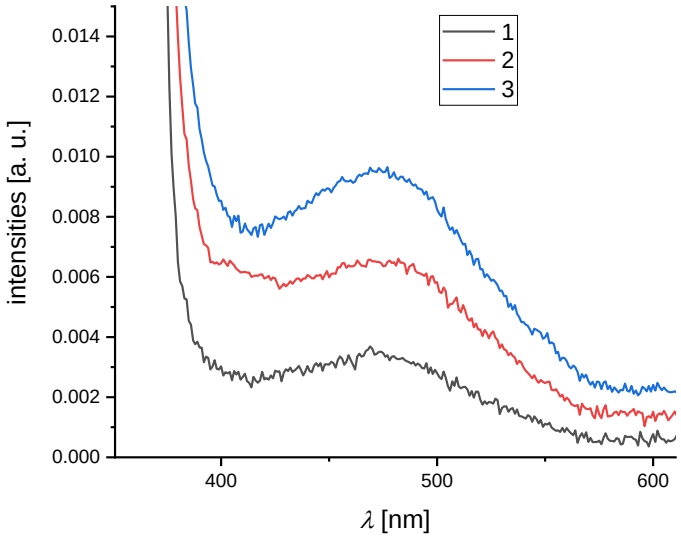

Figure S40: Section of the UV/vis absorption spectrum of $\mathbf{3}^{\mathbf{Me,Me}}$ (CH_2Cl_2) showing the weak absorption band centered at ~480 nm with increasing concentration (black → blue curve) of $\mathbf{3}^{\mathbf{Me,Me}}$.

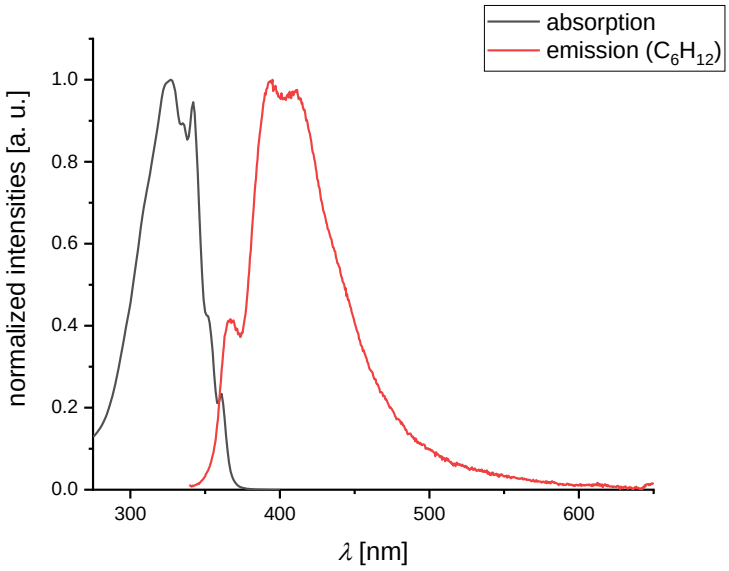

Figure S41: Normalized UV/vis absorption and emission spectra of **3**^{Me,Mes} (C_6H_{12}, λ_{ex} = 327 nm).

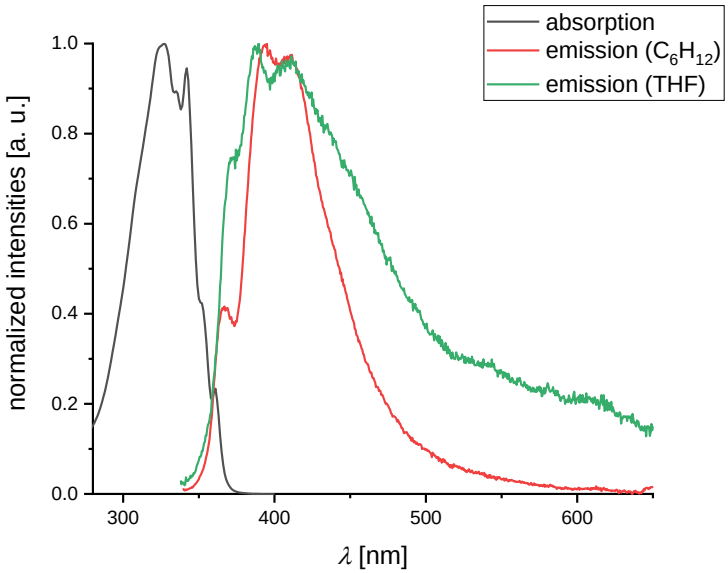

Figure S42: Normalized UV/vis absorption (C_6H_{12}) and emission spectra of **3**^{Me,Mes} (λ_{ex} = 327 nm) in C_6H_{12} and THF.

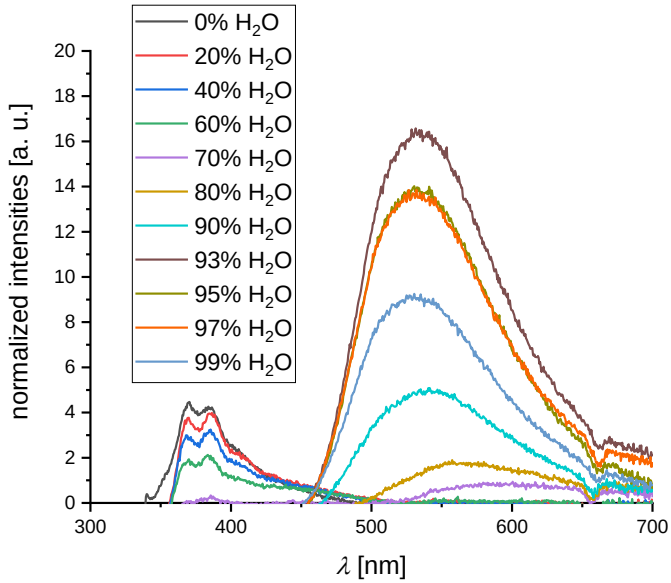

Figure S43: Emission spectra of **3**^{Me,Mes} (λ_{ex} = 327 nm) with differing H_2O fractions from 0% to 99% H_2O in THF.

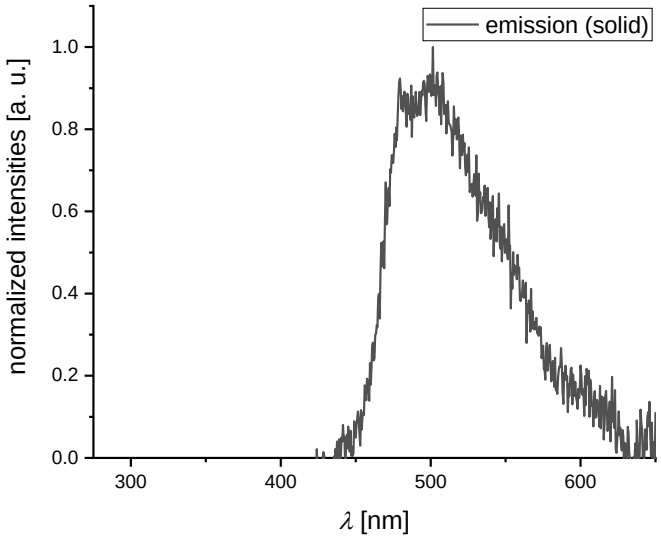

Figure S44: Solid-state emission spectrum of **3**^{Me,Mes} (λ_{ex} = 327 nm).

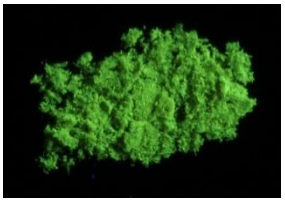

Figure S45: Photo of a solid sample of **3**^{Me,Mes} under UV irradiation (365 nm).

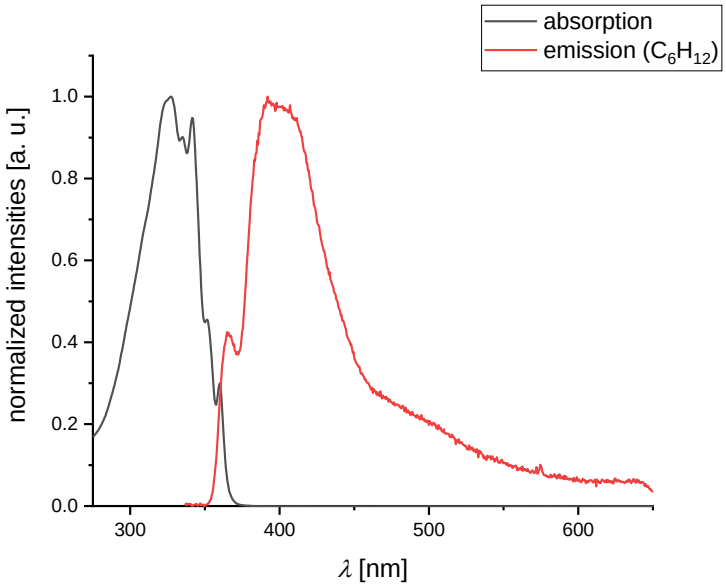

Figure S46: Normalized UV/vis absorption and emission spectra of **4**^{Me,Mes} (C_6H_{12}, λ_{ex} = 328 nm).

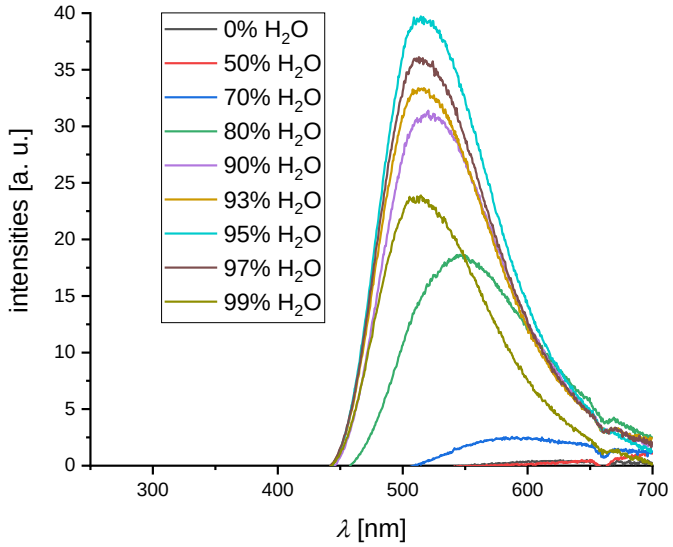

Figure S47: Emission spectra of **4**^{Me,Mes} (λ_{ex} = 327 nm) with differing H_2O fractions from 0% to 99% H_2O in THF.

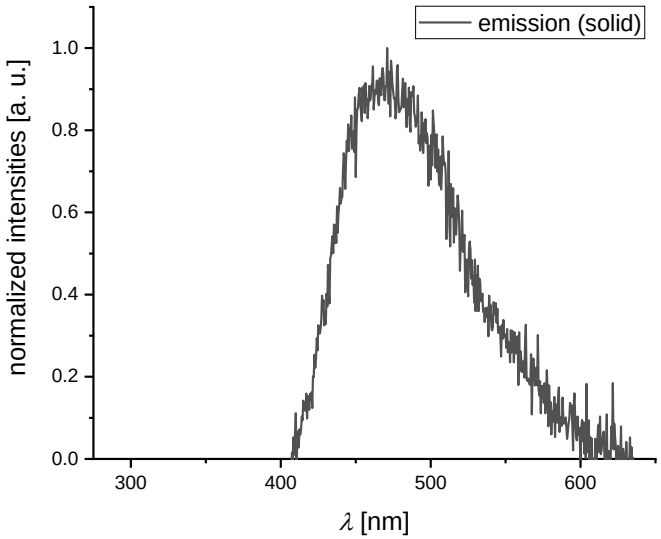

Figure S48: Solid-state emission spectrum of **4**$^{\mathbf{Me,Mes}}$ (λ_{ex} = 328 nm).

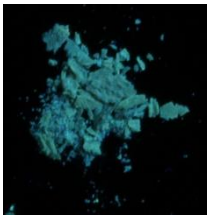

Figure S49: Photo of a solid sample of **4**$^{\mathbf{Me,Mes}}$ under UV irradiation (365 nm).

4.3. Plots of cyclic voltammograms

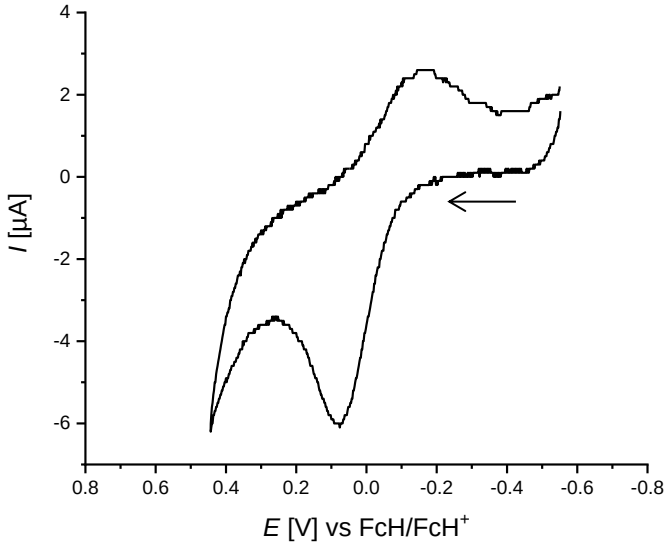

Figure S50: Cyclic voltammogram of $\mathbf{1}^{Me}$ in THF (referenced against the FcH/FcH^+ redox couple, room temperature, supporting electrolyte [*n*-Bu_4N][PF_6] (0.1 M), scan rate 200 mV s^{-1}, switching potentials: 0.44, −0.55 V).

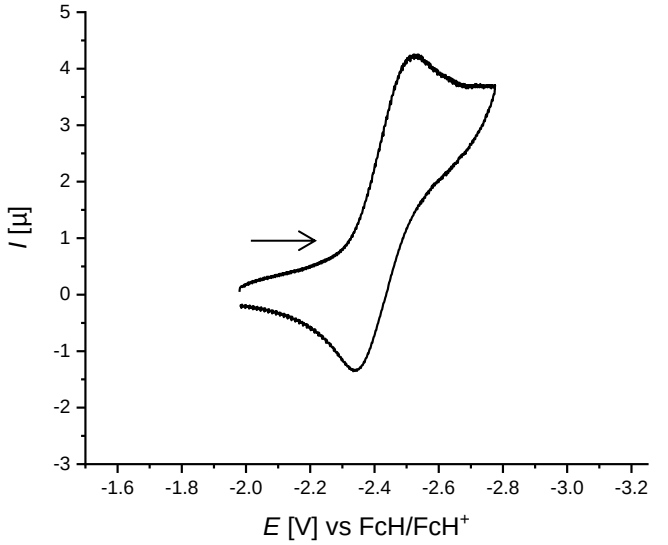

Figure S51: Cyclic voltammogram of $\mathbf{2}^{Me}$ in THF (referenced against the FcH/FcH^+ redox couple, room temperature, supporting electrolyte [*n*-Bu_4N][PF_6] (0.1 M), scan rate 200 mV s^{-1}, switching potentials: −1.98, −2.78 V).

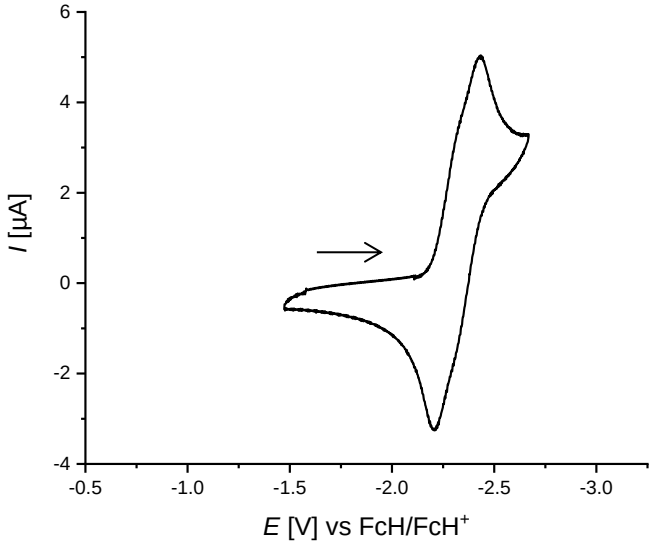

Figure S52: Cyclic voltammogram of $\mathbf{2}^{\mathbf{Mes}}$ in THF (referenced against the FcH/FcH^+ redox couple, room temperature, supporting electrolyte [*n*-Bu_4N][PF_6] (0.1 M), scan rate 200 mV s^{-1}, switching potentials: −1.47, −2.67 V).

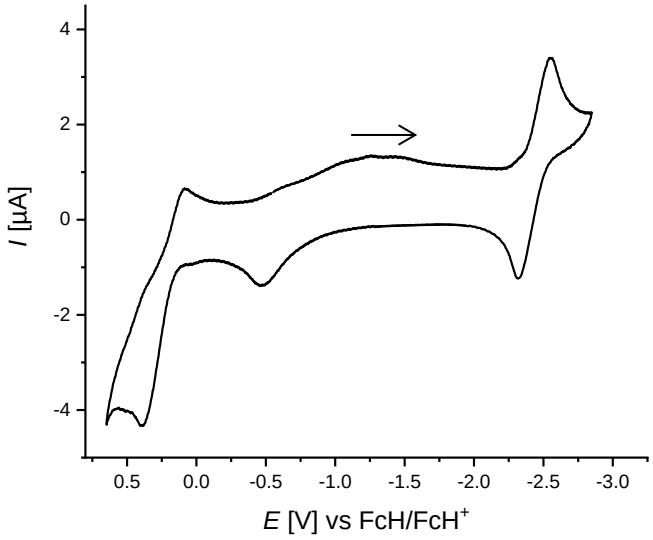

Figure S53: Cyclic voltammogram of $\mathbf{3}^{\mathbf{Me,Me}}$ in THF (referenced against the FcH/FcH^+ redox couple, room temperature, supporting electrolyte [*n*-Bu_4N][PF_6] (0.1 M), scan rate 200 mV s^{-1}, switching potentials: 0.65, −2.84 V).

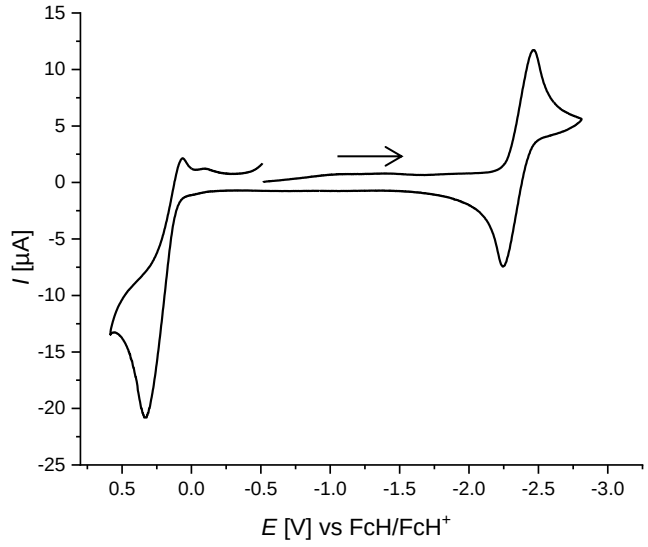

Figure S54: Cyclic voltammogram of **3**^{Me,Mes} in THF (referenced against the FcH/FcH$^+$ redox couple, room temperature, supporting electrolyte [*n*-Bu$_4$N][PF$_6$] (0.1 M), scan rate 200 mV s^{-1}, switching potentials: 0.58, −2.81 V).

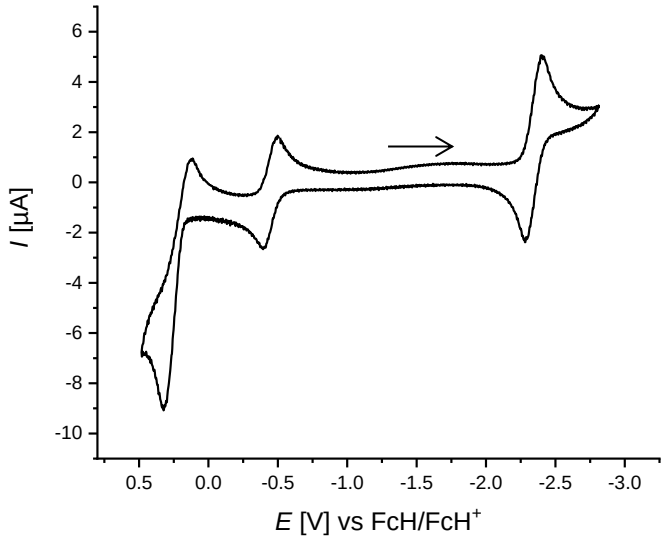

Figure S55: Cyclic voltammogram of **4**^{Me,Mes} in THF (referenced against the FcH/FcH$^+$ redox couple, room temperature, supporting electrolyte [*n*-Bu$_4$N][PF$_6$] (0.1 M), scan rate 200 mV s^{-1}, switching potentials: 0.48, −2.81 V). The wave in the middle corresponds to the Fc*H/Fc*H$^+$ redox couple.

5. X-ray crystal structure analyses

Data for all structures were collected on a STOE IPDS II two-circle diffractometer with a Genix Microfocus tube with mirror optics using MoK_α radiation (λ = 0.71073 Å) and were scaled using the frame-scaling procedure in the *X-AREA*[S11] program system. The structures were solved by direct methods using the program *SHELXS* and refined against F^2 with full-matrix least-squares techniques using the program *SHELXL-97*.[S12]

In **2**$^{\mathbf{H}}$, the coordinates of B-bonded H atoms were freely refined. The crystal was twinned. The fractional contribution of the minor occupied domain was refined to 0.2517(19).

In **2**$^{\mathbf{Me}}$·CH_2Cl_2, the C atom of co-crystallized CH_2Cl_2 is disordered over two equally occupied positions. The displacement ellipsoids of the disordered atoms were approximated to the shape of a sphere.

In **2**$^{\mathbf{Mes}}$·C_6H_{12}, the molecule lies on the intersection of three two-fold rotation axes. It therefore belongs to the symmetry point group D_2. Four atoms of the co-crystallized cyclohexane molecule are disordered over two equally occupied positions. The displacement ellipsoids of the disordered atoms were approximated to the shape of a sphere.

In **5**, the H atoms attached to the N atoms were freely refined.

In **3**$^{\mathbf{Me,Me}}$·THF, the molecule resides on a mirror plane, which results in the mutual disorder of the B and N atoms with equal occupation. The disordered B and N atoms were refined with the same coordinates and displacement parameters.

1$^{\mathbf{Me}}$·CH_2Cl_2, **2**$^{\mathbf{Me}}$·CH_2Cl_2, and **3**$^{\mathbf{Me,Me}}$·THF are isostructural. All of them crystallize in the orthorhombic crystal system with the space group *Pnma* (No. 62). The molecules form dimers linked *via* π-stacking interactions between parallel flat aromatic systems. The interplanar distance systematically increases with the increasing number of nitrogen atoms from 3.50 Å ({B_4N_2}, **2**$^{\mathbf{Me}}$) to 3.54 Å({B_3N_3}, **3**$^{\mathbf{Me,Me}}$) and 3.59 Å ({B_2N_4}, **1**$^{\mathbf{Me}}$). The cavities of ~250–260 Å^3 between the molecules in the crystal packing are filled with slightly disordered solvent molecules (CH_2Cl_2 or THF).

In **3**$^{\mathbf{Me,Mes}}$·C_6H_{14}, the C–C bond lengths in the co-crystallized *n*-hexane molecule were restrained to 1.500(8) Å.

In **6**, the H atoms attached to the N atoms were located in an electron density-difference map. Their displacement ellipsoids were refined with N–H bond lengths restrained to 0.91(1) Å.

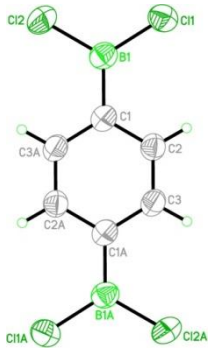

Figure S56: Solid-state structure of **B**. Displacement ellipsoids are drawn at the 50% probability level. Symmetry operator for generating equivalent atoms: −x + 1, −y + 1, −z. Selected bond lengths [Å]: B(1)−Cl(1) = 1.742(3), B(1)−Cl(2) = 1.753(3), B(1)−C(1) = 1.548(3).

Table S3: Crystal data and structure refinement for **B**.

Empirical formula	$C_6H_4B_2Cl_4$	
Formula weight	239.51	
Temperature	173(2) K	
Wavelength	0.71073 Å	
Crystal system	Monoclinic	
Space group	$P2_1/n$	
Unit cell dimensions	a = 3.9587(3) Å	α = 90°.
	b = 14.8849(9) Å	β = 101.651(5)°.
	c = 8.3966(6) Å	γ = 90°.
Volume	484.57(6) Å^3	
Z	2	
Density (calculated)	1.642 mg/m^3	
Absorption coefficient	1.154 mm^{-1}	
F(000)	236	
Crystal color, shape	colorless block	
Crystal size	0.290 × 0.290 × 0.280 mm^3	
Theta range for data collection	3.692 to 25.613°.	
Index ranges	−4<=h<=4, −18<=k<=18, −10<=l<=10	
Reflections collected	7798	
Independent reflections	906 [R(int) = 0.0658]	
Completeness to theta = 25.000°	99.4%	
Absorption correction	Semi-empirical from equivalents	
Max. and min. transmission	1.000 and 0.752	
Refinement method	Full-matrix least-squares on F^2	
Data / restraints / parameters	906 / 0 / 55	
Goodness-of-fit on F^2	1.094	
Final R indices [I>2sigma(I)]	R1 = 0.0409, wR2 = 0.1108	
R indices (all data)	R1 = 0.0421, wR2 = 0.1129	
Largest diff. peak and hole	0.316 and −0.425 e.Å^{-3}	

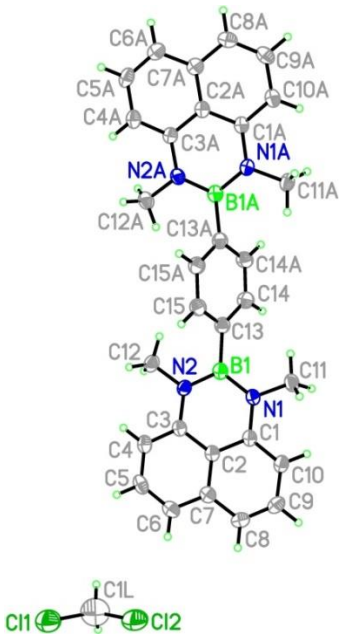

Figure S57: Solid-state structure of $\mathbf{1}^{\mathbf{Me}}\cdot CH_2Cl_2$. Displacement ellipsoids are drawn at the 50% probability level. Symmetry operator for generating equivalent atoms: x, –y + 0.5, z. Selected bond lengths [Å], bond angles [°], and torsion angles [°]: B(1)–N(1) = 1.430(3), B(1)–N(2) = 1.432(3), B(1)–C(13) = 1.580(3), N(1)–C(1) = 1.404(2), N(1)–C(11) = 1.463(2), N(2)–C(3) = 1.400(2), N(2)–C(12) = 1.467(2); N(1)–B(1)–N(2) = 118.21(18), B(1)–N(1)–C(1) = 121.53(16), B(1)–N(1)–C(11) = 122.12(17), B(1)–N(2)–C(3) = 121.80(16), B(1)–N(2)–C(12) = 121.73(16), N(1)–B(1)–C(13) = 122.30(17), N(2)–B(1)–C(13) = 119.42(17), C(1)–N(1)–C(11) = 116.27(15), C(3)–N(2)–C(12) = 116.45(16); N(1)–B(1)–C(13)–C(14) = 68.1(3), N(2)–B(1)–C(13)–C(14) = –115.1(2).

π-Stacking can be observed with a distance of 3.606 Å between the planes (Figure S58 and Figure S59). B(1) is located almost directly above C(7) of a neighboring molecule with a distance of 3.697 Å.

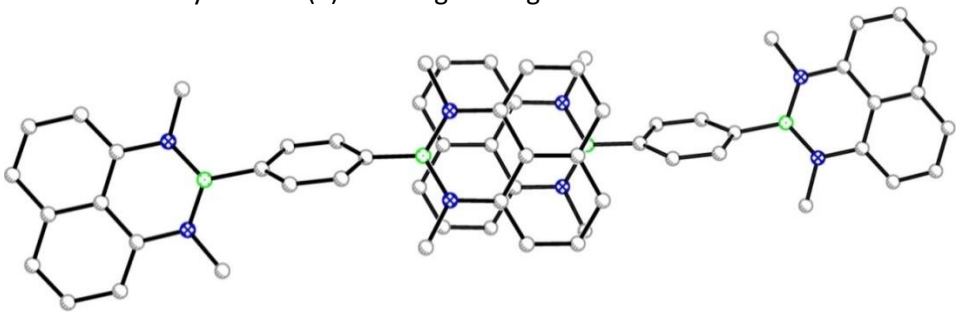

Figure S58: Top view of the stacking mode in the crystal lattice of $\mathbf{1}^{\mathbf{Me}}\cdot CH_2Cl_2$. Co-crystallized CH_2Cl_2 and H atoms are omitted for clarity.

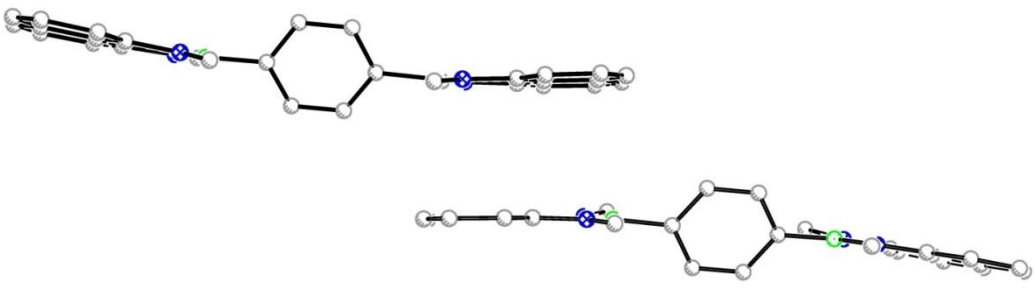

Figure S59: Side view of the stacking mode in the crystal lattice of $\mathbf{1}^{\mathbf{Me}}\cdot CH_2Cl_2$. Co-crystallized CH_2Cl_2 and H atoms are omitted for clarity.

Table S4: Crystal data and structure refinement for $\mathbf{1}^{\mathbf{Me}}\cdot CH_2Cl_2$.

Empirical formula	$C_{30}H_{28}B_2N_4\cdot CH_2Cl_2$	
Formula weight	551.11	
Temperature	173(2) K	
Wavelength	0.71073 Å	
Crystal system	Orthorhombic	
Space group	*P n m a*	
Unit cell dimensions	a = 12.6194(8) Å	α = 90°.
	b = 22.0063(13) Å	β = 90°.
	c = 9.7913(8) Å	γ = 90°.
Volume	2719.1(3) Å^3	
Z	4	
Density (calculated)	1.346 mg/m^3	
Absorption coefficient	0.268 mm^{-1}	
F(000)	1152	
Crystal color, shape	colorless block	
Crystal size	0.290 × 0.280 × 0.280 mm^3	
Theta range for data collection	3.359 to 25.623°.	
Index ranges	−14<=h<=15, −26<=k<=22, −11<=l<=11	
Reflections collected	8768	
Independent reflections	2590 [R(int) = 0.0241]	
Completeness to theta = 25.000°	98.9%	
Absorption correction	Semi-empirical from equivalents	
Max. and min. transmission	1.000 and 0.613	
Refinement method	Full-matrix least-squares on F^2	
Data / restraints / parameters	2590 / 0 / 183	
Goodness-of-fit on F^2	1.087	
Final R indices [I>2sigma(I)]	R1 = 0.0475, wR2 = 0.1167	
R indices (all data)	R1 = 0.0632, wR2 = 0.1292	
Largest diff. peak and hole	0.624 and −0.673 e.Å^{-3}	

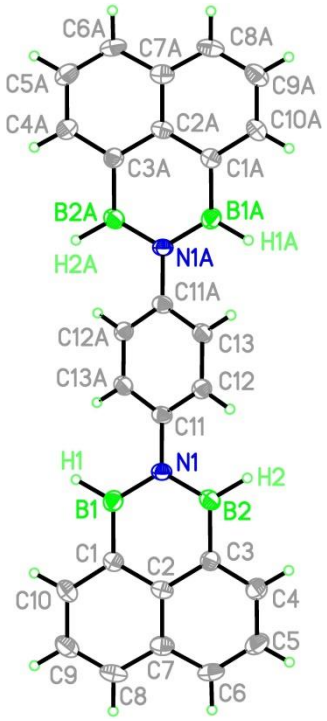

Figure S60: Solid-state structure of $\mathbf{2}^{\mathbf{H}}$. Displacement ellipsoids are drawn at the 50% probability level. Symmetry operator to generate equivalent atoms: −x, −y, −z + 1. Selected bond lengths [Å], bond angles [°], and torsion angles [°]: B(1)–N(1) = 1.437(4), B(2)–N(1) = 1.430(4), B(1)–C(1) = 1.540(4), B(2)–C(3) = 1.547(4), B(1)–H(1) = 1.09(3), B(2)–H(2) = 1.11(3), N(1)–C(11) = 1.445(3); B(1)–N(1)–B(2) = 118.8(2), B(1)–N(1)–C(11) = 121.1(2), B(2)–N(1)–C(11) = 120.1(2), N(1)–B(1)–H(1) = 119.0(14), N(1)–B(2)–H(2) = 120.0(13), C(1)–B(1)–H(1) = 120.3(14), C(3)–B(2)–H(2) = 119.5(13); B(1)–N(1)–C(11)–C(12) = 142.9(3), B(2)–N(1)–C(11)–C(12) = −36.4(4).

Table S5: Crystal data and structure refinement for **2^{H}.**

Empirical formula	$C_{26}H_{20}B_4N_2$	
Formula weight	403.68	
Temperature	173(2) K	
Wavelength	0.71073 Å	
Crystal system	Monoclinic	
Space group	$P2_1/c$	
Unit cell dimensions	a = 3.9326(2) Å	α = 90°.
	b = 19.1064(14) Å	β = 90.046(5)°.
	c = 13.7709(9) Å	γ = 90°.
Volume	1034.72(11) Å^3	
Z	2	
Density (calculated)	1.296 mg/m^3	
Absorption coefficient	0.073 mm^{-1}	
F(000)	420	
Crystal color, shape	colorless needle	
Crystal size	0.170 × 0.030 × 0.030 mm^3	
Theta range for data collection	3.525 to 25.687°.	
Index ranges	−4<=h<=4, −23<=k<=23, −16<=l<=16	
Reflections collected	9038	
Independent reflections	1938 [R(int) = 0.0515]	
Completeness to theta = 25.000°	99.6%	
Absorption correction	Semi-empirical from equivalents	
Max. and min. transmission	1.000 and 0.551	
Refinement method	Full-matrix least-squares on F^2	
Data / restraints / parameters	1938 / 0 / 154	
Goodness-of-fit on F^2	1.237	
Final R indices [I>2sigma(I)]	R1 = 0.0573, wR2 = 0.1145	
R indices (all data)	R1 = 0.0759, wR2 = 0.1264	
Largest diff. peak and hole	0.181 and −0.161 e.Å^{-3}	

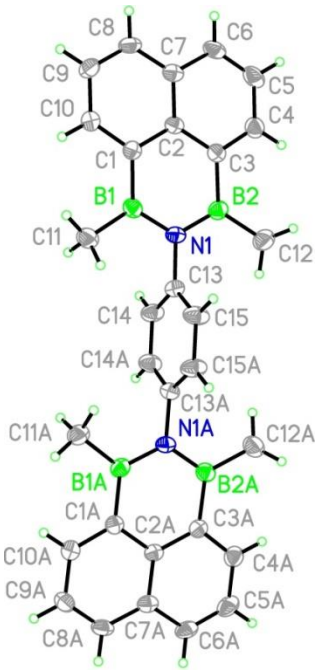

Figure S61: Solid-state structure of $\mathbf{2}^{\mathbf{Me}}\cdot CH_2Cl_2$. Co-crystallized CH_2Cl_2 is omitted for clarity. Displacement ellipsoids are drawn at the 50% probability level. Symmetry operator to generate equivalent atoms: x, –y + 1.5, z. Selected bond lengths [Å], bond angles [°], and torsion angles [°]: B(1)–N(1) = 1.450(5), B(2)–N(1) = 1.438(5), B(1)–C(1) = 1.555(5), B(1)–C(11) = 1.570(5), B(2)–C(3) = 1.562(5), B(2)–C(12) = 1.577(5), N(1)–C(13) = 1.451(4); B(1)–N(1)–B(2) = 122.6(3), B(1)–N(1)–C(13) = 117.9(3), B(2)–N(1)–C(13) = 119.5(3), N(1)–B(1)–C(1) = 117.4(3), N(1)–B(1)–C(11) = 119.9(3), N(1)–B(2)–C(3) = 117.6(3), N(1)–B(2)–C(12) = 121.0(3), C(1)–B(1)–C(11) = 122.7(3), C(3)–B(2)–C(12) = 121.3(3); B(1)–N(1)–C(13)–C(15) = 94.3(4), B(2)–N(1)–C(13)–C(15) = –83.7(4).

Table S6: Crystal data and structure refinement for $\mathbf{2}^{\mathbf{Me}}\cdot CH_2Cl_2$.

Empirical formula	$C_{30}H_{28}B_4N_2\cdot CH_2Cl_2$	
Formula weight	544.71	
Temperature	173(2) K	
Wavelength	0.71073 Å	
Crystal system	Orthorhombic	
Space group	*P n m a*	
Unit cell dimensions	a = 12.5056(7) Å	α = 90°.
	b = 23.4207(11) Å	β = 90°.
	c = 9.6710(4) Å	γ = 90°.
Volume	2832.5(2) Å^3	
Z	4	
Density (calculated)	1.277 mg/m^3	
Absorption coefficient	0.254 mm^{-1}	
F(000)	1136	
Crystal color, shape	colorless plate	
Crystal size	0.250 × 0.230 × 0.060 mm^3	
Theta range for data collection	3.181 to 25.707°.	
Index ranges	−15<=h<=15, -28<=k<=28, -11<=l<=11	
Reflections collected	26484	
Independent reflections	2734 [R(int) = 0.0515]	
Completeness to theta = 25.000°	99.8%	
Absorption correction	Semi-empirical from equivalents	
Max. and min. transmission	1.000 and 0.642	
Refinement method	Full-matrix least-squares on F^2	
Data / restraints / parameters	2734 / 6 / 186	
Goodness-of-fit on F^2	1.037	
Final R indices [I>2sigma(I)]	R1 = 0.0892, wR2 = 0.2302	
R indices (all data)	R1 = 0.1151, wR2 = 0.2572	
Largest diff. peak and hole	0.791 and −1.089 e.Å^{-3}	

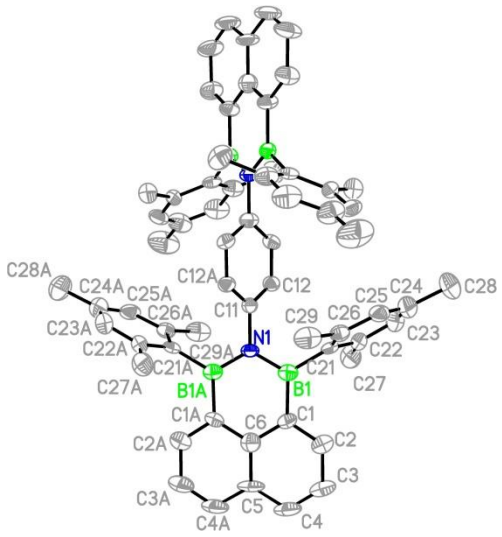

Figure S62: Solid-state structure of $\mathbf{2}^{\mathbf{Mes}}\cdot C_6H_{12}$ is shown here. Co-crystallized C_6H_{12} and H atoms are omitted for clarity. Displacement ellipsoids are drawn at the 50% probability level. Symmetry operators to generate equivalent atoms: a) x, –y + 1.5, –z + 1.5; b) –x, y, –z + 1.5; c) –x + 0.5, –y + 1, z. Selected bond lengths [Å], bond angles [°], and torsion angles [°]: B(1)–N(1) = 1.445(8), B(1)–C(1) = 1.557(8), B(1)–C(21) = 1.596(9); B(1)–N(1)–B(1A) = 121.8(7), B(1)–N(1)–C(11) = 119.1(3), N(1)–B(1)–C(1) = 117.9(6), N(1)–B(1)–C(21) = 120.9(5), C(1)–B(1)–C(21) = 121.2(6); B(1)–N(1)–C(11)–C(12) = 67.3(4), B(1A)–N(1)–C(11)–C(12) = –112.7(4).

Table S7: Crystal data and structure refinement for $\mathbf{2}^{\mathbf{Mes}}\cdot C_6H_{12}$.

Empirical formula	$C_{62}H_{60}B_4N_2\cdot C_6H_{12}$	
Formula weight	1044.67	
Temperature	173(2) K	
Wavelength	0.71073 Å	
Crystal system	Orthorhombic	
Space group	*C c c* a	
Unit cell dimensions	a = 25.514(4) Å	α = 90°.
	b = 16.100(3) Å	β = 90°.
	c = 15.3944(18) Å	γ = 90°.
Volume	6323.6(17) Å^3	
Z	4	
Density (calculated)	1.097 mg/m^3	
Absorption coefficient	0.061 mm^{-1}	
F(000)	2248	
Crystal size	0.080 × 0.070 × 0.070 mm^3	
Theta range for data collection	3.272 to 25.703°.	
Index ranges	−31<=h<=29, −19<=k<=19, −18<=l<=18	
Reflections collected	21435	
Independent reflections	3001 [R(int) = 0.2351]	
Completeness to theta = 25.000°	99.7%	
Absorption correction	Semi-empirical from equivalents	
Max. and min. transmission	1.000 and 0.923	
Refinement method	Full-matrix least-squares on F^2	
Data / restraints / parameters	3001 / 24 / 202	
Goodness-of-fit on F^2	1.275	
Final R indices [I>2sigma(I)]	R1 = 0.1577, wR2 = 0.2281	
R indices (all data)	R1 = 0.2577, wR2 = 0.2613	
Largest diff. peak and hole	0.175 and −0.208 e.Å^{-3}	

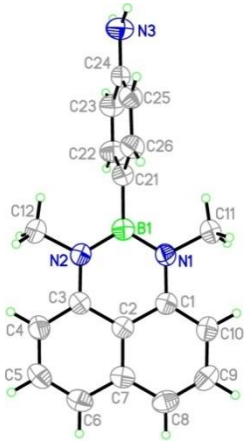

Figure S63: Solid-state structure of **5**. Displacement ellipsoids are drawn at the 50% probability level. Selected bond lengths [Å], bond angles [°], and torsion angles [°]: B(1)–N(1) = 1.427(3), B(1)–N(2) = 1.428(3), B(1)–C(21) = 1.573(3), N(1)–C(1) = 1.402(2), N(2)–C(3) = 1.404(2); N(1)–B(1)–N(2) = 118.31(17), B(1)–N(1)–C(1) = 121.83(16), B(1)–N(1)–C(11) = 121.59(16), B(1)–N(2)–C(3) = 121.84(16), B(1)–N(2)–C(12) = 121.61(17), N(1)–B(1)–C(21) = 121.51(18), N(2)–B(1)–C(21) = 120.18(17), C(1)–N(1)–C(11) = 116.55(15), C(3)–N(2)–C(12) = 116.46(16); N(1)–B(1)–C(21)–C(22) = 104.1(2), N(2)–B(1)–C(21)–C(22) = –75.4(3).

Table S8: Crystal data and structure refinement for **5**.

Empirical formula	$C_{18}H_{18}BN_3$	
Formula weight	287.16	
Temperature	173(2) K	
Wavelength	0.71073 Å	
Crystal system	Orthorhombic	
Space group	$P\,2_1\,2_1\,2_1$	
Unit cell dimensions	a = 7.2323(3) Å	α = 90°.
	b = 10.5998(4) Å	β = 90°.
	c = 20.4068(9) Å	γ = 90°.
Volume	1564.40(11) Å^3	
Z	4	
Density (calculated)	1.219 mg/m^3	
Absorption coefficient	0.073 mm^{-1}	
F(000)	608	
Crystal size	0.260 × 0.240 × 0.230 mm^3	
Theta range for data collection	2.771 to 27.601°.	
Index ranges	−9<=h<=9, −13<=k<=13, −26<=l<=26	
Reflections collected	16518	
Independent reflections	3587 [R(int) = 0.0284]	
Completeness to theta = 25.000°	99.3%	
Absorption correction	Semi-empirical from equivalents	
Max. and min. transmission	1.000 and 0.526	
Refinement method	Full-matrix least-squares on F^2	
Data / restraints / parameters	3587 / 0 / 210	
Goodness-of-fit on F^2	1.136	
Final R indices [I>2sigma(I)]	R1 = 0.0391, wR2 = 0.1031	
R indices (all data)	R1 = 0.0409, wR2 = 0.1045	
Absolute structure parameter	0.2(10)	
Extinction coefficient	0.064(10)	
Largest diff. peak and hole	0.183 and −0.153 e.Å^{-3}	

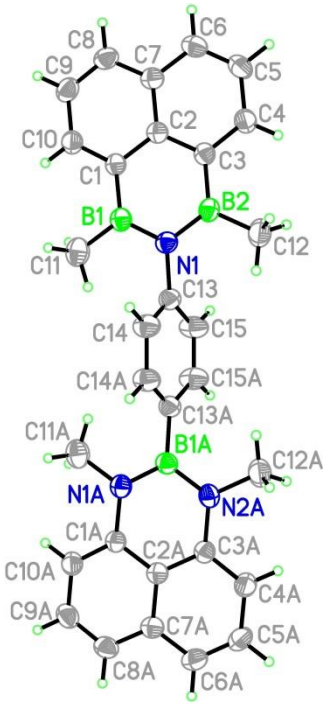

Figure S64: Solid-state structure of $\mathbf{3}^{\mathbf{Me,Me}}$·THF. Co-crystallized THF is omitted for clarity. The molecule is located on a crystallographic mirror plane, which can be attributed to the structural similarity of the NBN- and BNB-phenalenyl moieties in the crystal structure. This renders both halves of the molecules indistinguishable. Displacement ellipsoids are drawn at the 50% probability level. Symmetry operator for generating equivalent atoms: x, –y + 1.5, z. Selected bond lengths [Å], bond angles [°], and torsion angles [°]: B(1)/B(1A)–N(1)/N(1A) = 1.437(2), B(1)/N(1A)–C(1)/C(1A) = 1.472(2), B(2)/B(1A)–N(1)/N(2A) = 1.445(2), B(2)/N(2A)–C(3)/C(3A) = 1.471(2), N(1)/B(1A)–C(13)/C(13A) = 1.502(2); B(1)/N(1A)–N(1)/B(1A)–B(2)/N(2A) = 118.91(14), B(1)/N(1A)–N(1)/B(1A)–C(13)/C(13A) = 119.81(14), B(2)/N(2A)–N(1)/B(1A)–C(13)/C(13A) = 121.27(14), N(1)/B(1A)–B(1)/N(1A)–C(1)/C(1A) = 120.89(14), N(1)/B(1A)–B(1)/N(1A)–C(11)/C(11A) = 120.33(16), N(1)/B(1A)–B(2)/N(2A)–C(3)/C(3A) = 120.45(14), N(1)/B(1A)–B(2)/N(2A)–C(12)/C(12A) = 120.55(15), C(1)/C(1A)–B(1)/N(1A)–C(11)/C(11A) = 118.78(15), C(3)/C(3A)–B(2)/N(2A)–C(12)/C(12A) = 118.97(15); N(1A)–B(1A)–C(13A)–C(15A) = 101.5(2), N(2A)–B(1A)–C(13A)–C(15A) = –79.5(2).

Table S9: Crystal data and structure refinement for $\mathbf{3}^{\mathbf{Me,Me}}$·THF.

Empirical formula	$C_{30}H_{28}B_3N_3$·THF	
Formula weight	535.09	
Temperature	173(2) K	
Wavelength	0.71073 Å	
Crystal system	Orthorhombic	
Space group	*P n m a*	
Unit cell dimensions	a = 11.5196(3) Å	α = 90°.
	b = 23.1323(6) Å	β = 90°.
	c = 10.7965(4) Å	γ = 90°.
Volume	2877.00(15) Å^3	
Z	4	
Density (calculated)	1.235 mg/m^3	
Absorption coefficient	0.073 mm^{-1}	
F(000)	1136	
Crystal color, shape	yellow block	
Crystal size	0.280 × 0.220 × 0.220 mm^3	
Theta range for data collection	2.586 to 27.750°.	
Index ranges	−15<=h<=14, −29<=k<=30, −14<=l<=14	
Reflections collected	37275	
Independent reflections	3397 [R(int) = 0.0418]	
Completeness to theta = 25.000°	99.6%	
Absorption correction	Semi-empirical from equivalents	
Max. and min. transmission	1.000 and 0.563	
Refinement method	Full-matrix least-squares on F^2	
Data / restraints / parameters	3397 / 0 / 196	
Goodness-of-fit on F^2	1.112	
Final R indices [I>2sigma(I)]	R1 = 0.0636, wR2 = 0.1579	
R indices (all data)	R1 = 0.0747, wR2 = 0.1684	
Extinction coefficient	0.0090(19)	
Largest diff. peak and hole	0.606 and −0.356 e.Å^{-3}	

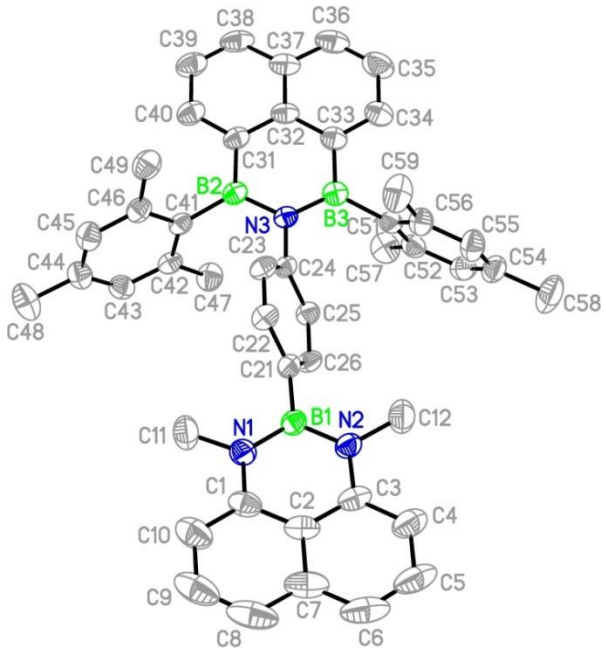

Figure S65: Solid-state structure of $\mathbf{3}^{\mathbf{Me,Mes}}\cdot C_6H_{14}$. Co-crystallized *n*-hexane and H atoms are omitted for clarity. Displacement ellipsoids are drawn at the 50% probability level. Selected bond lengths [Å], bond angles [°], and torsion angles [°]: B(1)–N(1) = 1.428(4), B(1)–N(2) = 1.420(4), B(2)–N(3) = 1.457(4), B(3)–N(3) = 1.441(4), B(1)–C(21) = 1.571(4), B(2)–C(31) = 1.558(4), B(2)–C(41) = 1.572(4), B(3)–C(33) = 1.554(4), B(3)–C(51) = 1.583(4), N(1)–C(1) = 1.405(4), N(2)–C(3) = 1.400(4), N(3)–C(24) = 1.446(3); B(2)–N(3)–B(3) = 121.5(2), N(1)–B(1)–N(2) = 118.2(3), B(1)–N(1)–C(1) = 121.6(2), B(1)–N(1)–C(11) = 122.1(2), B(1)–N(2)–C(3) = 122.0(2), B(1)–N(2)–C(12) = 121.9(2), N(1)–B(1)–C(21) = 120.6(2), N(2)–B(1)–C(21) = 121.1(2), N(3)–B(2)–C(31) = 117.8(2), N(3)–B(2)–C(41) = 121.9(2), N(3)–B(3)–C(33) = 118.5(2), N(3)–B(3)–C(51) = 122.5(3), C(31)–B(2)–C(41) = 120.1(2), C(33)–B(3)–C(51) = 118.9(2), C(1)–N(1)–C(11) = 116.3(2), C(3)–N(2)–C(12) = 116.0(2); B(2)–N(3)–C(24)–C(23) = –63.0(3), B(3)–N(3)–C(24)–C(23) = 117.6(3), N(1)–B(1)–C(21)–C(22) = 63.5(4), N(2)–B(1)–C(21)–C(22) = –113.6(3).

Table S10: Crystal data and structure refinement for $\mathbf{3}^{\mathbf{Me,Mes}}\cdot C_6H_{14}$.

Empirical formula	$C_{46}H_{44}B_3N_3\cdot C_6H_{14}$	
Formula weight	757.44	
Temperature	173(2) K	
Wavelength	0.71073 Å	
Crystal system	Monoclinic	
Space group	$P2_1/c$	
Unit cell dimensions	a = 16.9643(12) Å	α = 90°.
	b = 22.2064(11) Å	β = 96.641(6)°.
	c = 11.8863(8) Å	γ = 90°.
Volume	4447.7(5) Å^3	
Z	4	
Density (calculated)	1.131 mg/m^3	
Absorption coefficient	0.064 mm^{-1}	
F(000)	1624	
Crystal size	0.210 × 0.140 × 0.120 mm^3	
Theta range for data collection	3.248 to 25.749°.	
Index ranges	−20<=h<=20, −26<=k<=24, −14<=l<=14	
Reflections collected	35029	
Independent reflections	8344 [R(int) = 0.0891]	
Completeness to theta = 25.000°	99.8%	
Absorption correction	Semi-empirical from equivalents	
Max. and min. transmission	1.000 and 0.279	
Refinement method	Full-matrix least-squares on F^2	
Data / restraints / parameters	8344 / 5 / 531	
Goodness-of-fit on F^2	1.023	
Final R indices [I>2sigma(I)]	R1 = 0.0686, wR2 = 0.1552	
R indices (all data)	R1 = 0.1378, wR2 = 0.1938	
Largest diff. peak and hole	0.377 and −0.360 e.Å^{-3}	

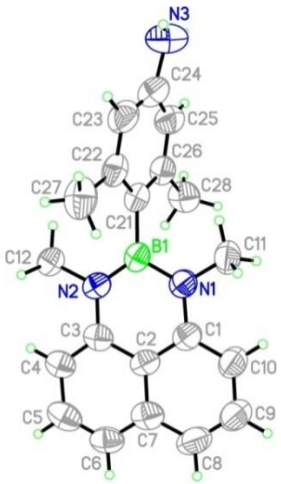

Figure S66: Solid-state structure of **6**. In the crystal lattice of **6**, there are three almost identical molecules in the asymmetric unit. Only one molecule is shown here. Displacement ellipsoids are drawn at the 50% probability level. Selected bond lengths [Å], bond angles [°], and torsion angles [°]: B(1)–N(1) = 1.452(4), B(1)–N(2) = 1.411(5), B(1)–C(21) = 1.576(5), N(1)–C(1) = 1.395(4), N(2)–C(3) = 1.393(4); N(1)–B(1)–N(2) = 118.3(3), B(1)–N(1)–C(1) = 120.8(3), B(1)–N(1)–C(11) = 122.3(3), B(1)–N(2)–C(3) = 122.8(3), B(1)–N(2)–C(12) = 121.1(3), N(1)–B(1)–C(21) = 117.7(3), N(2)–B(1)–C(21) = 124.0(3), C(1)–N(1)–C(11) = 117.0(3), C(3)–N(2)–C(12) = 116.2(3); N(1)–B(1)–C(21)–C(22) = –96.3(4), N(2)–B(1)–C(21)–C(22) = 84.0(4).

Table S11: Crystal data and structure refinement for **6.**

Empirical formula	$C_{20}H_{22}BN_3$	
Formula weight	315.21	
Temperature	173(2) K	
Wavelength	0.71073 Å	
Crystal system	Monoclinic	
Space group	$P2_1/c$	
Unit cell dimensions	a = 12.1715(4) Å	α = 90°.
	b = 18.8940(4) Å	β = 92.011(2)°.
	c = 22.6103(7) Å	γ = 90°.
Volume	5196.5(3) $Å^3$	
Z	12	
Density (calculated)	1.209 mg/m^3	
Absorption coefficient	0.071 mm^{-1}	
F(000)	2016	
Crystal color, shape	light brown block	
Crystal size	0.270 × 0.250 × 0.220 mm^3	
Theta range for data collection	2.156 to 25.027°.	
Index ranges	−14<=h<=14, −22<=k<=22, −26<=l<=26	
Reflections collected	44476	
Independent reflections	9168 [R(int) = 0.0406]	
Completeness to theta = 25.000°	99.8%	
Absorption correction	Semi-empirical from equivalents	
Max. and min. transmission	1.000 and 0.859	
Refinement method	Full-matrix least-squares on F^2	
Data / restraints / parameters	9168 / 6 / 685	
Goodness-of-fit on F^2	1.137	
Final R indices [I>2sigma(I)]	R1 = 0.0732, wR2 = 0.1777	
R indices (all data)	R1 = 0.0945, wR2 = 0.1970	
Largest diff. peak and hole	0.453 and −0.255 $e.Å^{-3}$	

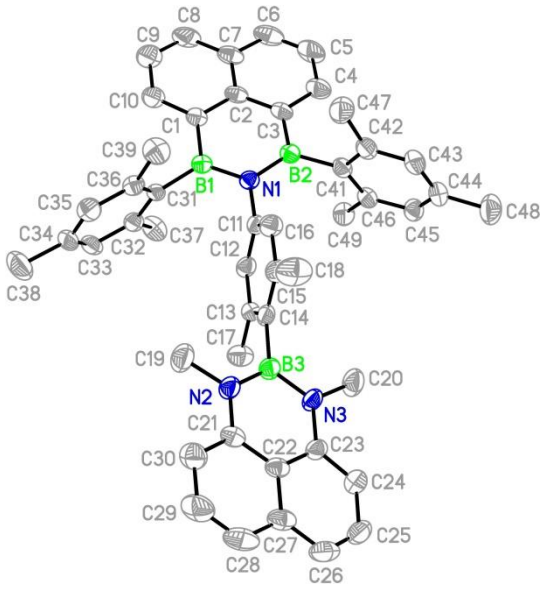

Figure S67: Solid-state structure of **4**^{Me,Mes}. H atoms are omitted for clarity. Displacement ellipsoids are drawn at the 50% probability level. Selected bond lengths [Å], bond angles [°], and torsion angles [°]: B(1)–N(1) = 1.444(5), B(2)–N(1) = 1.440(5), B(3)–N(2) = 1.416(5), B(3)–N(3) = 1.426(5), B(1)–C(1) = 1.566(5), B(1)–C(31) = 1.575(5), B(2)–C(3) = 1.555(5), B(2)–C(41) = 1.573(5), B(3)–C(14) = 1.582(5), N(1)–C(11) = 1.451(4), N(2)–C(21) = 1.404(4), N(3)–C(23) = 1.403(4); B(1)–N(1)–B(2) = 121.7(3), N(2)–B(3)–N(3) = 118.2(3), B(1)–N(1)–C(11) = 118.6(3), B(2)–N(1)–C(11) = 119.7(3), B(3)–N(2)–C(19) = 121.1(3), B(3)–N(2)–C(21) = 121.7(3), B(3)–N(3)–C(20) = 121.4(3), B(3)–N(3)–C(23) = 121.7(3), N(2)–B(3)–C(14) = 120.8(3), N(3)–B(3)–C(14) = 120.9(3), N(1)–B(1)–C(1) = 117.8(3), N(1)–B(1)–C(31) = 122.4(3), N(1)–B(2)–C(3) = 118.2(3), N(1)–B(2)–C(41) = 122.0(3), C(1)–B(1)–C(31) = 119.8(3), C(3)–B(2)–C(41) = 119.8(3), C(19)–N(2)–C(21) = 117.2(3), C(20)–N(3)–C(23) = 116.9(3); B(1)–N(1)–C(11)–C(12) = 72.9(4), B(2)–N(1)–C(11)–C(12) = –108.2(4), N(2)–B(3)–C(14)–C(13) = –97.5(4), N(3)–B(3)–C(14)–C(13) = 82.0(5).

Table S12: Crystal data and structure refinement for **4**^{Me,Mes}.

Empirical formula	$C_{48}H_{48}B_3N_3$	
Formula weight	699.32	
Temperature	173(2) K	
Wavelength	0.71073 Å	
Crystal system	Triclinic	
Space group	*P*-1	
Unit cell dimensions	a = 11.4766(6) Å	α = 102.326(4)°.
	b = 13.7242(7) Å	β = 106.309(4)°.
	c = 15.0142(8) Å	γ = 107.834(4)°.
Volume	2041.3(2) Å^3	
Z	2	
Density (calculated)	1.138 mg/m^3	
Absorption coefficient	0.065 mm^{-1}	
F(000)	744	
Crystal color, shape	colorless block	
Crystal size	0.230 × 0.190 × 0.160 mm^3	
Theta range for data collection	3.255 to 25.795°.	
Index ranges	−13<=h<=14, −16<=k<=16, −18<=l<=18	
Reflections collected	31694	
Independent reflections	7667 [R(int) = 0.0612]	
Completeness to theta = 25.000°	99.7%	
Absorption correction	Semi-empirical from equivalents	
Max. and min. transmission	1.000 and 0.732	
Refinement method	Full-matrix least-squares on F^2	
Data / restraints / parameters	7667 / 0 / 497	
Goodness-of-fit on F^2	1.307	
Final R indices [I>2sigma(I)]	R1 = 0.0932, wR2 = 0.1553	
R indices (all data)	R1 = 0.1367, wR2 = 0.1773	
Largest diff. peak and hole	0.263 and −0.212 e.Å^{-3}	

6. High-resolution mass spectrometry

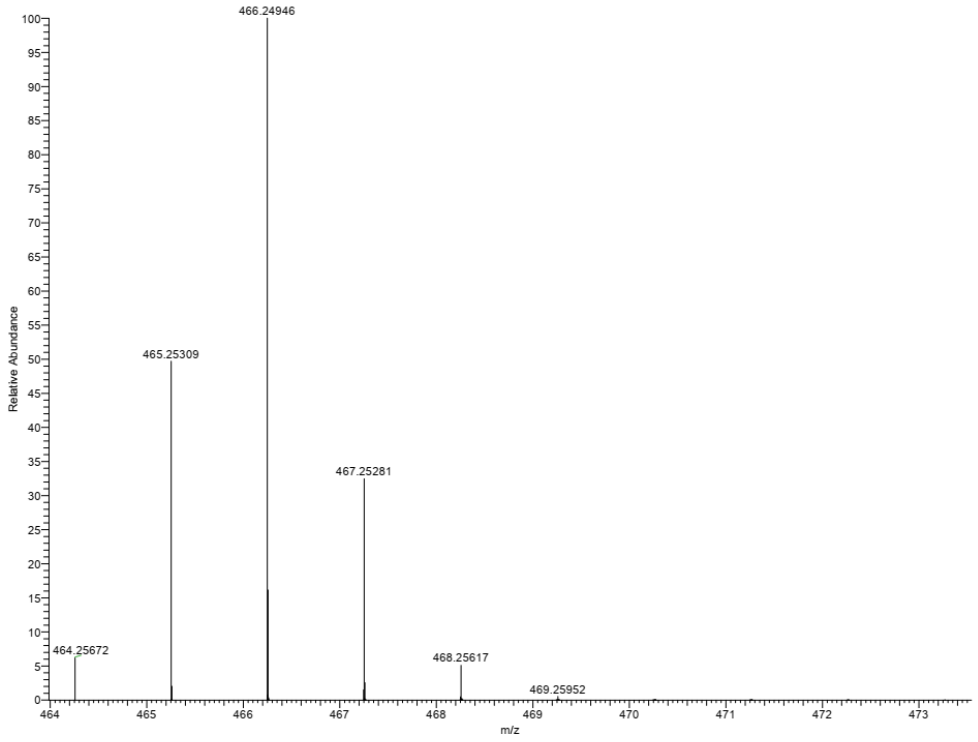

Figure S68: Simulated high-resolution mass spectrum of $[\mathbf{1}]^{\bullet+}$. Note that for technical reasons the *m*/*z* scale differs between the respective experimental and simulated mass spectra.

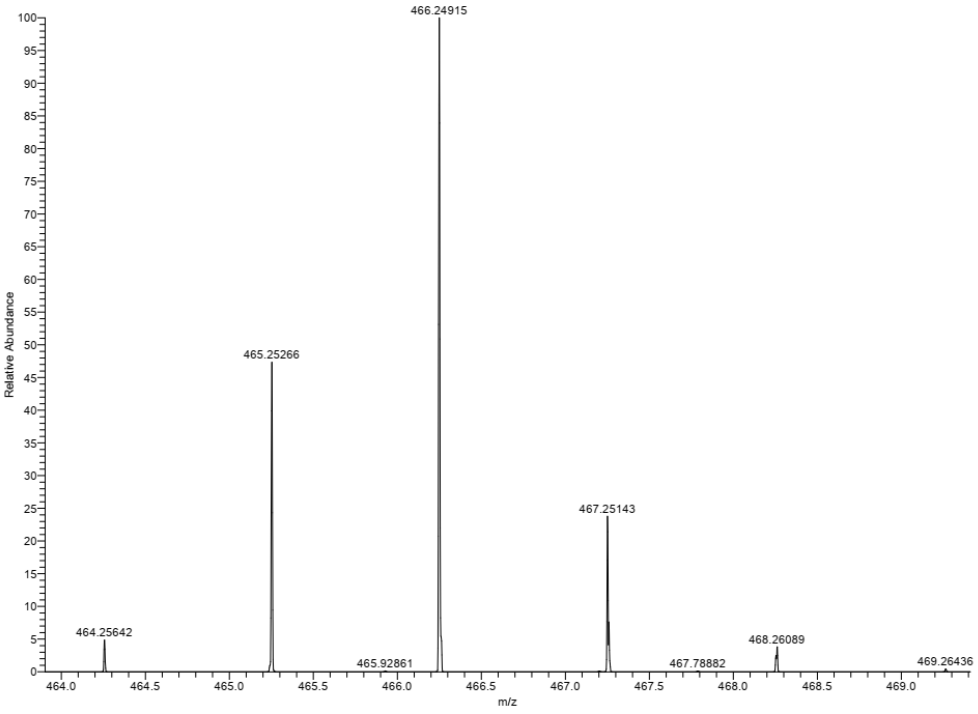

Figure S69: High-resolution mass spectrum of $[\mathbf{1}]^{\bullet+}$ measured in positive mode using a *Thermo Fisher Scientific* MALDI LTQ Orbitrap XL spectrometer and α-cyano-4-hydroxycinnamic acid as the matrix. Note that for technical reasons the *m*/*z* scale differs between the respective experimental and simulated mass spectra.

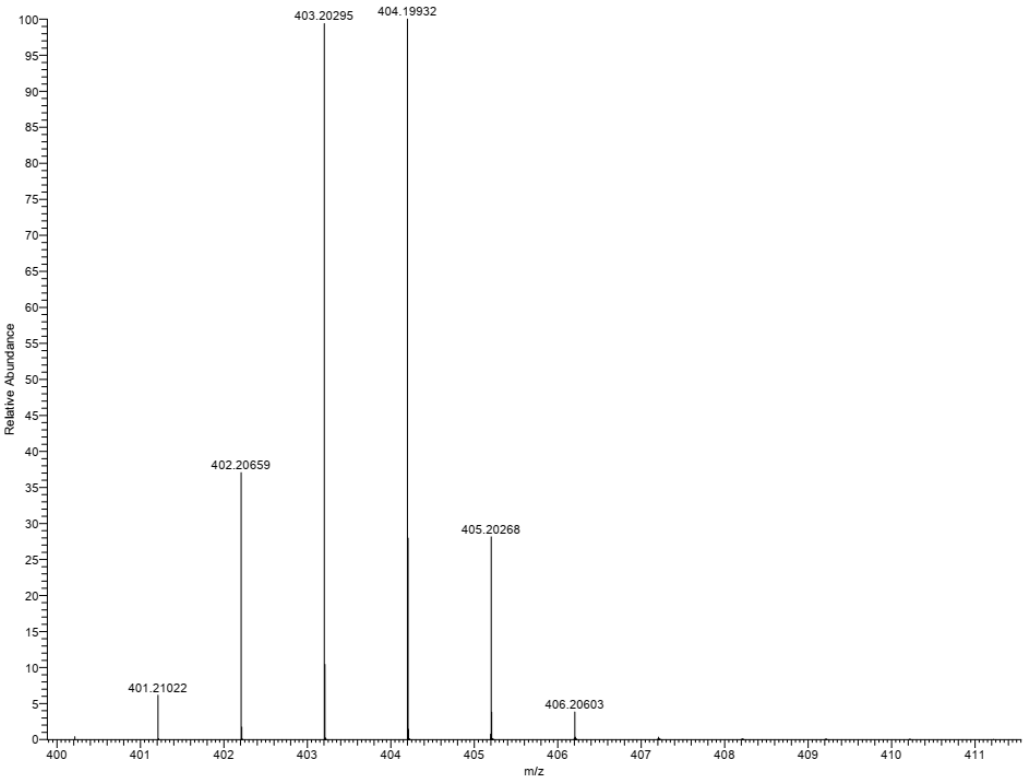

Figure S70: Simulated high-resolution mass spectrum of compound $[\mathbf{2}^{H}]^{\bullet+}$. Note that for technical reasons the *m*/*z* scale differs between the respective experimental and simulated mass spectra.

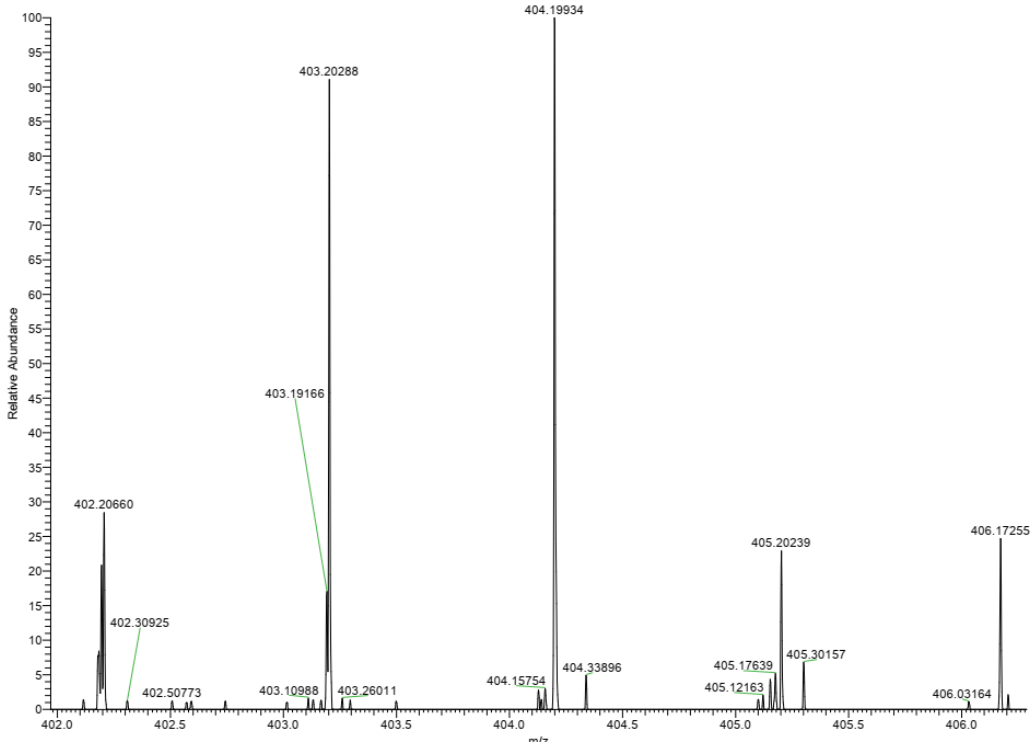

Figure S71: High-resolution mass spectrum of $[\mathbf{2}^{H}]^{\bullet+}$ measured in positive mode using a *Thermo Fisher Scientific* MALDI LTQ Orbitrap XL spectrometer and *α*-cyano-4-hydroxycinnamic acid as the matrix. Note that for technical reasons the *m*/*z* scale differs between the respective experimental and simulated mass spectra.

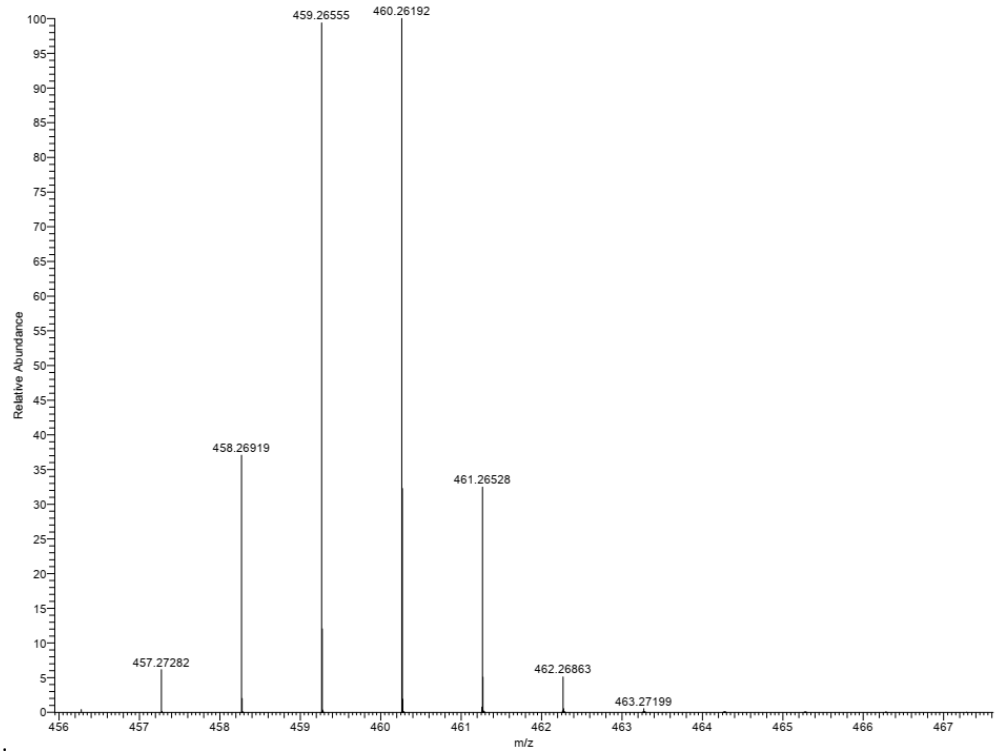

Figure S72: Simulated high-resolution mass spectrum of compound $[\mathbf{2}^{\mathbf{Me}}]^{\bullet+}$. Note that for technical reasons the *m*/*z* scale differs between the respective experimental and simulated mass spectra.

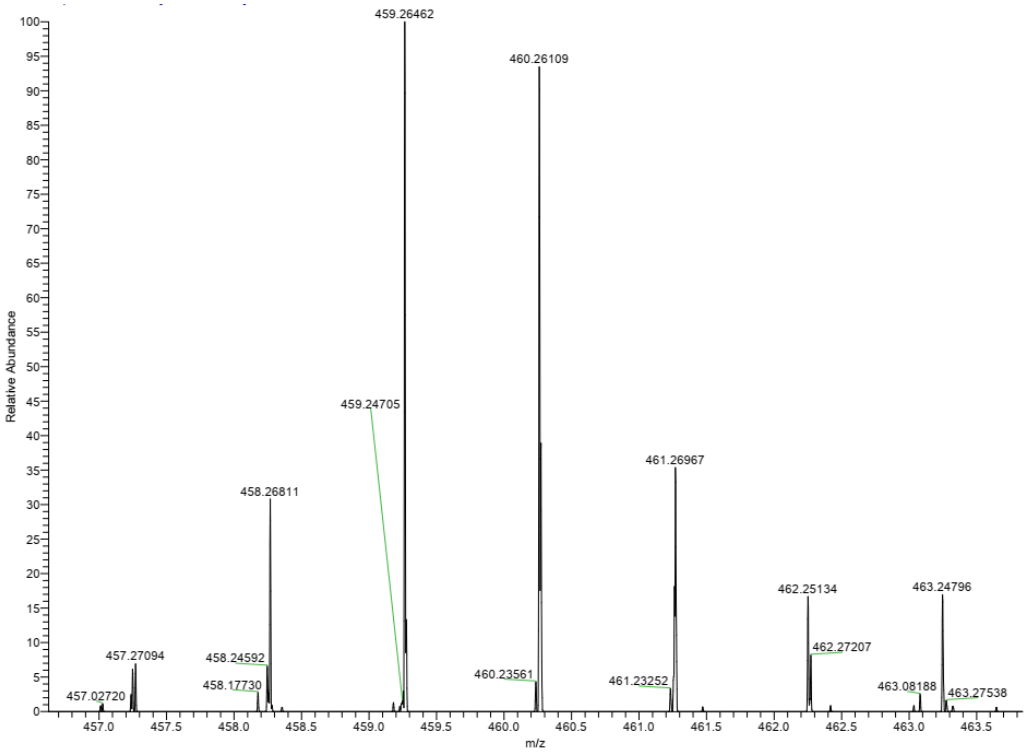

Figure S73: High-resolution mass spectrum of $[\mathbf{2}^{\mathbf{Me}}]^{\bullet+}$ measured in positive mode using a *Thermo Fisher Scientific* MALDI LTQ Orbitrap XL spectrometer and *α*-cyano-4-hydroxycinnamic acid as the matrix. Note that for technical reasons the *m*/*z* scale differs between the respective experimental and simulated mass spectra.

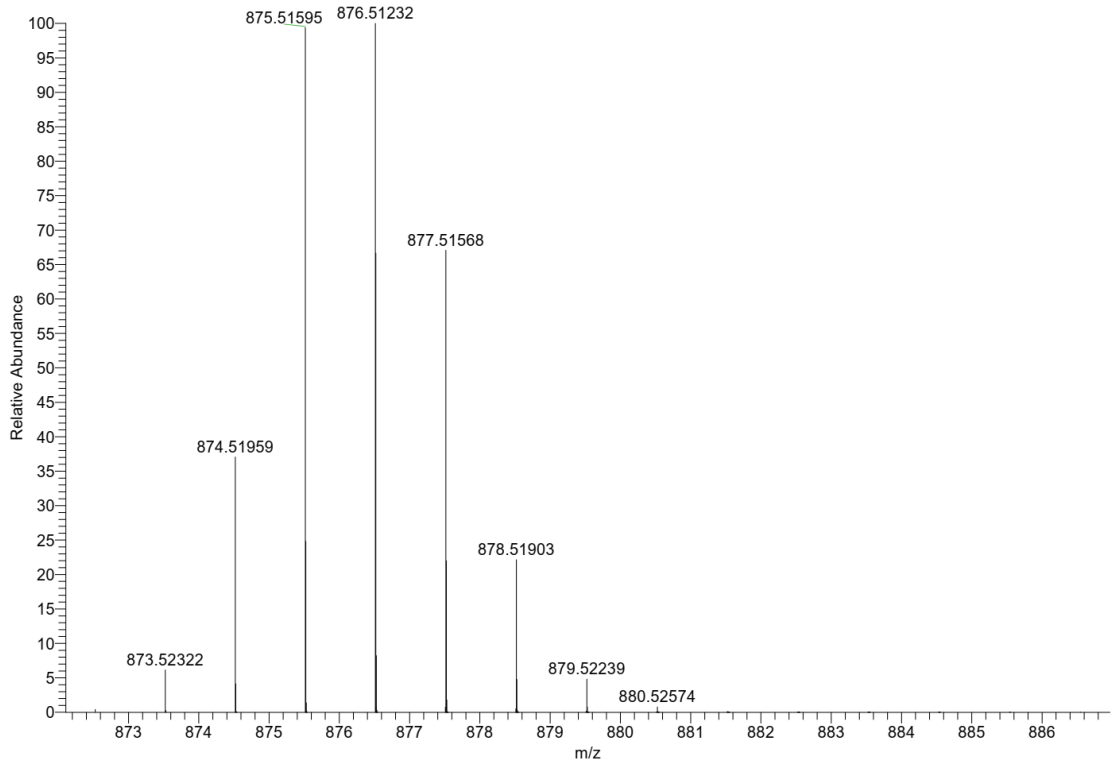

Figure S74: Simulated high-resolution mass spectrum of compound $[\mathbf{2}^{\mathbf{Mes}}]^{\bullet+}$. Note that for technical reasons the *m*/*z* scale differs between the respective experimental and simulated mass spectra.

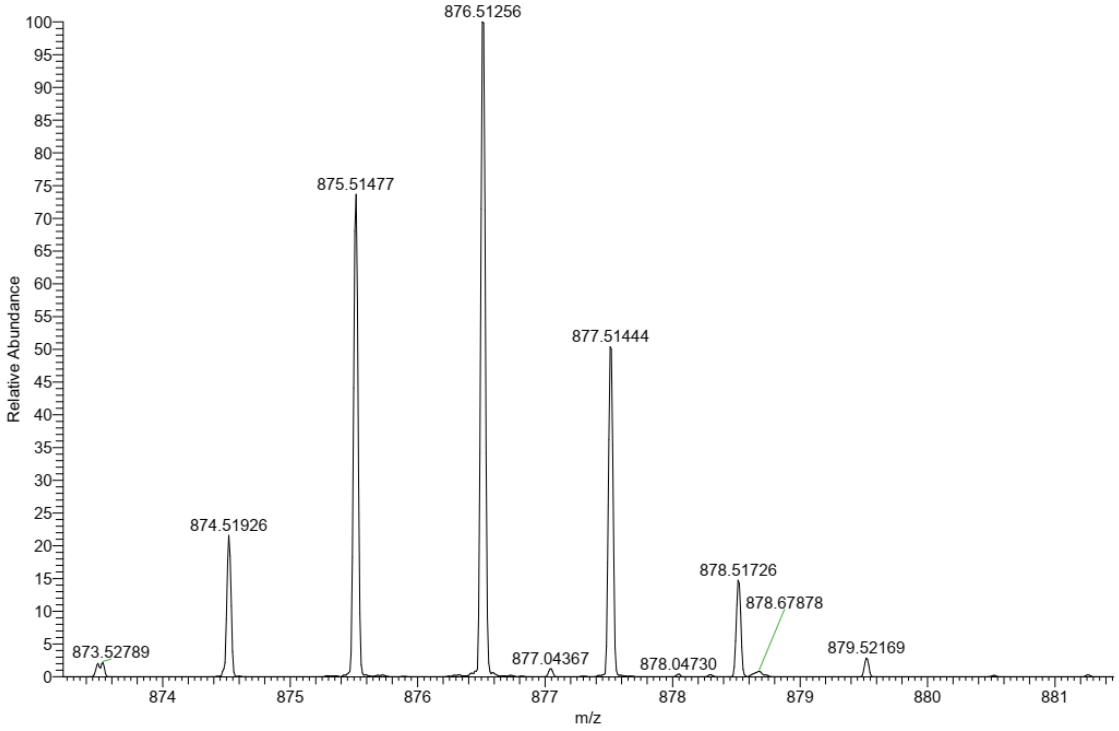

Figure S75: High-resolution mass spectrum of $[\mathbf{2}^{\mathbf{Mes}}]^{\bullet+}$ measured in positive mode using a *Thermo Fisher Scientific* MALDI LTQ Orbitrap XL spectrometer and *α*-cyano-4-hydroxycinnamic acid as the matrix. Note that for technical reasons the *m*/*z* scale differs between the respective experimental and simulated mass spectra.

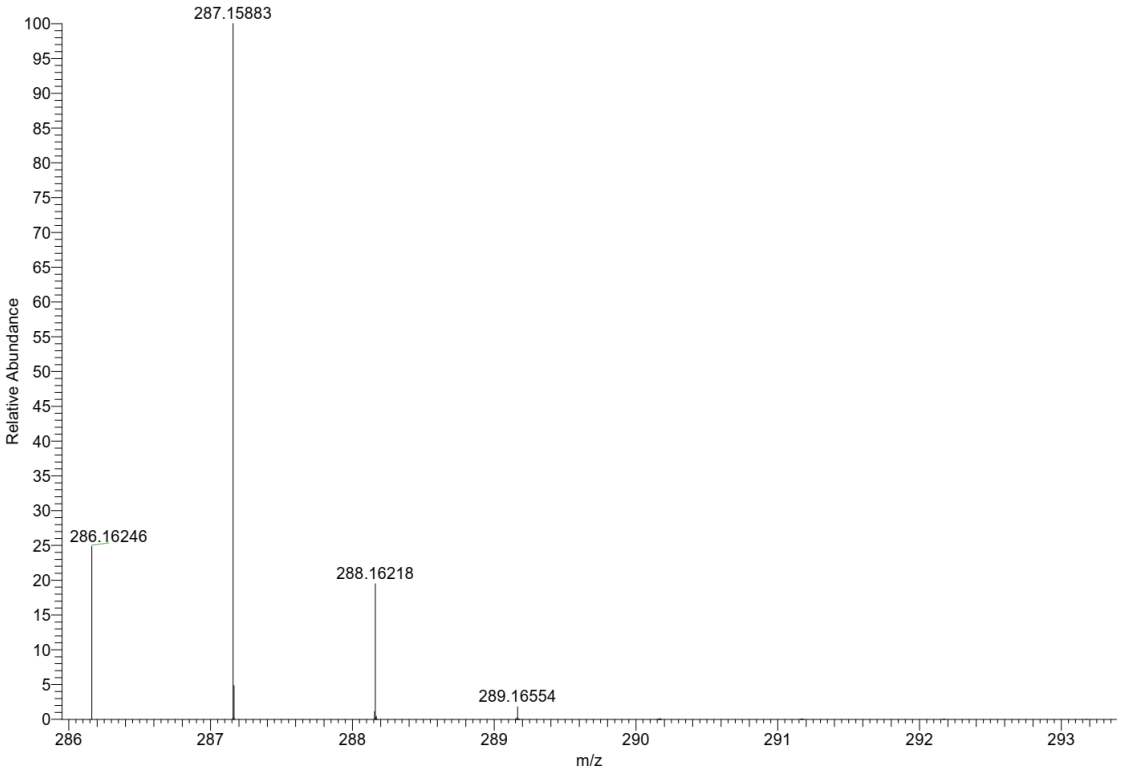

Figure S76: Simulated high-resolution mass spectrum of compound $[\mathbf{5}]^{\bullet+}$. Note that for technical reasons the *m*/*z* scale differs between the respective experimental and simulated mass spectra.

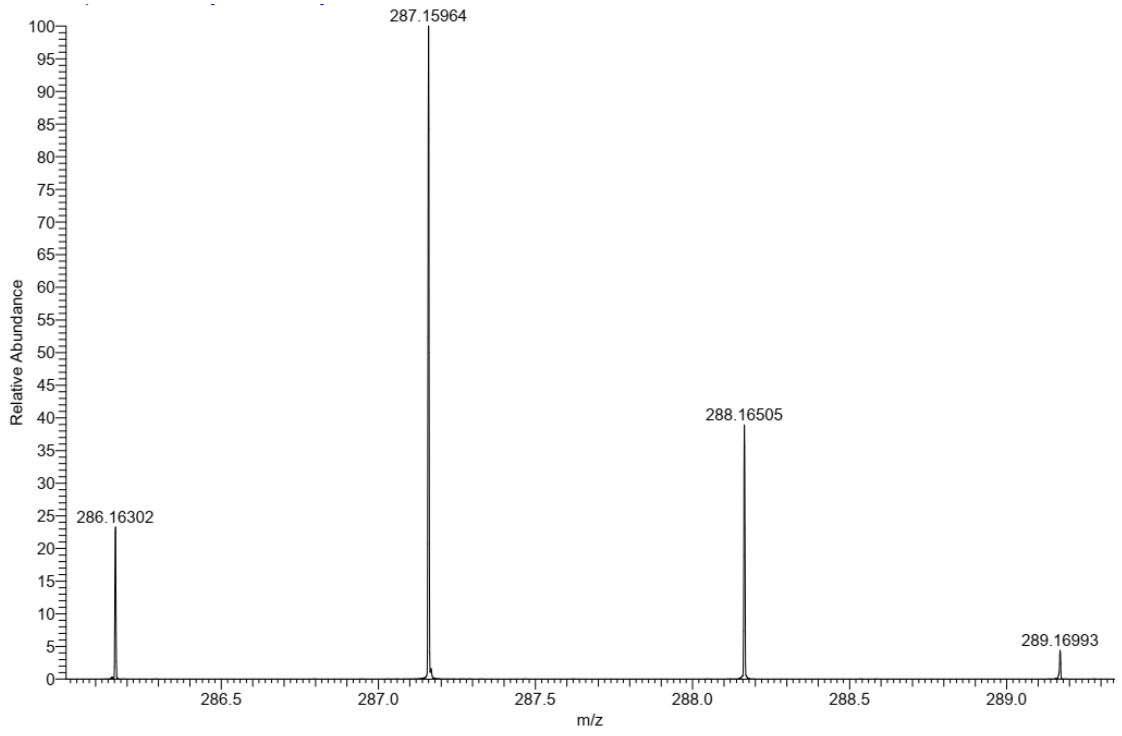

Figure S77: High-resolution mass spectrum of $[\mathbf{5}]^{\bullet+}$ measured in positive mode using a *Thermo Fisher Scientific* MALDI LTQ Orbitrap XL spectrometer and α-cyano-4-hydroxycinnamic acid as the matrix. Note that for technical reasons the *m*/*z* scale differs between the respective experimental and simulated mass spectra.

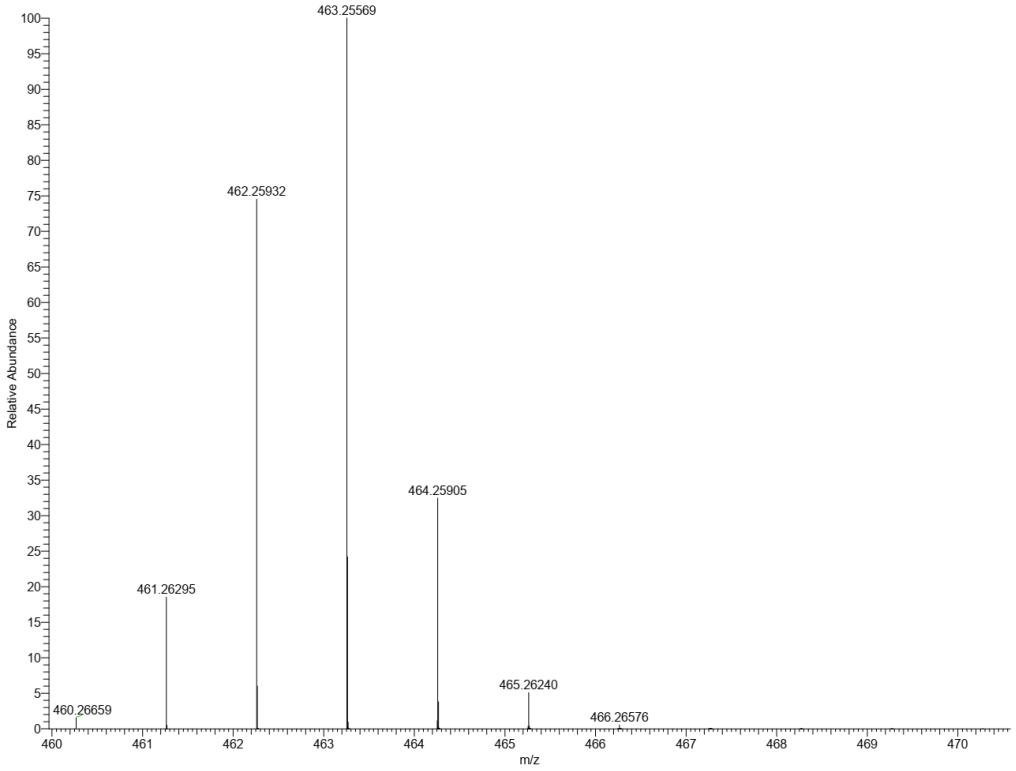

Figure S78: Simulated high-resolution mass spectrum of compound $[\mathbf{3}^{\mathbf{Me,Me}}]^{\bullet+}$. Note that for technical reasons the *m*/*z* scale differs between the respective experimental and simulated mass spectra.

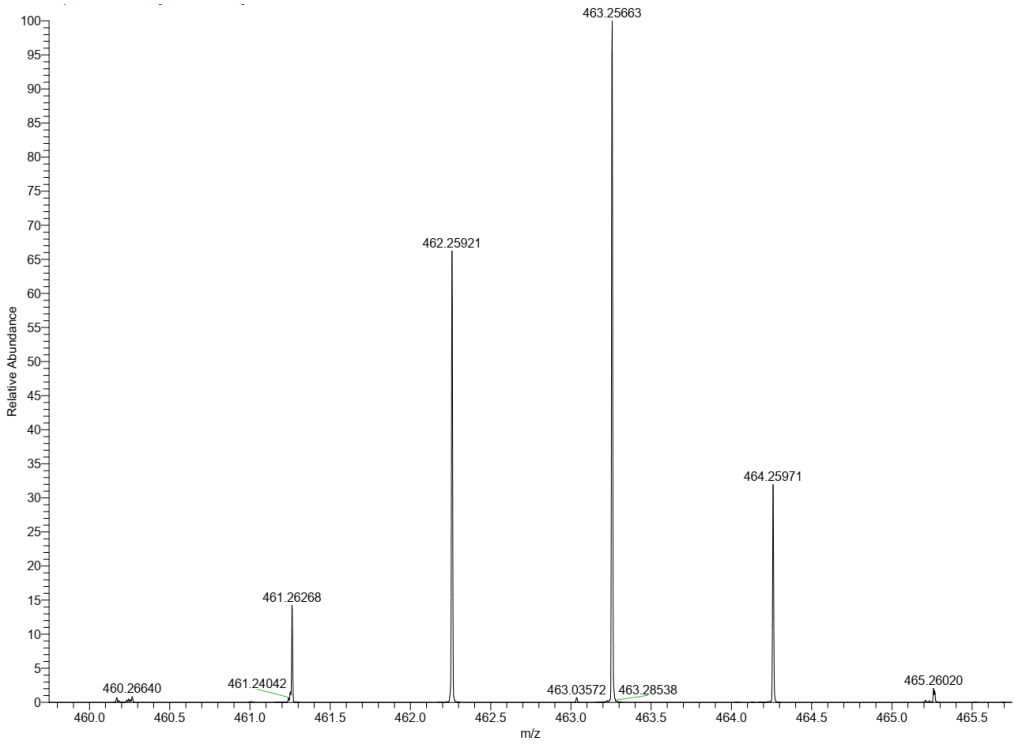

Figure S79: High-resolution mass spectrum of $[\mathbf{3}^{\mathbf{Me,Me}}]^{\bullet+}$ measured in positive mode using a *Thermo Fisher Scientific* MALDI LTQ Orbitrap XL spectrometer and *α*-cyano-4-hydroxycinnamic acid as the matrix. Note that for technical reasons the *m*/*z* scale differs between the respective experimental and simulated mass spectra.

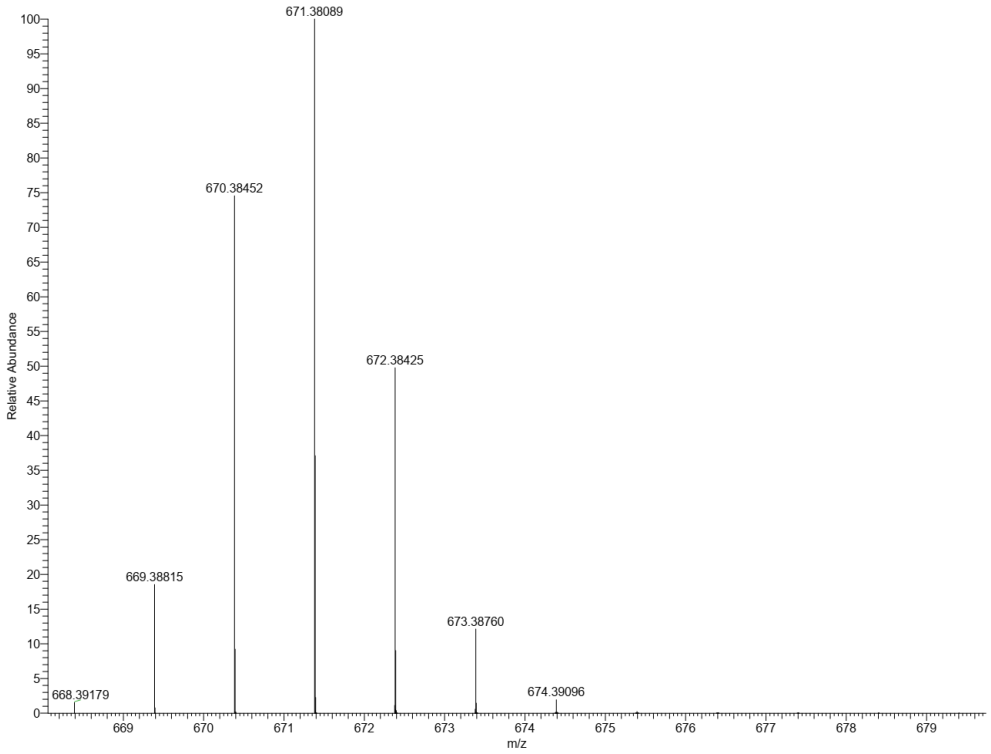

Figure S80: Simulated high-resolution mass spectrum of compound $[\mathbf{3}^{\mathbf{Me,Mes}}]^{\bullet+}$. Note that for technical reasons the *m*/*z* scale differs between the respective experimental and simulated mass spectra.

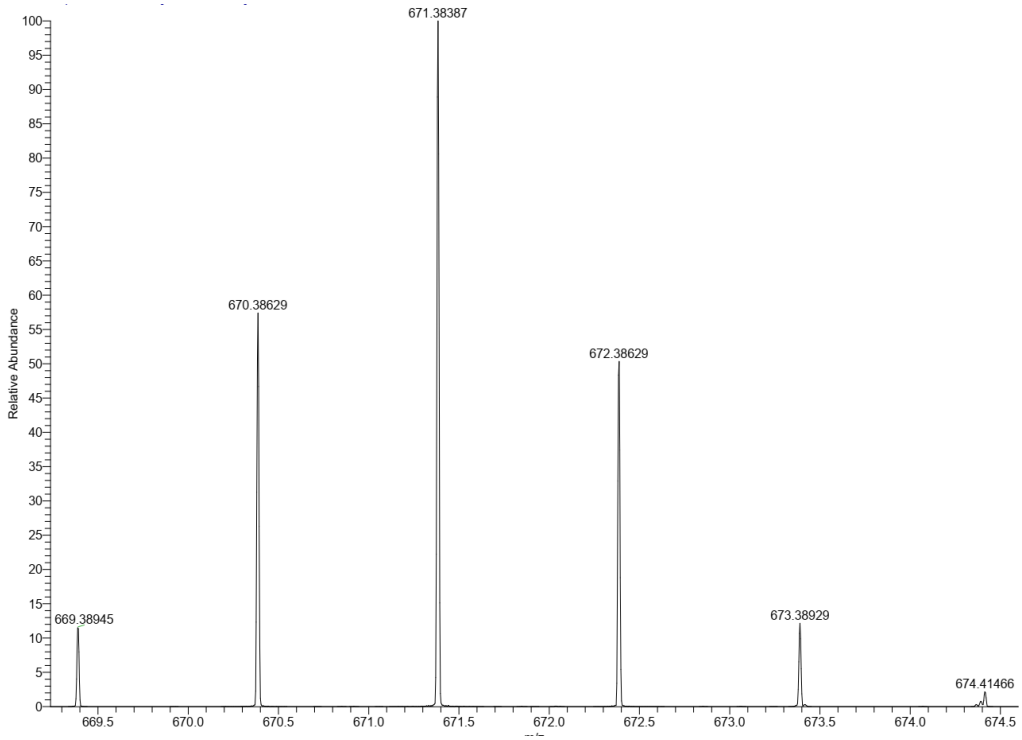

Figure S81: High-resolution mass spectrum of $[\mathbf{3}^{\mathbf{Me,Mes}}]^{\bullet+}$ measured in positive mode using a *Thermo Fisher Scientific* MALDI LTQ Orbitrap XL spectrometer and *α*-cyano-4-hydroxycinnamic acid as the matrix. Note that for technical reasons the *m*/*z* scale differs between the respective experimental and simulated mass spectra.

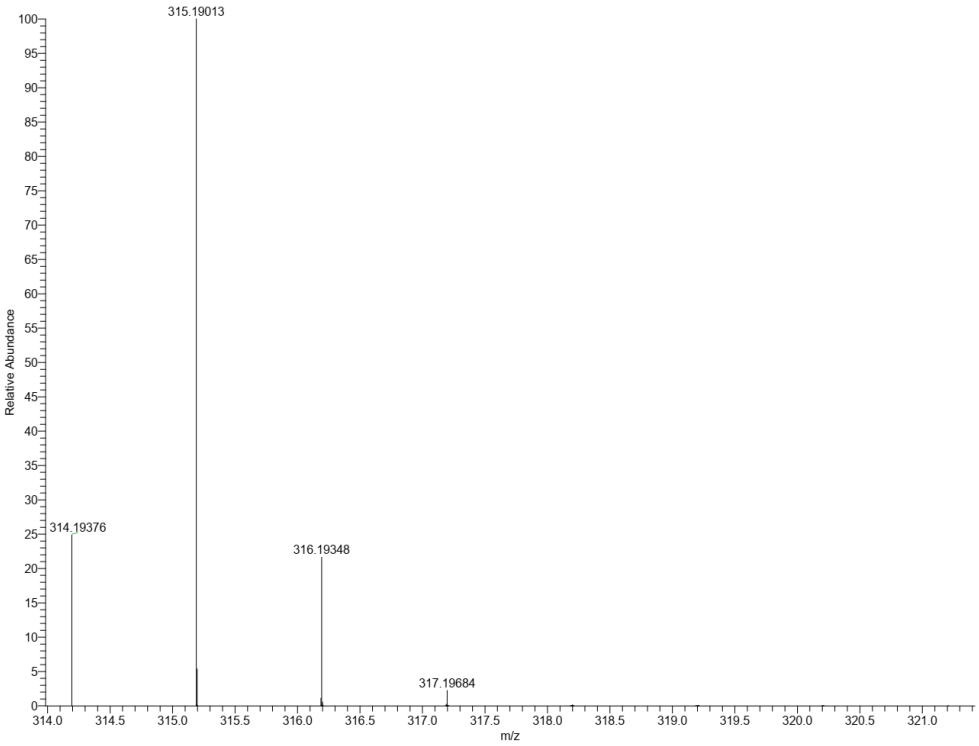

Figure S82: Simulated high-resolution mass spectrum of compound [**6**]$^{\bullet+}$. Note that for technical reasons the *m*/*z* scale differs between the respective experimental and simulated mass spectra.

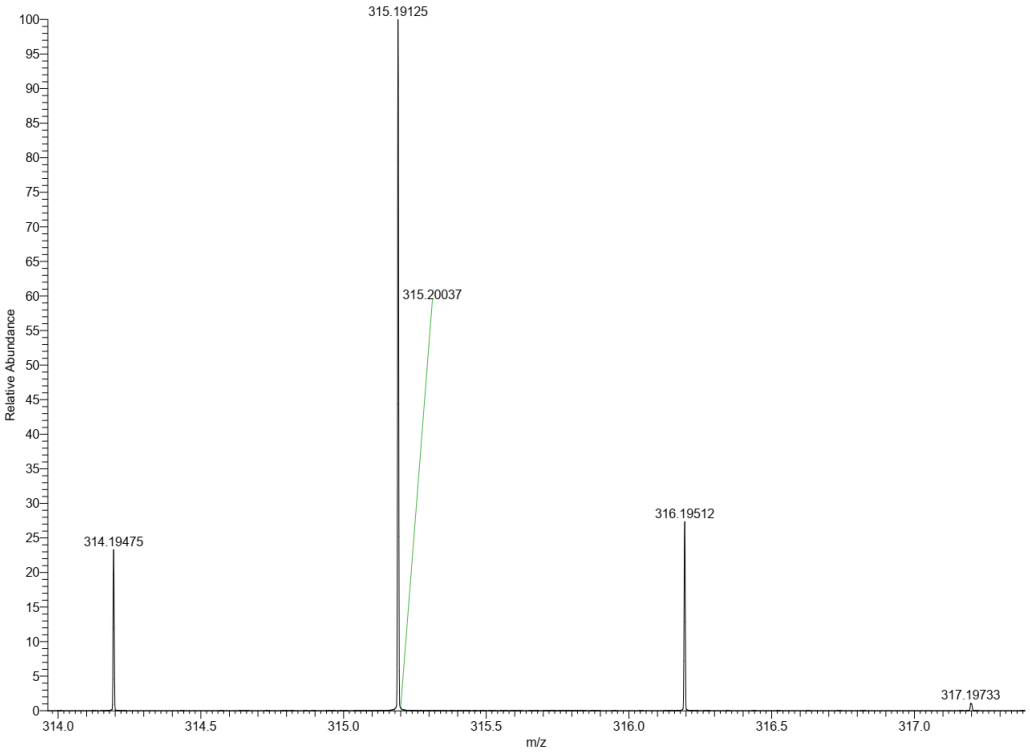

Figure S83: High-resolution mass spectrum of [**6**]$^{\bullet+}$ measured in positive mode using a *Thermo Fisher Scientific* MALDI LTQ Orbitrap XL spectrometer and *α*-cyano-4-hydroxycinnamic acid as the matrix. Note that for technical reasons the *m*/*z* scale differs between the respective experimental and simulated mass spectra.

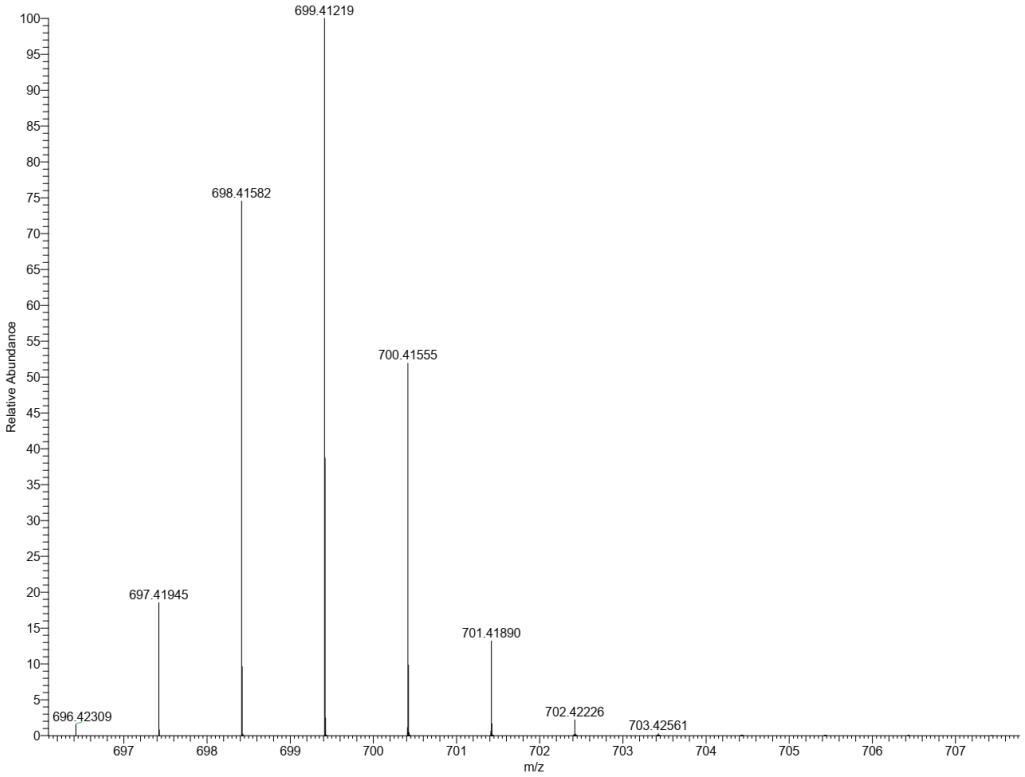

Figure S84: Simulated high-resolution mass spectrum of compound $[\mathbf{4}^{\mathbf{Me,Mes}}]^{\bullet+}$. Note that for technical reasons the *m*/*z* scale differs between the respective experimental and simulated mass spectra.

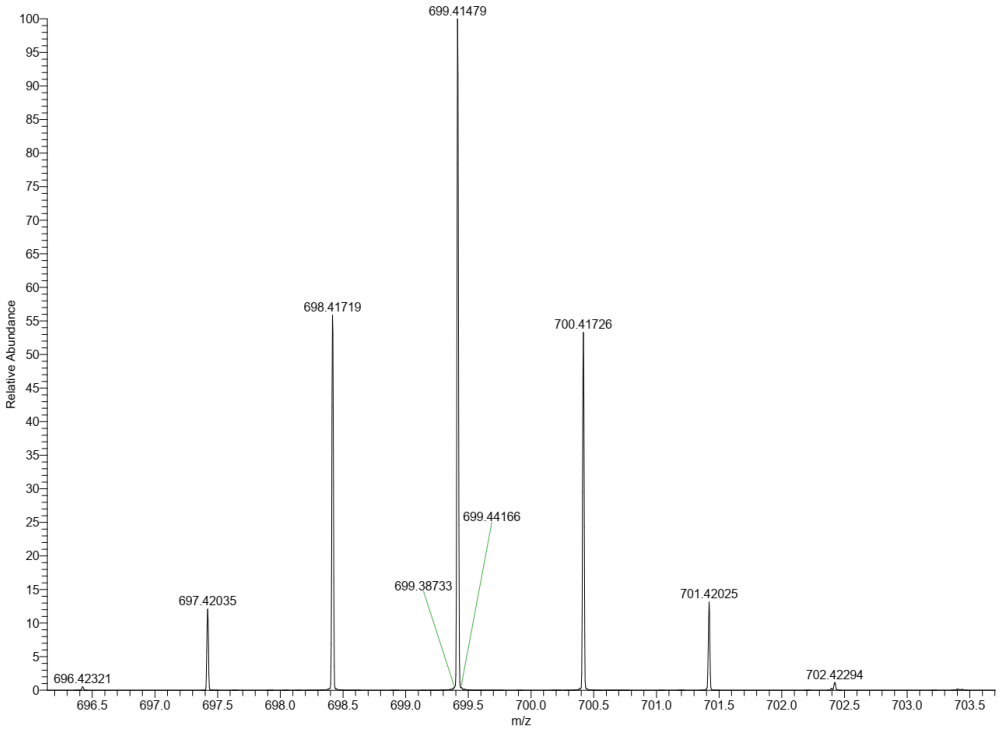

Figure S85: High-resolution mass spectrum of $[\mathbf{4}^{\mathbf{Me,Mes}}]^{\bullet+}$ measured in positive mode using a *Thermo Fisher Scientific* MALDI LTQ Orbitrap XL spectrometer and *α*-cyano-4-hydroxycinnamic acid as the matrix. Note that for technical reasons the *m*/*z* scale differs between the respective experimental and simulated mass spectra.

7. Computational details

7.1. Programs

Quantum-chemical computations were performed with a suite of software packages: Q-Chem 5.4.2[S13] for TDA-DFT,[S14–S16] optimal tuning,[S17,S18] and ΔUKS[S19] excited state optimization; TURBOMOLE 7.5.1[S20,S21] for DFT single-points and optimizations during CENSO; COSMOtherm16[S22] for COSMO-RS[S23,S24] calculations during CENSO runs; ORCA 5.0.4[S25] for DFT ground state optimizations and redox potentials; CREST 2.12[S26] for conformer searches; CENSO 1.2.0[S27] for conformer ensemble energy ranking and refinement; and xtb[S28,S29] for molecular dynamics simulations during the CREST runs. We employ standard settings for integration grids and convergence criteria during single-point and geometry optimizations. Initial molecular structures were generated with the Avogadro[S30] program. Visualizations of the molecular geometry and density isosurface plots were created with the vmd 1.9.3[S31] program package.

7.2. Geometries and conformational search

The computational protocol for the generation of relevant ground and excited state structures closely adheres to the procedure outlined in our previous work.[S2] For each compound, a conformer search was conducted with the CREST program at the GFN2-xTB[S28] level of theory. Solvation effects were considered using the ALPB[S32] solvation model. Separate CREST runs were carried out for benzene, THF, and water as the solvent, ensuring a complete ground state conformer ensemble for the later excited-state geometry optimization. The resulting conformer ensembles were refined and sorted using the CENSO program up to part2 in combination with the TURBOMOLE program. In this course, geometries and single-point energies were refined at the r^{2}SCAN-3c[S33] level of theory. The free energy contribution of solvation was included with dCOSMO-RS[S34] during geometry optimization and COSMO-RS during single-point free energy calculation, using parameters for the same solvents as in the prior CREST runs. The thermostatistical free energy contribution was calculated using the modified rigid-rotor-harmonic-oscillator approximation (mRRHO)[S35] within the single-point hessian[S36] approximation for GFN2-xTB. The complete level of theory is denoted as r^{2}SCAN-3c + COSMORS[benzene/THF/H_2O] + mRRHO(GFN2[ALPB]-bhess) // r^{2}SCAN-3c[DCOSMO-RS].

For compounds **1**^{Me}, **2**^{Me}, and **3**^{Me,Me}, the most stable conformer exhibits a parallel alignment of the NBN/BNB-phenalenyl-moieties (denoted dan and dbn), while a few conformers within an energy range of 0.5 kcal/mol are slightly twisted (up to 30°) along the bridging 1,4-phenylene. Due to the bulky mesityl units, **3**^{Me,Mes} tends to a twisted structure (25°), although the fully parallel conformation remains within 0.5 kcal/mol of the lowest energy conformer. The further methylation of the bridging 1,4-phenylene unit in **4**^{Me,Mes} enforces an orthogonal arrangement (> 80° N-B-C-C dihedral angle) between the dan-unit and the bridging 1,4-xylenylene. In turn, this favors a twisted conformation between the dan and dbn-units. Furthermore, the mesityl groups lead to a slight bend along the bridging 1,4-phenylene or 1,4-xylenylene unit. The twice-mesitylated **2**^{Mes} is dominated by sterical crowding, leading to a dihedral angle of about 60° between the dbn-units.

From the ground state ensembles at the r^{2}SCAN-3c level of theory, the two lowest structurally distinct conformers served as the starting point for both the calculation of absorption energies and the optimization of excited state geometries. For the former, the ground state geometries were reoptimized at the r^{2}SCAN-3c/SMD[S37] level of theory in the Orca program, employing the same solvent parameters as

in the subsequent excited state calculation. For the excited state geometry optimization, we applied the ΔSCF treatment of the singlet excited states based on unrestricted Kohn-Sham DFT in combination with the integral-equation formalism polarizable continuum model IEF-PCM[S38–S40] (denoted ΔSCF/UKS/PCM) in the Q-Chem program package. To prevent the UKS wavefunction from collapsing to the variational ground state, we utilized the maximum overlap method with the initial reference density (IMOM).[S19] ΔSCF/UKS/PCM accounts for both orbital relaxation and solvation effects during geometry optimization, particularly affecting charge-transfer (CT) excited states.[S41–S43] We demonstrated the applicability of ΔSCF/UKS/PCM for the local (LE) and CT states of the phenalenyl derivatives in our previous work through comparison to both experimental emission energies and the second-order algebraic-diagrammatic construction method (ADC(2)).[S2] Considering the greater system size of the investigated bridged dyads, we omit further testing against correlated wavefunction methods. All excited state geometry optimizations employ the OT-LRC-ωPBEh[S44] functional (vide infra) with a def2-SVP[S45,S46] basis set and the DFT-D4 dispersion correction,[S47,S48] employing damping parameters suggested recently for the default ω-value.[S49] In the case where different conformers persist after excited state optimization, we calculated emission energies for both and selected for each state the conformer with the lower energy of the equilibrated excited state at the TDA-DFT/SS-PCM[S50,S51] level of theory (vide infra). This procedure circumvents the need for consistent TDA-DFT/SS-PCM excited state geometry optimization, which is not feasible due to the unavailability of analytical nuclear gradients for the SS-PCM solvation model.

For the calculation of relaxed redox potentials, we reoptimized the ground state geometries of the neutral, as well as singly and doubly anionic and cationic species at the r^{2}SCAN-3c/SMD[THF][S37] level of theory with the Orca program.

7.3. Optimal tuning

For all excited state (TDA)-DFT calculations, we employed the range-separated hybrid functional LRC-ωPBEh due to its beneficial performance for excited state applications. To optimize LRC-ωPBEh for the application at hand, we applied the non-empirical and system-specific procedure of optimal tuning. This procedure determines an optimal value for the range-separation parameter ω, ensuring that the final functional (OT-LRC-ωPBEh) satisfies Koopman's theorem. The tuning procedure follows the slightly modified approach of Head-Gordon et al.,[S52] minimizing the deviation between the negative energy of the highest occupied molecular orbital (HOMO) and the first ionization potential (calculated via ΔSCF) for the neutral species and the anion. All calculations of the cationic, anionic, and neutral molecule were conducted at the r^{2}SCAN-3c-optimized neutral ground state geometries in the gas phase.

Optimal tuning was performed individually for the chosen conformer of each compound. For all compounds except **2^{Mes}**, the optimal ω values are very similar (within 0.01 Bohr^{-1}). Consequently, we employed a fixed average value for ω of 0.154 Bohr^{-1} in all calculations of these compounds. Only for **2^{Mes}** requires a distinct ω-value of 0.125 Bohr^{-1} was used.

7.4. Calculation of absorption energies

Vertical absorption energies E^c_{abs} were computed with time-dependent density functional theory in the Tamm-Dancoff approximation (TDA-DFT) at the r^2-SCAN-3c/SMD optimized ground state geometry in the Q-Chem program package. All calculations employ the system-specific OT-LRC-ωPBEh density functional

(vide supra). To capture the sizable solvation effects arising from the polar nature of the CT excited states, we employed perturbative state-specific PCM (ptSS-PCM)[S53,S54] in the non-equilibrium regime. This method relaxes only the fast (electronic) degrees of freedom defined by the refractive index n of the solvent to the excited state density.[S55] All calculations use the def2-TZVPP basis set.[S45,S46]

7.5. Calculation of emission energies

As for the absorption energies, vertical emission energies E^{c}_{em} were calculated with TDA-DFT/OT-LRC-ωPBEh for the two excited state conformers optimized with ΔSCF/UKS/PCM. This is crucial to determine the overall lowest excited state, which dominates the emission according to Kasha's rule.[S56] Solvation effects in the excited state were included based on fully iterative state-specific PCM (SS-PCM, or PTED-SS-PCM for perturbation of energy and density in the literature). To describe the vertical emission process, a non-equilibrium ptSS-PCM correction is again applied. All calculations employ the def2-SVP basis set during the iterative equilibration of the reaction field, followed by a final energy evaluation with the converged reaction field using the def2-TZVPP basis set.

7.6. Calculation of redox potentials

The adiabatic first and second potentials for both reduction and oxidation were calculated for all compounds employing the r^2SCAN-3c/SMD[THF] relaxed geometries for each charge state. Calculations were performed with both the B3LYP-D4[S57,S58] and ωB97X-D3[S59–S61] density functionals employing the minimally augmented ma-def2-QZVPP[S45,S46,S62] basis set to ensure a proper description of the negatively charged species. Solvation effects were considered based on the SMD model using the THF parameters. The redox potentials were evaluated against the FcH/FcH^{+} redox couple calculated at the same level of theory. All calculations were performed with the Orca program.

7.7. Results: absorption energies

Table S13 compiles the vertical absorption energies (E^c_{abs}), oscillator strengths (f_{osc}), and excited state dipole moments (μ) of the low-lying transitions (S_n) for all investigated compounds in different solvents. The ground state (S_0) geometry used for each calculation is characterized by the two dihedral angles between the NBN/BNB-phenalenyl (denoted dan and dbn) and the bridging unit (dxn-br.), and between the two dxn-units (dxn-dxn). Furthermore, Figure S86 displays the associated unrelaxed difference densities for all transitions.

Focusing on the homodyads **1**^{Me}, **2**^{Me}, and **2**^{Mes}, it becomes evident that absorption is dominated by transitions to locally excited (LE) states on dan or dbn. This preference stems in part from the effective separation afforded by the planar orientation of the two dxn-units in conjunction with the almost orthogonal 1,4-phenylene bridge.[S2] Due to the ensuing symmetry of the respective systems, both dxn-units contribute equally to the LE states, resulting in pairs of states. Despite exhibiting virtually identical density displacements, these pairs can have substantially different oscillator strengths, for instance, in the S_1 and S_2 of **1**^{Me}. Similarly matched states can also be found for the other states in the homodyads.

In **1**^{Me}, the absorption is dominated by the bright S_2 state (E^c_{abs} = 3.99 eV, f_{osc} = 0.104) and the very bright S_3 state (E^c_{abs} = 4.19 eV, f_{osc} = 0.705). In the isostructural BNB-analog **2**^{Me}, only the very bright S_1 state (E^c_{abs} = 4.20 eV, f_{osc} = 0.672) persists. This observation agrees well with the 0.3 eV shift in the experimental onset of the absorption band for **2**^{Me} compared to **1**^{Me}. However, the calculated absolute absorption energies are about 0.6 eV higher than the experimental value, a known issue for the doped phenalenyl derivatives, as previously discussed.[S2] The very bright states S_3 in **1**^{Me} and S_1 in **2**^{Me} feature a nodal plane along the bridge-including C_2-axis, a characteristic also observed for the S_5 transition (E^c_{abs} = 4.11 eV, f_{osc} = 0.588) of the mesitylated **2**^{Mes}. Notably, this state appears at a slightly lower absorption energy, consistent with the marginally earlier onset of the absorption compared to **2**^{Me} measured experimentally (3.63 eV vs. 3.70 eV). The mesityl-to-dbn charge transfer excitations (E^c_{abs} = 3.78 eV, f_{osc} = 0.010) arise at lower energies but do not significantly contribute to the absorption spectrum due to their low oscillator strength.

Moving now to the heterodyads **3**^{Me,Me}, **3**^{Me,Mes}, and **4**^{Me,Mes}, we observe absorption properties that resemble an overlay of the dan- and dbn-based homodyads. **3**^{Me,Me} exhibits both the LE transition on the dan-unit (S_1: E^c_{abs} = 3.99 eV, f_{osc} = 0.052) seen for **1**^{Me} and the very bright LE transition on both the dan- and dbn-subunit (S_2: E^c_{abs} = 4.19 eV, f_{osc} = 0.684) seen for all homodyads. The same overlay is also observed experimentally, with a first absorption peak of lower intensity at 3.4 eV followed by a more intense absorption at 3.73 eV. The very weak experimental absorption at 2.60 eV, attributed to the dan-to-dbn CT state, is not found theoretically, likely due to the geometry favoring local excitations (see above). Introducing the mesityl group in **3**^{Me,Mes} leads to a blend of the mes-to-BNB-CT and the bright dan/dbn LE states, resulting in two bright states (S_3: E^c_{abs} = 4.13 eV, f_{osc} = 0.052 and S_4: E^c_{abs} = 4.20 eV, f_{osc}=0.395) alongside from the separated LE on the NBN-phenalenyl (E^c_{abs} = 3.98 eV, f_{osc} = 0.045). The introduction of methyl groups on the bridging 1,4-phenylene in **4**^{Me,Mes} leaves the absorption properties unaffected, as **3**^{Me,Mes} already orients the dan-unit and 1,4-phenylene bridge almost orthogonally. In turn, both **3**^{Me,Mes}, and **4**^{Me,Mes} show an early onset of absorption similar to **3**^{Me,Me}.

Overall, for both homo- and heterodyads, the calculated absorption energies agree well with the experimental observation, which supports the hypothesis that absorption mainly populates locally excited states. Subsequent emission from different excited states thus requires prior internal conversion (see below).

Table S13: Vertical absorption energies (E^c_{abs}), excited state dipole moments (μ), and oscillator strengths (f_{osc}) at the TDA-OT-LRC-ωPBEh/def2-TZVPP/ptSS-PCM level of theory for different solvents. All calculations are performed at the ground state r^2SCAN-3c/SMD structure optimized with the same solvent used in the later calculation. Additionally, the dihedral angles θ_1, between the NBN/BNB-phenalenyl and the 1,4-phenylene/xylylene unit (dxn-br.), and θ_2, between the two NBN/BNB-phenalenyl units (dxn-dxn), is reported for the S_0 structure.

Solv.	θ_1/° dxn-br.	θ_2/° dxn-dxn	μ/D	f_{osc}	E^c_{abs}/eV	μ/D	f_{osc}	E^c_{abs}/eV	μ/D	f_{osc}	E^c_{abs}/eV
1^{Me}	**S_0**		**S_1**			**S_2**			**S_3**		
C_6H_{12}	88.0	0.1	0.0	0.000	4.01	0.0	0.101	4.01	0.0	0.696	4.21
C_6H_6	87.7	0.1	0.0	0.000	4.01	0.0	0.101	4.01	0.0	0.697	4.21
THF	84.1	0.1	0.0	0.000	3.99	0.0	0.104	3.99	0.0	0.705	4.19
CH_2Cl_2	84.3	0.0	0.0	0.000	3.99	0.0	0.104	3.99	0.0	0.705	4.19
H_2O	68.7	0.1	0.0	0.000	3.96	0.0	0.086	3.96	0.0	0.722	4.18
2^{Me}	**S_0**		**S_1**								
C_6H_{12}	78.3	0.0	0.0	0.676	4.20						
C_6H_6	78.8	22.4	0.0	0.675	4.20						
THF	90.1	0.0	0.0	0.662	4.19						
CH_2Cl_2	78.3	0.0	0.0	0.672	4.20						
H_2O	77.6	0.1	0.0	0.675	4.22						
2^{Mes}	**S_0**		**S_1**			**S_5**					
C_6H_{12}	60.1	60.4	2.3	0.010	3.77	0.1	0.602	4.10			
C_6H_6	60.1	60.4	2.2	0.010	3.76	0.2	0.602	4.10			
THF	60.0	60.4	2.0	0.010	3.78	0.1	0.591	4.11			
CH_2Cl_2	60.0	60.4	2.1	0.010	3.78	0.1	0.588	4.11			
H_2O	60.0	60.4	1.9	0.010	3.81	0.3	0.560	4.11			
3^{Me,Me}	**S_0**		**S_1**			**S_2**					
C_6H_{12}	89.9	0.5	3.4	0.050	4.01	4.5	0.624	4.19			
C_6H_6	89.9	0.6	3.5	0.051	4.01	4.6	0.633	4.19			
THF	89.8	0.6	4.0	0.052	3.99	4.8	0.683	4.19			
CH_2Cl_2	89.8	0.7	4.1	0.052	3.99	4.8	0.684	4.19			
H_2O	78.0	33.7	3.8	0.045	3.97	5.0	0.621	4.19			
3^{Me,Mes}	**S_0**		**S_1**			**S_3**			**S_4**		
C_6H_{12}	63.9	11.5	4.1	0.043	4.00	0.4	0.255	4.10	1.3	0.468	4.20
C_6H_6	64.1	11.5	4.2	0.044	4.00	0.6	0.263	4.11	0.9	0.435	4.20
THF	65.5	8.0	4.7	0.044	3.98	1.9	0.324	4.12	3.6	0.412	4.20
CH_2Cl_2	65.8	8.2	4.7	0.045	3.98	2.1	0.337	4.13	3.7	0.395	4.20
H_2O	64.9	3.2	4.6	0.041	3.96	2.3	0.327	4.11	4.7	0.390	4.20
4^{Me,Mes}	**S_0**		**S_1**			**S_3**			**S_4**		
C_6H_{12}	65.0	21.4	4.0	0.050	4.01	2.3	0.171	4.08	1.6	0.511	4.19
C_6H_6	65.3	21.4	4.0	0.050	4.01	2.1	0.179	4.08	1.6	0.515	4.19
THF	66.9	21.0	4.5	0.051	3.99	2.2	0.230	4.11	2.5	0.517	4.19
CH_2Cl_2	67.2	20.8	4.5	0.051	3.99	2.2	0.247	4.11	2.6	0.498	4.19
H_2O	66.7	20.5	4.8	0.051	3.98	2.6	0.257	4.11	3.6	0.465	4.19

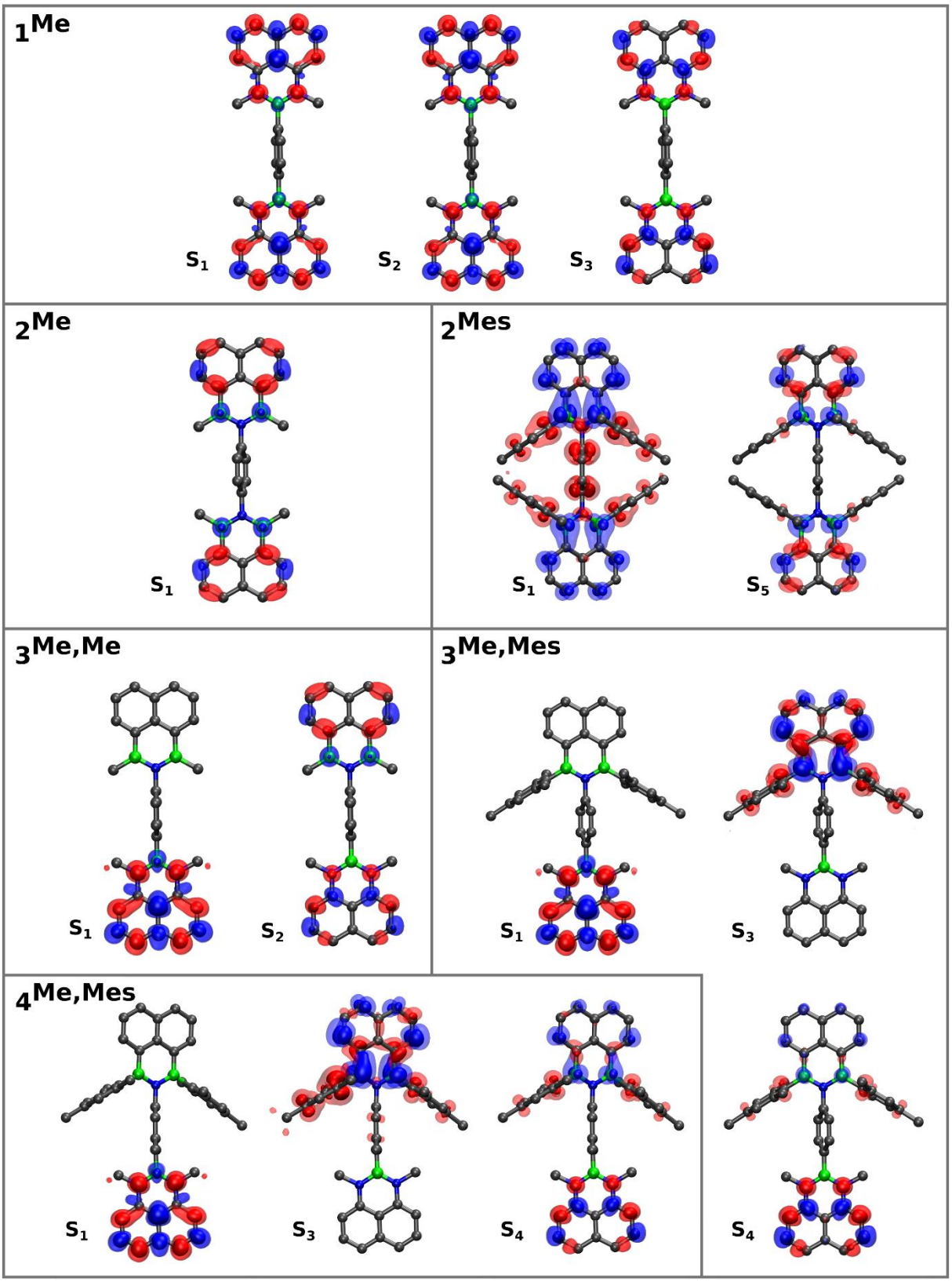

Figure S86: Unrelaxed difference densities for the singlet excited states (S_n) reached after absorption at the ground state geometry calculated at the TDA-OT-LRC-ωPBEh/def2-TZVPP/ptSS-PCM[CH_2Cl_2] level of theory. Red represents the hole- and blue the electron density. All plots employ 0.997 [opaque] and 0.999 [translucent] as isovalues.

7.8. Results: emission energies

Table S14 lists the vertical emission energies (E^{c}_{abs}), oscillator strengths (f_{osc}), and excited state dipole moments (μ) of the lowest two excited states for the investigated compounds in various solvents. Due to the lack of analytical nuclear gradients of the SS-PCM model, we calculated the excited state energies at ΔSCF/UKS/PCM optimized geometries (see above). Hence, we report the results for the geometry with the lower absolute excited state energy. Notably, the reported energy gap between the first and second excited states (ΔE_{12}) deviates from the difference in emission energies due to the difference in geometry and the state-specific nature of the solvation model. Figure S87 displays the associated unrelaxed difference density for all excited states.

The isostructural homodyads $\mathbf{1}^{\mathbf{Me}}$ and $\mathbf{2}^{\mathbf{Me}}$ each manifest two distinct states: (1) a lower, less twisted, and dark CT state from [to] the dan [dbn] to [from] the 1,4-phenylene bridge for $\mathbf{1}^{\mathbf{Me}}$ [$\mathbf{2}^{\mathbf{Me}}$], and (2) an orthogonal bright LE state on the dxn-moieties similar to the bright state involved in absorption (see above). The opposite direction of the CT confirms the electron-donating and electron-accepting properties of $\mathbf{1}^{\mathbf{Me}}$ and $\mathbf{2}^{\mathbf{Me}}$, respectively. The decisive difference lies in the relative energies of the different states, where the energy gap ΔE_{12} between the S_1 and S_2 is substantially smaller for $\mathbf{2}^{\mathbf{Me}}$ (0.38 eV vs. 0.63 eV). Based on the systematic shift of the LE state to higher energies, the state ordering might even be inverted. We speculate that this smaller (or inverted) gap leads to the different experimental emission characteristics of $\mathbf{1}^{\mathbf{Me}}$ and $\mathbf{2}^{\mathbf{Me}}$, where $\mathbf{1}^{\mathbf{Me}}$ is non-emissive in CH_2Cl_2, whereas $\mathbf{2}^{\mathbf{Me}}$ shows a rather narrow emission at 3.34 eV. Internal conversion from the initially populated LE state (see section 6.7.) to the dark CT states is likely favored in $\mathbf{1}^{\mathbf{Me}}$, similar to simple phenyl-substituted NBN-phenalenyl investigated before (compound **3** in ref. [S2]). Meanwhile, for $\mathbf{2}^{\mathbf{Me}}$, a substantial (or even the complete) population might remain in the orthogonal and bright LE state, leading to the experimentally observed emission.

The mesityl groups in $\mathbf{2}^{\mathbf{Mes}}$ lead experimentally to a broad and bathochromically shifted emission band at 2.86 eV. We attribute this to mixed phenyl- and mesityl-to-dbn-CT states (E^{c}_{em} =2.57 eV, f_{osc}=0.019), which we already observed for the phenyl- substituted BNB-phenalenyl before (compound **6** in ref. [S2]).

The heterodyads $\mathbf{3}^{\mathbf{Me,Me}}$, $\mathbf{3}^{\mathbf{Me,Mes}}$, and $\mathbf{4}^{\mathbf{Me,Mes}}$ introduce the completely dark dan-to-dbn-CT state (E^{c}_{em} = 1.68–1.83 eV, f_{osc} = 0.000). For $\mathbf{3}^{\mathbf{Me,Me}}$, this state is substantially below the LE on the dan-moiety (E^{c}_{em} = 3.85 eV, f_{osc} = 0.040), resulting in a completely non-emissive behavior. The mesityl groups in $\mathbf{3}^{\mathbf{Me,Mes}}$ and $\mathbf{4}^{\mathbf{Me,Mes}}$ allows again for the rather bright mesityl-to-dbn-CT state. Comparison to the experiment shows that both in $\mathbf{3}^{\mathbf{Me,Mes}}$ and $\mathbf{4}^{\mathbf{Me,Mes}}$ exhibit broad emission bands similar to $\mathbf{2}^{\mathbf{Mes}}$, indicating a relevant population of the mesityl-to-dbn-CT state. The substantial energy gap between the dan-to-dbn-CT and mesityl-to-dbn-CT states (ΔE_{12} = 0.8 eV) appears contradictory to this observation. However, the comparison of CT states, especially the very strong dan-to-dbn-CT, is likely associated with a substantial error due to the wrong asymptotic behavior of TDA-DFT, even with the optimally-tuned-RSH OT-LRC-ωPBEh.[S41,S43]

Table S14: Vertical emission energies (E^c_{em}), excited state dipole moments (μ), and oscillator strengths (f_{osc}) at the TDA-OT-LRC-ωPBEh/def2-TZVPP/SS-PCM level of theory for different solvents. All calculations are performed at the ΔSCF/UKS/OT-LRC-ωPBEh/def2-SVP/PCM optimized excited state geometries that minimize the energy of the specific state. For the second excited state (S_2), the absolute energy difference to the first excited state (ΔE_{12}) is given. Additionally, the dihedral angles θ_1, between the NBN/BNB-phenalenyl and the 1,4-phenylene/xylylene unit (dxn-br.), and θ_2, between the two NBN/BNB-phenalenyl units (dxn-dxn), are reported for the respective structures used for the state S_n.

Solv.	θ_1/° dxn-br.	θ_2/° dxn-dxn	μ/D	f_{osc}	E^c_{em}/eV	θ_1/° dxn-br.	θ_2/° dxn-dxn	μ/D	f_{osc}	E^c_{em}/eV	ΔE_{12}/eV
1^{Me}			**S_1**					**S_2**			
C_6H_{12}	39.6	84.7	16.6	0.007	2.92	90.0	0.0	1.1	0.398	3.80	0.51
C_6H_6	39.6	84.7	17.1	0.007	2.89	90.0	0.0	1.1	0.399	3.80	0.52
THF	39.7	87.9	20.7	0.008	2.53	90.0	0.0	1.4	0.403	3.79	0.62
CH_2Cl_2	39.7	88.1	21.0	0.008	2.51	90.0	0.0	1.4	0.404	3.79	0.63
H_2O	40.1	89.4	22.5	0.007	2.30	90.0	0.0	1.5	0.406	3.78	0.69
2^{Me}			**S_1**					**S_2**			
C_6H_{12}	44.6	56.6	15.4	0.009	3.31	88.9	0.0	0.0	0.695	3.98	0.16
C_6H_6	44.6	57.7	15.9	0.009	3.28	88.9	0.0	0.0	0.696	3.98	0.18
THF	46.1	65.3	19.5	0.010	2.88	88.8	0.0	0.0	0.696	3.98	0.37
CH_2Cl_2	46.2	65.4	19.8	0.010	2.85	88.8	0.0	0.0	0.696	3.98	0.38
H_2O	47.3	65.8	21.3	0.009	2.64	88.8	0.0	0.0	0.698	3.98	0.47
2^{Mes}			**S_1**								
C_6H_{12}	46.9	71.1	15.5	0.022	2.88						
C_6H_6	47.0	71.2	15.9	0.022	2.86						
THF	48.6	72.2	19.1	0.021	2.59						
CH_2Cl_2	47.3	71.3	19.4	0.019	2.57						
H_2O	63.9	46.1	22.1	0.009	2.63						
3^{Me,Me}			**S_1**					**S_2**			
C_6H_{12}	86.2	1.4	45.0	0.000	3.17	71.8	29.6	1.9	0.021	3.82	0.60
C_6H_6	86.7	1.6	45.6	0.000	3.06	71.8	26.8	2.1	0.022	3.82	0.69
THF	84.1	4.2	48.6	0.000	1.76	85.3	2.8	4.5	0.040	3.85	1.26
CH_2Cl_2	84.9	3.9	48.9	0.000	1.68	85.4	2.7	4.6	0.040	3.85	1.31
H_2O	82.7	6.5	49.9	0.000	1.11	86.3	2.9	5.0	0.043	3.85	1.51
3^{Me,Mes}			**S_1**					**S_2**			
C_6H_{12}	70.1	7.7	40.8	0.000	3.09	70.1	7.7	11.4	0.030	3.64	0.52
C_6H_6	70.7	7.9	41.4	0.000	3.00	70.7	7.9	11.3	0.028	3.62	0.57
THF	73.8	7.7	45.9	0.000	1.87	73.8	7.7	15.4	0.019	3.20	0.84
CH_2Cl_2	74.2	7.9	46.3	0.000	1.80	74.2	7.9	15.7	0.019	3.16	0.87
H_2O	77.3	9.5	48.1	0.000	1.27	77.3	9.5	17.5	0.016	2.92	0.98
4^{Me,Mes}			**S_1**					**S_2**			
C_6H_{12}	82.6	23.5	40.8	0.000	3.13	82.6	23.5	11.5	0.014	3.60	0.44
C_6H_6	83.1	23.8	41.5	0.000	3.03	83.1	23.8	12.7	0.018	3.62	0.53
THF	86.0	23.8	46.1	0.000	1.91	86.0	23.8	15.6	0.010	3.16	0.78
CH_2Cl_2	86.1	23.6	46.5	0.000	1.83	86.1	23.6	15.9	0.010	3.13	0.80
H_2O	86.4	23.3	48.3	0.000	1.30	86.4	23.3	17.4	0.008	2.88	0.91

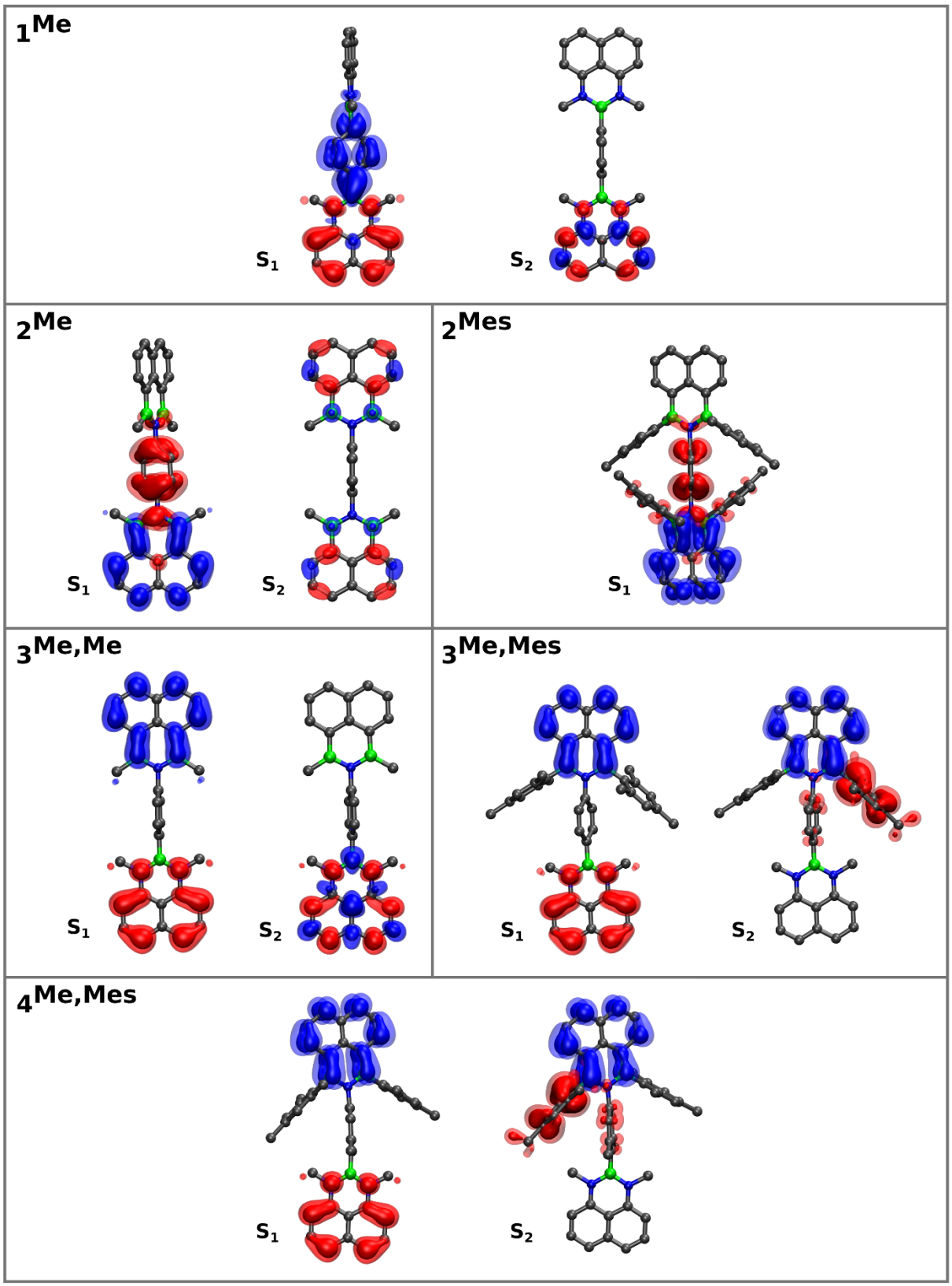

Figure S87: Unrelaxed difference densities for the singlet excited states (S_n) for emission at the relaxed ΔSCF/UKS/PCM excited state geometry calculated at the TDA-OT-LRC-ωPBEh/def2-TZVPP/SS-PCM[CH_2Cl_2] level of theory. Red represents the hole- and blue the electron density. All plots employ 0.997 [opaque] and 0.999 [translucent] as isovalues.

7.9. Results: redox potentials

In Table S15 both the first and second reduction and oxidation potentials are compiled for all compounds at the B3LYP-D4 and ωB97X-D3/ma-def2-QZVPP/SMD[THF]//r^2-SCAN-3c/SMD[THF] levels of theory. The FcH/FcH$^+$ redox couple serves as the reference. Figures S70–S75 display the orbital plots for the highest (singly) occupied (H[S]OMO) and lowest unoccupied molecular orbitals (LUMO) of the neutral, cationic, anionic species at the ωB97X-D3/ma-def2-QZVPP/SMD[THF]//r^2-SCAN-3c/SMD[THF] level of theory.

For the relevant first oxidation (**1**^{Me}, **3**^{Me,Me}, **3**^{Me,Mes}, and **4**^{Me,Mes}) and reduction (**2**^{Me}, **2**^{Mes}, **3**^{Me,Me}, **3**^{Me,Mes}, and **4**^{Me,Mes}) potentials, the results deviate only slightly (< 0.3 V) between B3LYP-D4 and ωB97X-D3. Notably, deviations are generally larger for the reduction, where ωB97X-D3 predicts more negative potentials than B3LYP-D4, which is in agreement with the experimental measurements. Moreover, ωB97X-D3 predicts a close second reduction of **2**^{Mes} only 0.13 V above the first (B3LYP-D4 is 0.74 V higher), which fits well to the two barely resolved experimental CV peaks (approx. –2.33 V). Hence, ωB97X-D3 appears to be more reliable for redox properties of the present systems. This is also expected for the range-separated hybrid density functional ωB97X-D3 compared to the global hybrid B3LYP-D4, owing to a more efficient reduction of self-interaction error prevalent in the one-electron oxidation or reduction processes. Generally, the observed errors w.r.t. the experimental measurements are in most cases substantially below 0.3 V (mean absolute error (MAE) 0.13 V), which is within expected limits, especially, considering the limitations of the implicit solvation model SMD for charged species.[S37,S40,S63–S65]

Table S15: First and second adiabatic reduction and oxidation potentials calculated at the DFT/ma-def2-QZVPP/SMD(THF)//r^{2}SCAN-3c/SMD(THF) level of theory, together with the available experimental data from Table 1. The FcH/FcH$^+$ redox couple is used as the reference for both theory and experiment.

Redox. Pot.		$E_{1.ox}$/V	$E_{2.ox}$/V	$E_{1.red}$/V	$E_{2.red}$/V
1^{Me}	B3LYP-D4	0.37	1.18	–3.63	–4.24
	ωB97X-D3	0.37	2.00	–4.22	–4.57
	Exp.	0.08	–	–	–
2^{Me}	B3LYP-D4	1.37	2.62	–2.40	–3.07
	ωB97X-D3	1.37	3.77	–2.69	–3.93
	Exp.	–	–	–2.52	–
2^{Mes}	B3LYP-D4	1.22	1.93	–2.28	–3.02
	ωB97X-D3	1.53	2.89	–2.55	–2.68
	Exp.	–	–	–2.21 and –2.43	
3^{Me,Me}	B3LYP-D4	0.30	1.80	–2.33	–3.45
	ωB97X-D3	0.30	1.87	–2.60	–3.76
	Exp.	0.39	–	–2.55	–
3^{Me,Mes}	B3LYP-D4	0.29	1.79	–2.23	–2.94
	ωB97X-D3	0.28	1.88	–2.49	–3.25
	Exp.	0.33	–	–2.47	–
4^{Me,Mes}	B3LYP-D4	0.28	1.84	–2.25	–3.40
	ωB97X-D3	0.26	1.95	–2.50	–3.71
	Exp.	0.32	–	–2.40	–

Where available, the HOMO of the neutral species is situated on the (or both) dan-units, which confirms that the first oxidation occurs on the formal neutral analog of the phenalenyl anion. Similarly, the LUMO of the resulting cationic species localizes to the dan-unit. For the BNB-homodyads **2**^{Me} and **2**^{Mes}, oxidation

is notably disfavored and occurs on either the electron-poor BNB-phenalenyl (**2**^{Me}) or the combined mesityl groups and the 1,4-phenylene bridge. This also agrees well with predicted LE and CT excitations of both compounds (see above).

Regarding the first reduction, the LUMO of the neutral species corresponds, in some cases, to a dissociated free electron solution and provides no useful information (marked with *, e.g., **1**^{Me}). This is a known issue due to the ill-defined nature of the LUMO in the self-consistent-field optimization of the orbital coefficients and arises if diffuse basis functions are available, as is presently the case.[S66] A more reliable indicator is the H(S)OMO of the anionic species, which is generally located on the dbn-subunits. Only in the case of the electron-rich **1**^{Me} lacking a dbn-subunit does the reduction occur on the phenyl bridge, which aligns well with its electron-accepting role in the dan-to-Ph-CT state (see above).

Moving to the second reduction of the BNB-homodyads **2**^{Me} and **2**^{Mes}, the LUMO of the anionic species is now located on the second (unreduced) dbn-subunit. A reason for the preferential second reduction of **2**^{Mes} cannot be discerned in the MO plots.

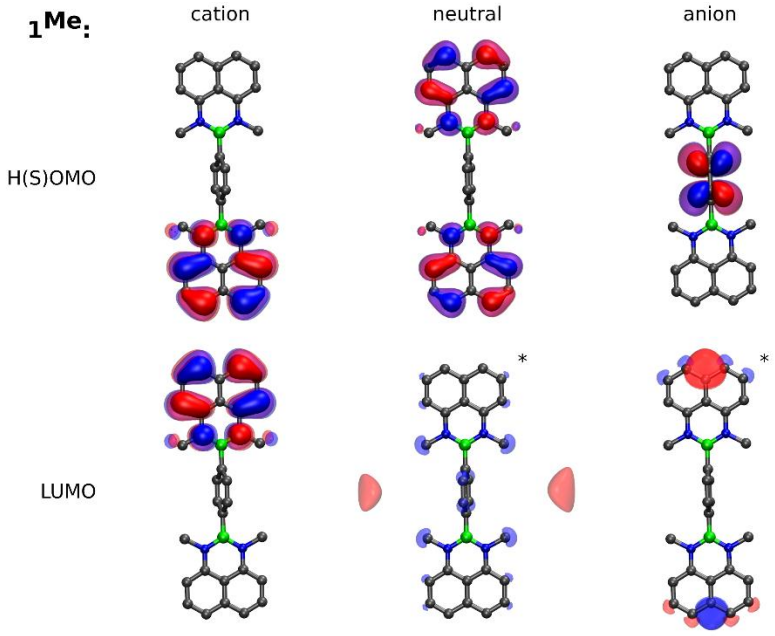

Figure S88: Highest (singly) occupied [H(S)OMO, top] and lowest unoccupied molecular orbital [LUMO] of the neutral, cationic, and anionic compound **1**^{Me} at the ωB97X-D3/ma-def2-QZVPP/SMD[THF]//r^2-SCAN-3c/SMD[THF] level of theory. The LUMO of the neutral and anionic species (marked by *) represent an artificial free electron solution, which arise due to the ill-defined nature of the unoccupied orbitals, if diffuse basis functions are available.[S66] All plots employ 0.96 [opaque] and 0.98 [translucent] as isovalues.

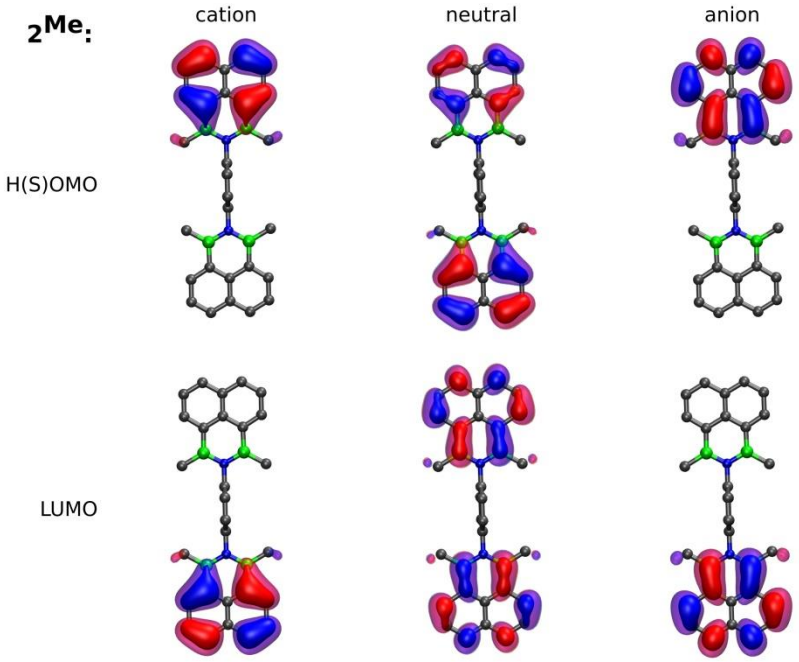

Figure S89: Highest (singly) occupied [H(S)OMO, top] and lowest unoccupied molecular orbital [LUMO] of the neutral, cationic, and anionic compound $\mathbf{2}^{\mathbf{Me}}$ at the ωB97X-D3/ma-def2-QZVPP/SMD[THF]//r^2-SCAN-3c/SMD[THF] level of theory. All plots employ 0.96 [opaque] and 0.98 [translucent] as isovalues.

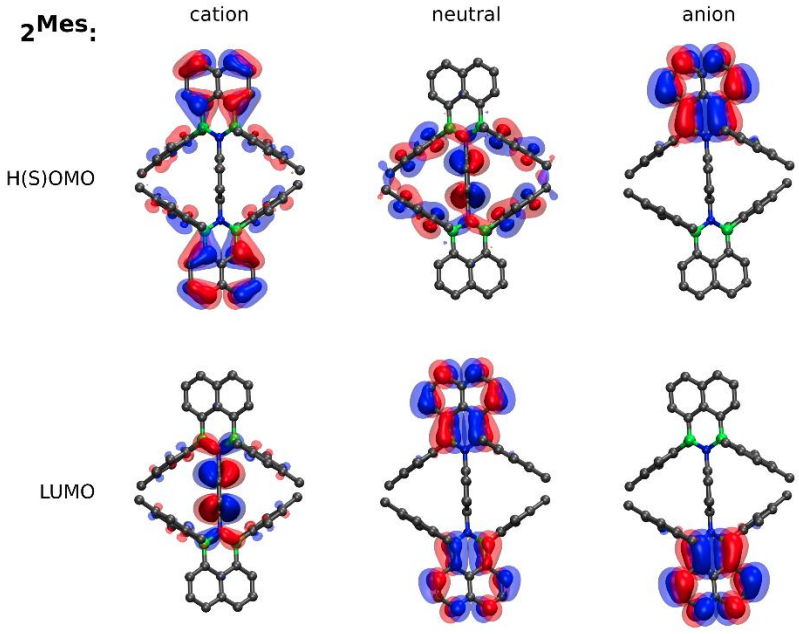

Figure S90: Highest (singly) occupied [H(S)OMO, top] and lowest unoccupied molecular orbital [LUMO] of the neutral, cationic, and anionic compound $\mathbf{2}^{\mathbf{Mes}}$ at the ωB97X-D3/ma-def2-QZVPP/SMD[THF]//r^2-SCAN-3c/SMD[THF] level of theory. All plots employ 0.96 [opaque] and 0.98 [translucent] as isovalues.

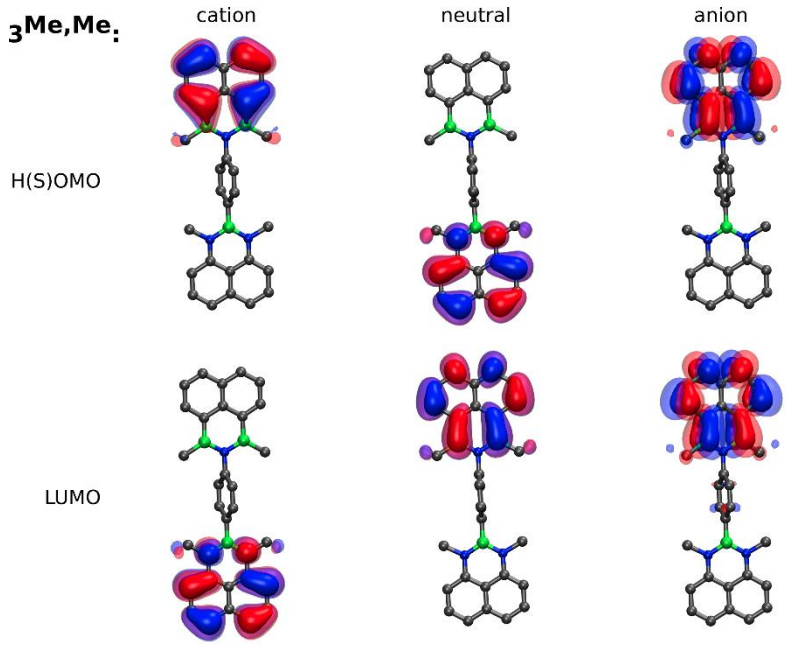

Figure S91: Highest (singly) occupied [H(S)OMO, top] and lowest unoccupied molecular orbital [LUMO] of the neutral, cationic, and anionic compound **3**^{Me,Me} at the ωB97X-D3/ma-def2-QZVPP/SMD[THF]//r^2-SCAN-3c/SMD[THF] level of theory. All plots employ 0.96 [opaque] and 0.98 [translucent] as isovalues.

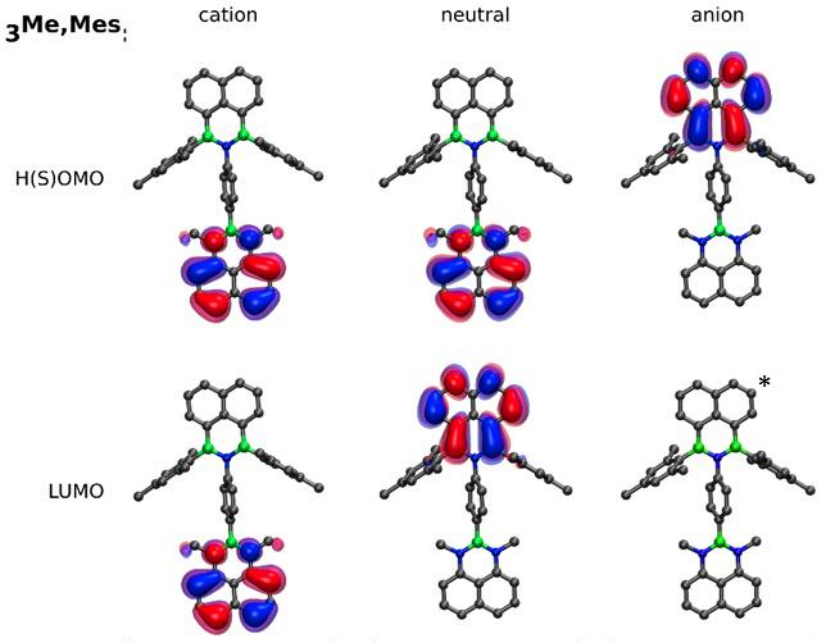

Figure S92: Highest (singly) occupied [H(S)OMO, top] and lowest unoccupied molecular orbital [LUMO] of the neutral, cationic, and anionic compound **3**^{Me,Mes} at the ωB97X-D3/ma-def2-QZVPP/SMD[THF]//r^2-SCAN-3c/SMD[THF] level of theory. The LUMO of the anionic species (marked by *) represents an artificial free electron solution, which arises due to the ill-defined nature of the unoccupied orbitals, if diffuse basis functions are available.[S66] All plots employ 0.96 [opaque] and 0.98 [translucent] as isovalues.

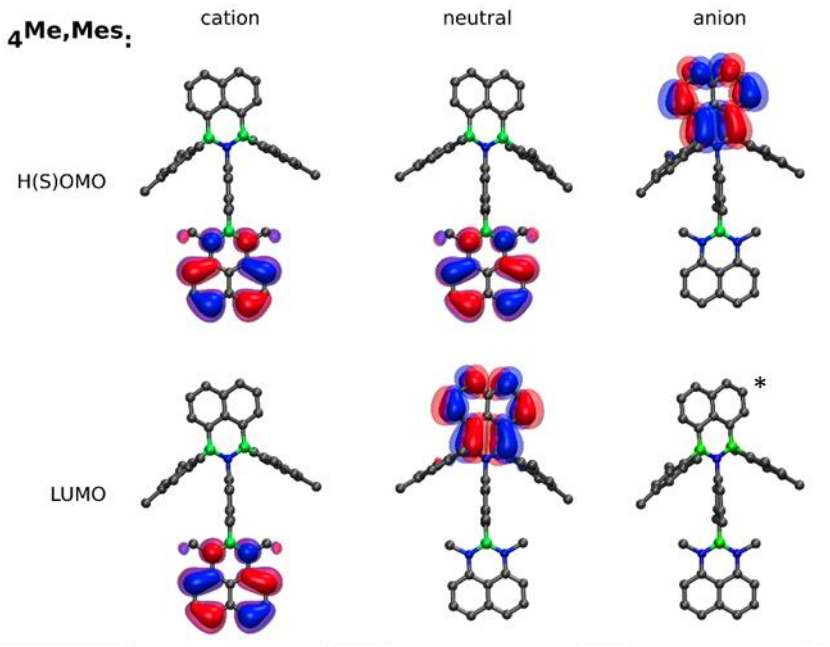

Figure S93: Highest (singly) occupied [H(S)OMO, top] and lowest unoccupied molecular orbital [LUMO] of the neutral, cationic, and anionic compound **4**^{Me,Mes} at the ωB97X-D3/ma-def2-QZVPP/SMD[THF]//r^2-SCAN-3c/SMD[THF] level of theory. The LUMO of the anionic species (marked by *) represents an artificial free electron solution, which arises due to the ill-defined nature of the unoccupied orbitals, if diffuse basis functions are available.[S66] All plots employ 0.96 [opaque] and 0.98 [translucent] as isovalues.

8. References

S1 A. S. Scholz, J. G. Massoth, M. Bursch, J.-M. Mewes, T. Hetzke, B. Wolf, M. Bolte, H.-W. Lerner, S. Grimme and M. Wagner, BNB-Doped Phenalenyls: Modular Synthesis, Optoelectronic Properties, and One-Electron Reduction, *J. Am. Chem. Soc.*, 2020, **142**, 11072–11083.

S2 A. S. Scholz, J. G. Massoth, L. Stoess, M. Bolte, M. Braun, H.-W. Lerner, J.-M. Mewes, M. Wagner and T. Froitzheim, NBN- and BNB-Phenalenyls: the Yin and Yang of Heteroatom-doped π Systems, *Chem. Eur. J.*, 2024, e202400320.

S3 C. Li, S. K. Mellerup, X. Wang and S. Wang, Accessing Two-Stage Regioselective Photoisomerization in Unsymmetrical N,C-Chelate Organoboron Compounds: Reactivity of B(ppz)(Mes)Ar, *Organometallics*, 2018, **37**, 3360–3367.

S4 P. Sudhakar, S. Mukherjee and P. Thilagar, Revisiting Borylanilines: Unique Solid-State Structures and Insight into Photophysical Properties, *Organometallics*, 2013, **32**, 3129–3133.

S5 R. W. Alder, N. P. Hyland, J. C. Jeffery, T. Riis-Johannessen and D. J. Riley, Poly(1,1-bis(dialkylamino)propan-1,3-diyl)s; conformationally-controlled oligomers bearing electroactive groups, *Org. Biomol. Chem.*, 2009, **7**, 2704–2715.

S6 G. R. Fulmer, A. J. M. Miller, N. H. Sherden, H. E. Gottlieb, A. Nudelman, B. M. Stoltz, J. E. Bercaw and K. I. Goldberg, NMR Chemical Shifts of Trace Impurities: Common Laboratory Solvents, Organics, and Gases in Deuterated Solvents Relevant to the Organometallic Chemist, *Organometallics*, 2010, **29**, 2176–2179.

S7 K. Suzuki, A. Kobayashi, S. Kaneko, K. Takehira, T. Yoshihara, H. Ishida, Y. Shiina, S. Oishi and S. Tobita, Reevaluation of absolute luminescence quantum yields of standard solutions using a spectrometer with an integrating sphere and a back-thinned CCD detector, *Phys. Chem. Chem. Phys.*, 2009, **11**, 9850–9860.

S8 A. M. Brouwer, Standards for photoluminescence quantum yield measurements in solution (IUPAC Technical Report), *Pure Appl. Chem.*, 2011, **83**, 2213–2228.

S9 F. Barrière and W. E. Geiger, Use of Weakly Coordinating Anions to Develop an Integrated Approach to the Tuning of $\Delta E_{1/2}$ Values by Medium Effects, *J. Am. Chem. Soc.*, 2006, **128**, 3980–3989.

S10 D. R. Nielsen and W. E. McEwen, Benzenediboronic Acids, *J. Am. Chem. Soc.*, 1957, **79**, 3081–3084.

S11 *Stoe & Cie.*, *X-AREA. Diffractometer control program system*, Stoe & Cie, Darmstadt, Germany, 2002.

S12 G. M. Sheldrick, A short history of *SHELX*, *Acta Crystallogr. A*, 2008, **64**, 112–122.

S13 E. Epifanovsky, A. T. B. Gilbert, X. Feng, J. Lee, Y. Mao, N. Mardirossian, P. Pokhilko, A. F. White, M. P. Coons, A. L. Dempwolff, Z. Gan, D. Hait, P. R. Horn, L. D. Jacobson, I. Kaliman, J. Kussmann, A. W. Lange, K. U. Lao, D. S. Levine, J. Liu, S. C. McKenzie, A. F. Morrison, K. D. Nanda, F. Plasser, D. R. Rehn, M. L. Vidal, Z.-Q. You, Y. Zhu, B. Alam, B. J. Albrecht, A. Aldossary, E. Alguire, J. H. Andersen, V. Athavale, D. Barton, K. Begam, A. Behn, N. Bellonzi, Y. A. Bernard, E. J. Berquist, H. G. A. Burton, A. Carreras, K. Carter-Fenk, R. Chakraborty, A. D. Chien, K. D. Closser, V. Cofer-Shabica, S. Dasgupta, M. de Wergifosse, J. Deng, M. Diedenhofen, H. Do, S. Ehlert, P.-T. Fang, S. Fatehi, Q. Feng, T. Friedhoff, J. Gayvert, Q. Ge, G. Gidofalvi, M. Goldey, J. Gomes, C. E. González-Espinoza, S. Gulania, A. O. Gunina, M. W. D. Hanson-Heine, P. H. P. Harbach, A. Hauser, M. F. Herbst, M. Hernández Vera, M. Hodecker, Z. C. Holden, S. Houck, X. Huang, K. Hui, B. C. Huynh, M. Ivanov, Á. Jász, H. Ji, H. Jiang, B. Kaduk, S. Kähler, K. Khistyaev, J. Kim, G. Kis, P. Klunzinger, Z. Koczor-Benda, J. H. Koh, D. Kosenkov, L. Koulias, T. Kowalczyk, C. M. Krauter, K. Kue, A. Kunitsa, T. Kus, I. Ladjánszki, A. Landau, K. V. Lawler, D. Lefrancois, S. Lehtola, R. R. Li, Y.-P. Li, J. Liang, M. Liebenthal, H.-H. Lin, Y.-S. Lin, F. Liu, K.-Y. Liu, M. Loipersberger, A. Luenser, A. Manjanath, P. Manohar, E. Mansoor, S. F. Manzer, S.-P. Mao, A. V. Marenich, T. Markovich, S. Mason, S. A. Maurer, P. F. McLaughlin, M. F. S. J. Menger, J.-M. Mewes, S. A. Mewes, P. Morgante, J. W. Mullinax, K. J. Oosterbaan, G. Paran, A. C.

Paul, S. K. Paul, F. Pavošević, Z. Pei, S. Prager, E. I. Proynov, Á. Rák, E. Ramos-Cordoba, B. Rana, A. E. Rask, A. Rettig, R. M. Richard, F. Rob, E. Rossomme, T. Scheele, M. Scheurer, M. Schneider, N. Sergueev, S. M. Sharada, W. Skomorowski, D. W. Small, C. J. Stein, Y.-C. Su, E. J. Sundstrom, Z. Tao, J. Thirman, G. J. Tornai, T. Tsuchimochi, N. M. Tubman, S. P. Veccham, O. Vydrov, J. Wenzel, J. Witte, A. Yamada, K. Yao, S. Yeganeh, S. R. Yost, A. Zech, I. Y. Zhang, X. Zhang, Y. Zhang, D. Zuev, A. Aspuru-Guzik, A. T. Bell, N. A. Besley, K. B. Bravaya, B. R. Brooks, D. Casanova, J.-D. Chai, S. Coriani, C. J. Cramer, G. Cserey, A. E. DePrince, III, R. A. DiStasio, Jr., A. Dreuw, B. D. Dunietz, T. R. Furlani, W. A. Goddard, III, S. Hammes-Schiffer, T. Head-Gordon, W. J. Hehre, C.-P. Hsu, T.-C. Jagau, Y. Jung, A. Klamt, J. Kong, D. S. Lambrecht, W. Liang, N. J. Mayhall, C. W. McCurdy, J. B. Neaton, C. Ochsenfeld, J. A. Parkhill, R. Peverati, V. A. Rassolov, Y. Shao, L. V. Slipchenko, T. Stauch, R. P. Steele, J. E. Subotnik, A. J. W. Thom, A. Tkatchenko, D. G. Truhlar, T. Van Voorhis, T. A. Wesolowski, K. B. Whaley, H. L. Woodcock, III, P. M. Zimmerman, S. Faraji, P. M. W. Gill, M. Head-Gordon, J. M. Herbert and A. I. Krylov, Software for the frontiers of quantum chemistry: An overview of developments in the Q-Chem 5 package, *J. Chem. Phys.*, 2021, **155**, 084801.

S14 E. Runge and E. K. U. Gross, Density-Functional Theory for Time-Dependent Systems, *Phys. Rev. Lett.*, 1984, **52**, 997–1000.

S15 M. Petersilka, U. J. Gossmann and E. K. U. Gross, Excitation Energies from Time-Dependent Density-Functional Theory, *Phys. Rev. Lett.*, 1996, **76**, 1212–1215.

S16 S. Hirata and M. Head-Gordon, Time-dependent density functional theory within the Tamm–Dancoff approximation, *Chem. Phys. Lett.*, 1999, **314**, 291–299.

S17 T. Stein, L. Kronik and R. Baer, Prediction of charge-transfer excitations in coumarin-based dyes using a range-separated functional tuned from first principles, *J. Chem. Phys.*, 2009, **131**, 244119.

S18 R. Baer, E. Livshits and U. Salzner, Tuned Range-Separated Hybrids in Density Functional Theory, *Annu. Rev. Phys. Chem.*, 2010, **61**, 85–109.

S19 A. T. B. Gilbert, N. A. Besley and P. M. W. Gill, Self-Consistent Field Calculations of Excited States Using the Maximum Overlap Method (MOM), *J. Phys. Chem. A*, 2008, **112**, 13164–13171.

S20 S. G. Balasubramani, G. P. Chen, S. Coriani, M. Diedenhofen, M. S. Frank, Y. J. Franzke, F. Furche, R. Grotjahn, M. E. Harding, C. Hättig, A. Hellweg, B. Helmich-Paris, C. Holzer, U. Huniar, M. Kaupp, A. Marefat Khah, S. Karbalaei Khani, T. Müller, F. Mack, B. D. Nguyen, S. M. Parker, E. Perlt, D. Rappoport, K. Reiter, S. Roy, M. Rückert, G. Schmitz, M. Sierka, E. Tapavicza, D. P. Tew, C. van Wüllen, V. K. Voora, F. Weigend, A. Wodyński and J. M. Yu, TURBOMOLE: Modular program suite for *ab initio* quantum-chemical and condensed-matter simulations, *J. Chem. Phys.*, 2020, **152**, 184107.

S21 Y. J. Franzke, C. Holzer, J. H. Andersen, T. Begušić, F. Bruder, S. Coriani, F. Della Sala, E. Fabiano, D. A. Fedotov, S. Fürst, S. Gillhuber, R. Grotjahn, M. Kaupp, M. Kehry, M. Krstić, F. Mack, S. Majumdar, B. D. Nguyen, S. M. Parker, F. Pauly, A. Pausch, E. Perlt, G. S. Phun, A. Rajabi, D. Rappoport, B. Samal, T. Schrader, M. Sharma, E. Tapavicza, R. S. Treß, V. Voora, A. Wodyński, J. M. Yu, B. Zerulla, F. Furche, C. Hättig, M. Sierka, D. P. Tew and F. Weigend, TURBOMOLE: Today and Tomorrow, *J. Chem. Theory Comput.*, 2023, **19**, 6859–6890.

S22 F. Eckert and A. Klamt, *COSMOtherm, Version C30-1601 (revision 2299), release 16.01*, COSMOlogic GmbH & Co. KG, Leverkusen (Germany), 2016.

S23 A. Klamt and G. Schüürmann, COSMO: a new approach to dielectric screening in solvents with explicit expressions for the screening energy and its gradient, *J. Chem. Soc., Perkin Trans. 2*, 1993, 799–805.

S24 A. Klamt, Conductor-like Screening Model for Real Solvents: A New Approach to the Quantitative Calculation of Solvation Phenomena, *J. Phys. Chem.*, 1995, **99**, 2224–2235.

S25 F. Neese, The ORCA program system, *Wiley Interdiscip. Rev.: Comput. Mol. Sci.*, 2012, **2**, 73–78.

S26 P. Pracht, F. Bohle and S. Grimme, Automated exploration of the low-energy chemical space with fast quantum chemical methods, *Phys. Chem. Chem. Phys.*, 2020, **22**, 7169–7192.

S27 S. Grimme, F. Bohle, A. Hansen, P. Pracht, S. Spicher and M. Stahn, Efficient Quantum Chemical Calculation of Structure Ensembles and Free Energies for Nonrigid Molecules, *J. Phys. Chem. A*, 2021, **125**, 4039–4054.

S28 C. Bannwarth, S. Ehlert and S. Grimme, GFN2-xTB – An Accurate and Broadly Parametrized Self-Consistent Tight-Binding Quantum Chemical Method with Multipole Electrostatics and Density-Dependent Dispersion Contributions, *J. Chem. Theory Comput.*, 2019, **15**, 1652–1671.

S29 C. Bannwarth, E. Caldeweyher, S. Ehlert, A. Hansen, P. Pracht, J. Seibert, S. Spicher and S. Grimme, Extended tight-binding quantum chemistry methods, *Wiley Interdiscip. Rev.: Comput. Mol. Sci.*, 2021, **11**, e1493.

S30 M. D. Hanwell, D. E. Curtis, D. C. Lonie, T. Vandermeersch, E. Zurek and G. R. Hutchison, Avogadro: an advanced semantic chemical editor, visualization, and analysis platform, *J. Cheminform.*, 2012, **4**, 17.

S31 W. Humphrey, A. Dalke and K. Schulten, VMD: Visual molecular dynamics, *J. Mol. Graph.*, 1996, **14**, 33–38.

S32 S. Ehlert, M. Stahn, S. Spicher and S. Grimme, Robust and Efficient Implicit Solvation Model for Fast Semiempirical Methods, *J. Chem. Theory Comput.*, 2021, **17**, 4250–4261.

S33 S. Grimme, A. Hansen, S. Ehlert and J.-M. Mewes, r^2SCAN-3c: A "Swiss army knife" composite electronic-structure method, *J. Chem. Phys.*, 2021, **154**, 064103.

S34 A. Klamt, The COSMO and COSMO-RS solvation models, *Wiley Interdiscip. Rev.: Comput. Mol. Sci.*, 2018, **8**, e1338.

S35 S. Grimme, Supramolecular Binding Thermodynamics by Dispersion-Corrected Density Functional Theory, *Chem. Eur. J.*, 2012, **18**, 9955–9964.

S36 S. Spicher and S. Grimme, Single-Point Hessian Calculations for Improved Vibrational Frequencies and Rigid-Rotor-Harmonic-Oscillator Thermodynamics, *J. Chem. Theory Comput.*, 2021, **17**, 1701–1714.

S37 A. V. Marenich, C. J. Cramer and D. G. Truhlar, Universal Solvation Model Based on Solute Electron Density and on a Continuum Model of the Solvent Defined by the Bulk Dielectric Constant and Atomic Surface Tensions, *J. Phys. Chem. B*, 2009, **113**, 6378–6396.

S38 S. Miertuš, E. Scrocco and J. Tomasi, Electrostatic interaction of a solute with a continuum. A direct utilizaion of AB initio molecular potentials for the prevision of solvent effects, *Chem. Phys.*, 1981, **55**, 117–129.

S39 J. Tomasi, B. Mennucci and E. Cancès, The IEF version of the PCM solvation method: an overview of a new method addressed to study molecular solutes at the QM ab initio level, *J. Mol. Struc.: THEOCHEM*, 1999, **464**, 211–226.

S40 J. M. Herbert, Dielectric continuum methods for quantum chemistry, *Wiley Interdiscip. Rev.: Comput. Mol. Sci.*, 2021, **11**, e1519.

S41 A. Dreuw and M. Head-Gordon, Single-Reference ab Initio Methods for the Calculation of Excited States of Large Molecules, *Chem. Rev.*, 2005, **105**, 4009–4037.

S42 L. Kunze, A. Hansen, S. Grimme and J.-M. Mewes, PCM-ROKS for the Description of Charge-Transfer States in Solution: Singlet–Triplet Gaps with Chemical Accuracy from Open-Shell Kohn–Sham Reaction-Field Calculations, *J. Phys. Chem. Lett.*, 2021, **12**, 8470–8480.

S43 T. Froitzheim, S. Grimme and J.-M. Mewes, Either Accurate Singlet–Triplet Gaps or Excited-State Structures: Testing and Understanding the Performance of TD-DFT for TADF Emitters, *J. Chem. Theory Comput.*, 2022, **18**, 7702–7713.

S44 M. A. Rohrdanz, K. M. Martins and J. M. Herbert, A long-range-corrected density functional that performs well for both ground-state properties and time-dependent density functional theory excitation energies, including charge-transfer excited states, *J. Chem. Phys.*, 2009, **130**, 054112.

S45 F. Weigend and R. Ahlrichs, Balanced basis sets of split valence, triple zeta valence and quadruple zeta valence quality for H to Rn: Design and assessment of accuracy, *Phys. Chem. Chem. Phys.*, 2005, **7**, 3297–3305.
S46 F. Weigend, Accurate Coulomb-fitting basis sets for H to Rn, *Phys. Chem. Chem. Phys.*, 2006, **8**, 1057–1065.
S47 E. Caldeweyher, C. Bannwarth and S. Grimme, Extension of the D3 dispersion coefficient model, *J. Chem. Phys.*, 2017, **147**, 034112.
S48 E. Caldeweyher, S. Ehlert, A. Hansen, H. Neugebauer, S. Spicher, C. Bannwarth and S. Grimme, A generally applicable atomic-charge dependent London dispersion correction, *J. Chem. Phys.*, 2019, **150**, 154122.
S49 M. Friede, S. Ehlert, S. Grimme and J.-M. Mewes, Do Optimally Tuned Range-Separated Hybrid Functionals Require a Reparametrization of the Dispersion Correction? It Depends, *J. Chem. Theory Comput.*, 2023, **19**, 8097–8107.
S50 R. Improta, V. Barone, G. Scalmani and M. J. Frisch, A state-specific polarizable continuum model time dependent density functional theory method for excited state calculations in solution, *J. Chem. Phys.*, 2006, **125**, 054103.
S51 J.-M. Mewes, J. M. Herbert and A. Dreuw, On the accuracy of the general, state-specific polarizable-continuum model for the description of correlated ground- and excited states in solution, *Phys. Chem. Chem. Phys.*, 2017, **19**, 1644–1654.
S52 J. Shee and M. Head-Gordon, Predicting Excitation Energies of Twisted Intramolecular Charge-Transfer States with the Time-Dependent Density Functional Theory: Comparison with Experimental Measurements in the Gas Phase and Solvents Ranging from Hexanes to Acetonitrile, *J. Chem. Theory Comput.*, 2020, **16**, 6244–6255.
S53 J.-M. Mewes, Z.-Q. You, M. Wormit, T. Kriesche, J. M. Herbert and A. Dreuw, Experimental Benchmark Data and Systematic Evaluation of Two *a Posteriori*, Polarizable-Continuum Corrections for Vertical Excitation Energies in Solution, *J. Phys. Chem. A*, 2015, **119**, 5446–5464.
S54 S. Chibani, Š. Budzák, M. Medved', B. Mennucci and D. Jacquemin, Full cLR-PCM calculations of the solvatochromic effects on emission energies, *Phys. Chem. Chem. Phys.*, 2014, **16**, 26024–26029.
S55 P. Winget, D. Dolney, D. Giesen, C. Cramer and D. Truhlar, *Minnesota solvent descriptor database*, 1999.
S56 M. Kasha, Characterization of electronic transitions in complex molecules, *Discuss. Faraday Soc.*, 1950, **9**, 14–19.
S57 A. D. Becke, Density-functional thermochemistry. III. The role of exact exchange, *J. Chem. Phys.*, 1993, **98**, 5648–5652.
S58 P. J. Stephens, F. J. Devlin, C. F. Chabalowski and M. J. Frisch, *Ab Initio* Calculation of Vibrational Absorption and Circular Dichroism Spectra Using Density Functional Force Fields, *J. Phys. Chem.*, 1994, **98**, 11623–11627.
S59 Y.-S. Lin, G.-D. Li, S.-P. Mao and J.-D. Chai, Long-Range Corrected Hybrid Density Functionals with Improved Dispersion Corrections, *J. Chem. Theory Comput.*, 2013, **9**, 263–272.
S60 S. Grimme, J. Antony, S. Ehrlich and H. Krieg, A consistent and accurate *ab initio* parametrization of density functional dispersion correction (DFT-D) for the 94 elements H-Pu, *J. Chem. Phys.*, 2010, **132**, 154104.
S61 S. Grimme, A. Hansen, J. G. Brandenburg and C. Bannwarth, Dispersion-Corrected Mean-Field Electronic Structure Methods, *Chem. Rev.*, 2016, **116**, 5105–5154.
S62 J. Zheng, X. Xu and D. G. Truhlar, Minimally augmented Karlsruhe basis sets, *Theor. Chem. Acc.*, 2011, **128**, 295–305.
S63 A. V Marenich, C. P. Kelly, J. D. Thompson, G. D. Hawkins, C. C. Chambers, D. J. Giesen, P. Winget, C. J. Cramer and D. G. Truhlar, Minnesota Solvation Database (MNSOL) version 2012, https://doi.org/10.13020/3eks-j059, (accessed 5 March 2024).

S64 D. L. Mobley and J. P. Guthrie, FreeSolv: a database of experimental and calculated hydration free energies, with input files, *J. Comput.-Aided Mol. Des.*, 2014, **28**, 711–720.
S65 C. Plett, M. Stahn, M. Bursch, J.-M. Mewes and S. Grimme, Improving Quantum Chemical Solvation Models by Dynamic Radii Adjustment for Continuum Solvation (DRACO), *J. Phys. Chem. Lett.*, 2024, **15**, 2462–2469.
S66 F. Jensen, *Introduction to Computational Chemistry*, 3rd ed., Wiley & Sons Ltd, Chichester, 2017.